Label Free Methods for the Quantification of Molecular Interaction with Membrane Protein on Cell Surface

by

Fenni Zhang

A Dissertation Presented in Partial Fulfillment
of the Requirements for the Degree
Doctor of Philosophy

Approved July 2018 by the
Graduate Supervisory Committee:

Nongjian Tao, Chair
Junseok Chae
Chad Borges
Tianwei Jing
Shaopeng Wang

ARIZONA STATE UNIVERSITY

December 2018

ABSTRACT

Measuring molecular interaction with membrane proteins is critical for understanding cellular functions, validating biomarkers and screening drugs. Despite the importance, developing such a capability has been a difficult challenge, especially for small molecules binding to membrane proteins in their native cellular environment. The current mainstream practice is to isolate membrane proteins from the cell membranes, which is difficult and often lead to the loss of their native structures and functions. In this thesis, novel detection methods for *in situ* quantification of molecular interactions with membrane proteins are described.

First, a label-free surface plasmon resonance imaging (SPRi) platform is developed for the *in situ* detection of the molecular interactions between membrane protein drug target and its specific antibody drug molecule on cell surface. With this method, the binding kinetics of the drug-target interaction is quantified for drug evaluation and the receptor density on the cell surface is also determined.

Second, a label-free mechanically amplification detection method coupled with a microfluidic device is developed for the detection of both large and small molecules on single cells. Using this method, four major types of transmembrane proteins, including glycoproteins, ion channels, G-protein coupled receptors (GPCRs) and tyrosine kinase receptors on single whole cells are studied with their specific drug molecules. The basic principle of this method is established by developing a thermodynamic model to express the binding-induced nanometer-scale cellular deformation in terms of membrane protein density and cellular mechanical properties. Experiments are carried out to validate the model.

Last, by tracking the cell membrane edge deformation, molecular binding induced downstream event – granule exocytosis is measured with a dual-optical imaging system. Using this method, the single granule exocytosis events in single cells are monitored and the temporal-spatial distribution of the granule fusion-induced cell membrane deformation are mapped. Different patterns of granule release are resolved, including multiple release events occurring close in time and position. The label-free cell membrane deformation tracking method was validated with the simultaneous fluorescence recording. And the simultaneous cell membrane deformation detection and fluorescence recording allow the study of the propagation of the granule release-induced membrane deformation along cell surfaces.

DEDICATION

To my beloved family, my parents, my husband and my dear daughter for their endless love and selfless support.

ACKNOWLEDGMENTS

First of all, I would like to express my sincere gratitude to my advisor Dr. Nongjian Tao for his continued guidance, encouragement and support during my PhD study and research. His passion and immense knowledge in research inspired me to work on different projects, to solve difficult problems and to become an excellent researcher.

I would like to thank other committee members, Dr. Junseok Chae, Dr. Chad Borges, Dr. Tianwei Jing and Dr. Shaopeng Wang, for their help and advice.

My sincere thanks also goes to Dr. Erica Forzoni, Dr. Shaopeng Wang, Dr. Yunze Yang, Dr. Hui Yu and Dr. Yan Guan for their great help and discuss on my different projects. I learnt a lot about finding and solving problems from them.

It has been a valuable experience to work in Dr. Tao's group where I can learn from everyone in the group. I would like to explicitly thanks Drs Di Wang, Xiaonan Shan, Francis Tsow, Yixian Wang, Xianwei Liu, Linliang Yin, Wenwen Jing, Karan Syal, Di Zhao, Yueqi Li, Liming Xiang, Dangdang Shao, Yuting Yang, Xiaojun Xian, Yue Deng and Devon Bridgeman, as well as Mr. Yan Wang, Mr. Guangzhong Ma, Mr. Rafael Iriya, Ms. Manni Mo, Ms. Runli Liang, Ms. Ashley Hunt, Mr. Hao Zhu, and Ms. Chenwen Lin. I will always treasure the time working with you.

TABLE OF CONTENTS

Page

CHAPTER Page

CHAPTER Page

CHAPTER Page

LIST OF TABLES

LIST OF FIGURES

Figure Page

Figure Page

Figure Page

Figure Page

CHAPTER 1 INTRODUCTION AND BACKGROUND

1.1 Introduction

Molecular interaction plays an important role in many fundamental biological processes, such as cell growth and metabolism, immune system responses, and disease development and treatment [1, 2]. When the ligand molecule binds to its target receptor, a specific receptor-ligand complex will form and evoke a cascade of downstream responses for biological signaling. Besides, molecular interaction is critical for detecting disease biomarkers, and for drug screening to evaluate the drug potency and efficacy. Therefore, it is of great value to develop a quantitative platform for the measurement of the molecular interaction.

Membrane proteins are the most targeted receptors for molecular interaction, which is responsible for relaying signals between a cell and its external environment, moving ions and molecules across the membrane, and allows it to recognize other cells and attach to a surface, regulating almost all cellular functions [3-5]. Membrane proteins are also the most important drug targets, comprising more than 60% of the current therapeutic drug targets [6]. When small molecule drug or antibody drug bind to the membrane proteins, it normally initiates or inhibits the function of certain pathways for the disease treatment [7]. For both studying the cellular functions and discovering new drugs, it is necessary to measure the binding of membrane proteins with various ligands and drug candidate molecules, and quantify the binding kinetics in order to determine how strong and fast the binding is [5, 8] and evaluate drug potency and efficacy.[8-10]

Quantifying the binding affinity of a ligand molecule with its specific membrane protein provides valuable information for drug screening and optimization. The affinities of good drug candidates are often in the nM range, but weaker and stronger affinities are also observed [11, 12]. To screening the best drug for one targeted receptor, more binding constants need to be considered. Binding kinetics determine how fast a drug associates and dissociates with its receptor, providing excellent supplementary information for further drug potency evaluation [9, 13]. Thus, the detection of binding kinetics is also important in drug development, especially for small molecules, as more than 50% of the current drugs are small molecules.

1.2 Membrane Protein

Membrane proteins are the proteins that bound with the cell membrane, which constitutes one of the largest and most important classes of proteins, accounting for about 30% of a cell's typical proteins [14]. Some of them are bound only to the membrane surface, whereas others are transmembrane proteins and have domains on one or both sides. The extracellular domains of the proteins are generally involved in molecular recognition for cell – cell signaling and binding interactions, the transmembrane domain, particularly those that form channels or pores, can move different ions or molecules across the cell membrane for signaling transduction, while the intracellular domains often have a variety of functions, triggering different intracellular signaling pathways.

Membrane proteins are the starting point for a huge variety of cellular signal transduction pathways, ranging from the basic molecular recognition function to various physiological and pathological functions. Many diseases are caused by the mutations of

membrane proteins, for example the neurological diseases, depression and schizophrenia are resulting from the mutation of ion channels, while cystic fibrosis is due to the mutation of an ATP-binding cassette transporter (ABC transporter) protein [15-17]. Mutations that cause a certain membrane protein overexpressing and constant activation often lead to uncontrolled diseases. Therefore, quantification of membrane protein expression density in cell membrane is important for disease diagnosis. Furthermore, more than 60% of the current drugs bind to targeted membrane proteins for disease treatment (Figure 1.1). The binding interaction with membrane protein is proposed to be the key process in drug screening and optimization.

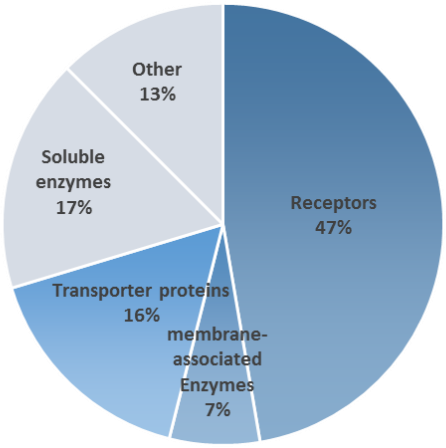

Figure 1.1 Drug classes of current drug therapies.[18] The transmembrane proteins are the most targeted membrane proteins in drug screening, which can be divided into three different groups according to their basic structure and function in ligand – protein interaction (Figure 1.2). The first group of these proteins are ligand - gated ion channels, which allow the influx and efflux of certain ions along the concentration gradient when activated. The second group of transmembrane proteins are membrane transporters, which

span the whole membrane and transport the specific bonded molecules across the membrane. The last group are called membrane receptors, which can be activated by the binding of specific ligands for cellular signal transduction.

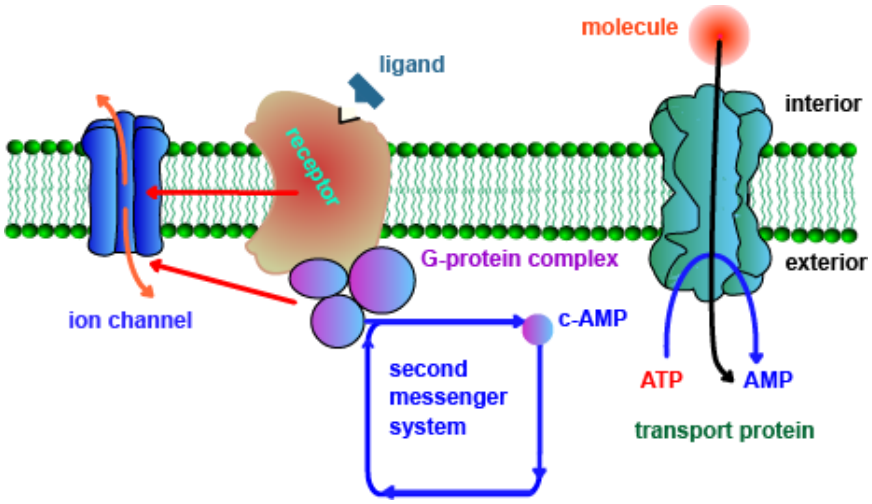

Figure 1.2 Three different types of transmembrane proteins. [From ChemgaPedia at http://www.chemgapedia.de/vsengine/en/index.html]

Membrane ion channels are transmembrane proteins that form a hydrophilic pore with multiple subunits to allow certain ion flux passing through, which play an important role in maintaining the electrostatic equilibrium and cell function. According to the gating methods, membrane ion channels can be divided as voltage – gated ion channels and ligand – gated ion channels. Voltage – gated ion channels open or close in response to the changes of membrane potential, playing a key role in electrical signal generation and transduction. However, no ligand binding process involved in these proteins. The ligand – gated ion channels are more related with the binding process and posing great significance in drug discovery and development. When the molecule binds as a ligand to the ion channel receptor, the gate will open to allow specific ions, such as Na^+ or Ca^{2+} to pass through. A

lot of ligand – gated ion channels have been identified as certain drug targets, and most of them are targets for neurotransmitter interaction and nervous signal transmission.

Membrane transporters, transmembrane proteins involved in the movement of small molecules, or macromolecules, such as hormones, immunoglobulin and other proteins across the membrane, can play a vital role in determining drug pharmacokinetics, safety and efficacy as they are implicated in the process of drug absorption and elimination [19-21]. The drug targeted membrane transporters are mainly carrier mediated transporters, which interact with specific ligand for transportation activation. These carriers mediated transportation can be divided into facilitated diffusion and active transport according to ATP consumption during the transportation process. The active transport occurs when the transported molecules are coupled to ATP hydrolysis, which provide the energy for molecular transportation regardless of the concentration gradient. One of the most famous active transport proteins are the ATP-Binding Cassette (ABC) transporters, which depend upon ATP binding for molecular transportation and the mutation of these transporters can lead to different diseases, such as cystic fibrosis, adrenoleukodystrophy, and drug-resistant tumors [22, 23]. The facilitated diffusion transporters are the proteins that have a specific binding site for the transported molecules, and the binding causes the conformation change of transporter for the binding molecules to be released through concentration gradient without consumption of any energy. These type of transporter possess significant potential in drug absorption and elimination for drug screening and optimization. One important example is the glucose transporters (GLUT), which are important for the understanding of type II diabetes.

The last but the most important group of transmembrane proteins in drug discovery are the membrane receptors, which serve as receptors for neurotransmitters, peptide hormones and growth factor and constitute more than half of the drug targets. Some neurotransmitter receptors have been mentioned in previous ligand – gated ion channel section. The other membrane receptors, instead of opening the channel, act by the regulation of intracellular proteins for different physiological and pathological functions. These membrane proteins normally consist of three major domains: an extracellular binding domain, a hydrophobic transmembrane domain, and an intracellular functional domain, either an enzyme or other proteins for various functions. Ligand binding to the extracellular domain of these membrane receptors will initiate a chain of conformation change and intracellular reactions, ultimately reaching the targeted cell nucleus and leading to certain changes in gene expression, which is also the typical therapeutic process for drug intervention. According to the structure and functions, membrane receptors can be divided into 3 classes: the ion channel – linked receptor (mentioned as ligand – gated ion channel), the enzyme – linked receptor and the G protein – coupled receptor (GPCR). GPCR is one of the largest, most versatile group of membrane receptors, and also the most pharmaceutically important ones, accounting for over 50% of all human drug targets and involving in a wide range of disease conditions including cancer, cardiovascular, metabolic, CNS and inflammatory diseases [24, 25]. The GPCR family receptors are all structurally and functionally related, characterized by seven transmembrane spanning α helices and the intermediary action of G proteins. The binding interactions between an agonist and GPCR will induce a conformation change that activate the bound G protein, which will dissociate

from the receptor and transduce the signal to intracellular targets for different functionalities [26].

In contrast to GPCR, other membrane receptors are directly linked to intracellular enzymes, termed as the enzyme – linked receptors, in which the largest family receptors are receptor tyrosine kinases (RTKs). RTKs receptors can phosphorylate their substrate proteins on tyrosine residues for signal transduction, serving as high affinity receptors for many peptide growth factor, cytokines, and hormones. These receptors all have the common structure, consisting of an N-terminal extracellular ligand-binding domain, a single transmembrane α helix, and a cytosolic C-terminal domain with protein-tyrosine kinase activity. Up to now, more than 50 RTKs have been identified, and the majority of these receptors are for growth factors and hormones like epidermal growth factor (EGF), platelet derived growth factor (PDGF), fibroblast growth factor (FGF), hepatocyte growth factor (HGF), insulin, and nerve growth factor (NGF), which are particularly involved in the control of cell growth and differentiation. Therefore, the upregulation of these receptors will lead to uncontrolled cell dividing, resulting in various carcinomas.

After introduction of the different types of membrane proteins, it is evident that membrane proteins are critical for the understanding of cellular communication processes, validation of biomarkers, and screening of drugs. Despite their importance, membrane proteins are notoriously difficult to prepare in pure form and hard to get the correctly folded form in sufficient quantity for drug discovery purposes. The challenge of membrane proteins expression is that their expression can be toxic to cells or cause inclusion bodies, affecting the protein yield, purification and research period. Therefore, the quantification

of ligand – protein interaction in their natural lipid environment on cell surface is of great significance for drug discovery.

1.3 Binding Kinetics

As has been pointed out, the quantification of ligand – protein interaction is of great significance in drug screening and optimization, in which relevant binding parameters can well be used to characterize the drug efficacy and potency. In most cases, the ligand – protein binding in biological and pharmaceutical study is a highly selective and reversible process, which can be illustrated as the simplest 1:1 stoichiometry shown below:

$$P + L \underset{k_d}{\overset{k_a}{\rightleftarrows}} PL$$

P represents the membrane protein, which could be a receptor, ion channel or transporter, while L represents the ligand molecule, which could be the neurotransmitter, hormone, antibody and other drug molecules. PL is the binding formed biomolecular complex. The association rate constant k_a (in the unit of $M^{-1}s^{-1}$) and dissociation rate constant k_d (in the unit of s^{-1}) are the binding kinetic constants, which can be used to describe how fast a ligand binds to the membrane protein and how long it keeps bound with the receptor. These binding kinetic values can fully characterize the protein – ligand binding process, providing comprehensive information in drug evaluation.

The binding affinity is the most used parameter for the quantification of the ligand – protein binding interaction, which is described by the equilibrium dissociation constant, K_D (in the unit of M). K_D is defined as the ratio of molecules concentrations in equilibrium state:

$$K_D = \frac{[P][L]}{[PL]}$$

And the value of K_D is equal to the ligand concentration that binds to half of the membrane protein site. Therefore, K_D can be directly derived by measuring the equilibrium concentration ratio between ligand, membrane protein and the formed complex under different ligand concentrations. The stronger the ligand is bound, the smaller K_D will be obtained for drug potency evaluation, normally in the range of nM for good drug candidates. However, binding affinity cannot characterize the whole binding process. When in equilibrium state, the formation of the molecular complex and the dissociation of this complex reach the balance, which means:

$$k_a[P][L] = k_d[PL]$$

Thus, the equilibrium constant K_D can also be calculated by the binding kinetics k_a and k_d:

$$K_D = \frac{k_d}{k_a}$$

As the ratio of dissociation rate to association rate, K_D lost the exact rate information for ligand binding process, not being able to illustrate how fast the ligands bind to the protein and how long the ligands keep bound with the protein. To fully characterize the molecular interaction with membrane protein, the binding kinetic constants need to be quantified. Therefore, the real time quantification of the whole binding process is important. **Error! Reference source not found.** is the reprehensive of the real time binding curve, in w hich association process, equilibrium state and the dissociation process are illustrated.

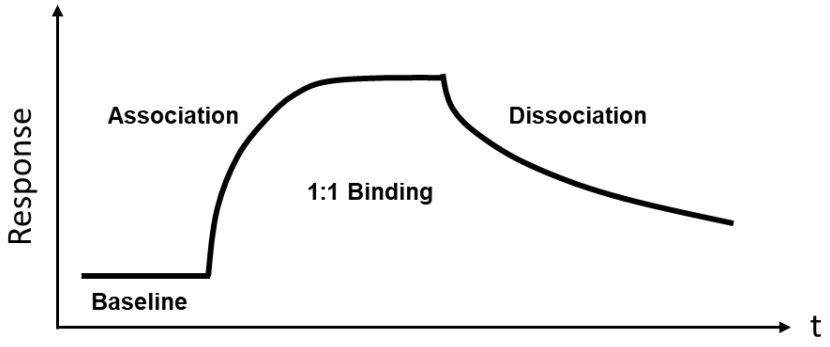

Figure 1.3 A representative binding curve in real time measurements.

1.3.1 Association Process

The association process is the first phase in the molecular interaction measurements. When the ligand molecules diffuse to the binding proteins, the binding interaction will occur. The rate of association, number of binding events per unit of time, equals:

$$[Ligand] \cdot [Protein] \cdot k_a \tag{1.1}$$

Once binding interaction occurs, the ligand and protein will form the protein-ligand complex for a random amount of time. The rate of dissociation, number of dissociation events per unit of time, equals:

$$[Protein \cdot Ligand] \cdot k_d \tag{1.2}$$

The binding interaction between immobilized protein (P) and ligand (L) can be assumed to follow the first order kinetics [27]. Therefore, during the association process, the complex [PL] increases as:

$$\frac{d[PL]}{dt} = k_a \cdot [P] \cdot [L] - k_d \cdot [PL] \tag{1.3}$$

The association rate constant k_a describes the rate of protein-ligand complex formation, indicating how fast the interaction occurs. The units of k_a are $M^{-1}s^{-1}$ and are

typically between 10^3 and 10^7 for biological application. The dissociation rate constant k_d describes the stability of protein-ligand complex, indicating how long the bond remains. The units of k_a are s^{-1} and are typically between 10^{-1} and 10^{-6} for biological application.

Assuming that the ligand concentration is constant and the maximum concentration of the protein is R_{max}, the protein-ligand complex concentration at time t is R_t, the free protein concentration at time t can be described as (R_{max}-R_t). Then, equation 1.3 can be rewrite as:

$$\frac{dR_t}{dt} = k_a \cdot (R_{max} - R_t) \cdot [L] - k_d \cdot R_t \quad (1.4)$$

By solving the differential equation 1.4, the association equation can be written by:

$$R_t = \frac{[L]R_{max}}{k_D + [L]} [1 - e^{-(k_a[L] + k_d)t}] \quad (1.5)$$

By fitting the binding association data with the kinetic equation 1.5, the binding kinetic constants can be derived.

1.3.2 Equilibrium State

When the binding association process continues for long enough time, the interaction will reach the equilibrium state, in which the formation of the protein-ligand complex equals to the breaking of the protein-ligand complex. At this state, the equilibrium constant k_D can be measured by:

$$K_D = \frac{[P][L]}{[PL]} = \frac{k_d}{k_a} \quad (1.6)$$

At equilibrium, the association equation can be written as:

$$\frac{dR_t}{dt} = k_a \cdot (R_{max} - R_{eq}) \cdot [L] - k_d \cdot R_{eq} = 0 \quad (1.7)$$

Equilibrium constants are determined with high sensitivity when the ligand concentration is equal to the dissociation constant k_D, which gives half of the maximum responses. Besides, equilibrium measurements are not affected by mass transport and ligand rebinding. So it is important to evaluate the data with equilibrium fitting.

An important experimental consideration is the time taken to reach equilibrium. From the integrated equation, the time required (t_r) to reach a fraction of equilibrium ($r=R/R_{eq}$) can be derived as:

$$R_{eq} = \frac{k_a[L]R_{max}}{k_d+k_a[L]} \tag{1.8}$$

$$t_r = \frac{-\ln(1-r)}{k_d+k_a[L]} \tag{1.9}$$

When the ligand concentration is equal to the equilibrium constant K_D, the time taken to reach 90% equilibrium is about $1/k_d$.

1.3.3 Dissociation Process

When the equilibrium is reached in the binding process, the ligand solution will be changed to buffer solution to start the dissociation process. At this point, the ligand concentration will drop to zero and the protein-ligand complex will dissociate, and the dissociation process can be described as:

$$\frac{dR_t}{dt} = -k_d \cdot R_t \tag{1.10}$$

Similarly, by solving this differential equation, the dissociation equation can be written as:

$$R_t = R_0 e^{-k_d(t-t_0)} \tag{1.11}$$

Normally, for the binding kinetic curve fitting, the dissociation rate constant will first be fitted with the dissociation equation. Then, with the fixed dissociation rate constant, the association rate constant and maximum responses will be fitted with association equation.

1.4 Molecular Interaction Detection Assays

Molecular binding to membrane proteins is critical for both cellular function study and drug development, which has motivated researchers to develop various detection technologies. A list of the binding detection assays and brief description of each method is presented in Table 1.1, from which it is easy to find out all the assays can be divided into two categories: labeled and label – free binding assays.

Labeled assays, including enzyme linked immunosorbent assay (ELISA), radioactive and fluorescent labeling assays, require different labeling or enzyme linking to measure the protein – ligand binding, which can arise a lot of issues. First of all, the labeling step usually takes long time and tends to be expensive. Secondly, the labeling molecules may intervene with the interaction between ligand and protein, leading to the activity change of the target protein. Third, all these labeled assays are end – point detection, which can only quantify the binding affinity for equilibrium binding, no kinetic constant provided. However, the labeled detections, i.e. radioligand based detection or ELISA, are still the most used assay in the high throughput screening process for drug development. It is mainly because these methods have high sensitivity and can easily be compatible with automated plate system.

In contrast, the label – free detection assays directly measure the protein – ligand binding interaction without any tagging process, which can save a lot of effort for label development. Furthermore, these detection methods can measure not only the affinity information, but also the binding kinetics in real – time, providing more comprehensive information to fully understand the binding process. As listed in Table 3, many label – free approaches have been developed, including the most popular surface plasmon resonance (SPR) biosensors that translate molecular interaction into refractive index, quartz crystal microbalance (QCM) that measures biomolecular interactions by sensing the mass change, and back scattering interferometry that measure back scattering light interference.

Table 1.1 Ligand binding assays

Group of assays	Assay	Mechanism	Advantages	Disadvantages
Labeled ligand binding assays	Enzyme-linked Immunosorbent Assay (ELISA)	ELISA applies enzyme linked antibody binding for specific binding.	ELISA is a gold standard for protein study. Quick and easy.	Enzyme labeling effects, cross reaction.
	Radioligand binding assays	Radioactively labeled ligand binding to target protein	Most popular assay for membrane protein. Robust and precise.	Radioactive safety issues. High cost for radioactivity handling.
	Fluorescent ligand binding assays	Fluorescent labeled ligand binding to target protein	Wide spectrum of wave lengths for multiple colors detection	Different fluorescence interference, labeling issues.
Label - free ligand binding assays	Quartz Crystal Microbalance (QCM)	QCM detects the mass change during binding interaction.	Label free, real time detection.	Low throughput, not suitable for small molecules.
	Bio-layer Interferometry (BLI)	BLI uses a spectrometer to detect interference patterns formed by light reflected from an optical layer and a bio-layer containing target protein.	Effective assay to study binding kinetics.	This assay has been validated mostly for small molecule detection.
	Back Scattering Interferometry (BSI)	BSI detects the interference pattern formed by the back scattering light from the binding sample.	Label free, solution free.	No binding kinetics. Not suitable for cell based assay.
	Isothermal Titration Calorimetry (ITC)	ITC measures the binding enthalpy variation by sensing the heat caused by the binding reaction	This method is useful for detecting highly potent and entropy-driven ligands.	Low throughput and sensitivity, and requires large sample volumes.
	Surface Plasmon Resonance (SPR)	SPR applies light-excited surface plasmon polaritons to track the binding of ligands to the receptors bound to a gold surface	Most popular label-free ligand binding assay. This assay can be used to determine binding kinetics.	Not suitable for small molecules.

1.4.1 Enzyme Linked Immunosorbent Assay (ELISA)

Enzyme – linked immunosorbent assay (ELISA) is a gold standard for protein study, which has been designed as a plate based assay for high throughput detection and quantification of different molecules, such as proteins, peptides, antibodies and small molecules. In ELISA measurement, the targeted proteins, termed as antigen, must be immobilized to a solid surface, and an antibody linked to an enzyme is introduced for specific binding interaction. The signal detection is accomplished by the assessment of enzyme activity via incubation with a substrate to produce measurable product, usually a color change.

There are four different assay formats used in ELISA: direct, indirect, sandwich and competitive ELISA, as shown in Figure 1.4. In direct ELISA, the target antigen is immobilized directly to the surface and an enzyme labeled primary antibody is used to detect the binding of antigen. Although easy to operate, the direct ELISA is not widely used in binding detection, but quite common for immunohistochemically staining of tissues and cells. There are several reasons. First, immunoreactivity of the primary antibody may be adversely affected by the labeling with enzymes. Second, labeling primary antibody for each specific antigen is time - consuming and expensive. Last, direct ELISA shows minimal signal amplification. Indirect ELISA uses an enzyme - conjugated secondary antibody for signal generation while primary antibody for the binding interaction. In the indirect ELISA, the immunoreactivity of the primary antibody is fully retained as it is not labeled. And with a wide variety of labeled secondary antibodies available commercially, indirect ELISA is much more versatile because many primary antibodies can be made in

same species and the same labeled secondary antibody can be used for detection. Furthermore, the sensitivity of indirect ELISA is increased as the primary antibody can contain several epitopes to bind with the labeled secondary antibody, allowing for signal amplification. However, the cross – reactivity may occur with the secondary antibody, resulting in nonspecific binding, and an extra incubation and washing steps are required. In sandwich ELISA assays—the antigen to be detected is sandwiched between a layer of capture antibody and a layer of detection antibodies. This assay is mostly used in the protein detection, which provides high specificity in detection because the capture assay format excludes many nonspecific adsorbed proteins on the substrate, allowing for direct protein detection in physiological fluids, such as serum and blood. The sensitivity of this assay is also high as several second antibodies can be applied for signal amplification. One requirement for this assay is that the target antigen need to have at least two different antibody binding sites. The last assay is competitive ELISA, which is commonly used when the antigen is small and has only one epitope, or antibody binding site. One strategy for this assay is to use a labeled standard antigen (purified) instead of a labeled antibody. Unlabeled target antigen from the sample competes with the labeled standard antigen for binding to the same capture antibody. A decrease of signal from standard antigen is observed compared with the wells with standard antigen alone, indicating the inhibitory effect of the target antigen. This assay allows for the detection within the crude or impure samples and the result is highly reproducible. However, the overall sensitivity and specificity is low.

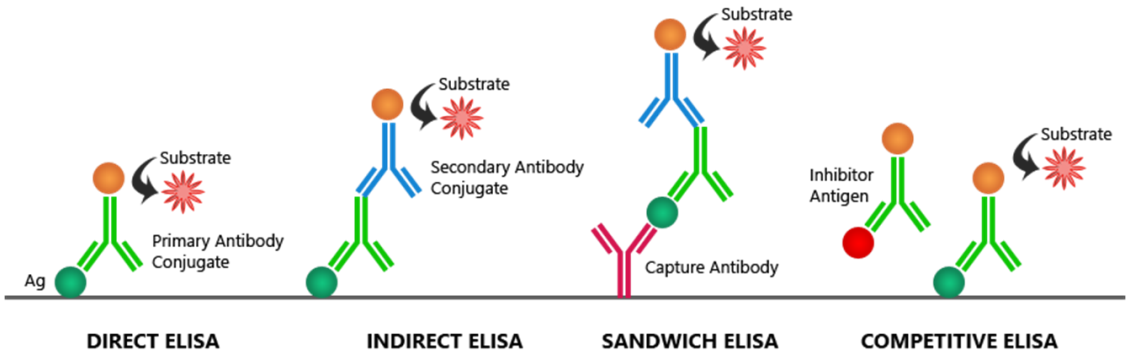

Figure 1.4 Four different ELISA formats. Direct, indirect, sandwich and competitive ELISA. [From Bosterbio at https://www.bosterbio.com/]

However, there are several limitations for ELISA. First, the secondary antibody detection involved assays are time consuming, requiring hours for signal detection. The washing between every steps is laborious. Second, as a labeled method, ELISA is an end-point detection assay which can only get binding affinity. And the enzyme tagging will intervene some of the binding interactions, leading to false results. Third, ELISA is mostly operated with purified proteins, which is sometimes expensive and laborious. More seriously, the purified proteins may lose their original structures and functions after being isolated from the native membrane environment.

1.4.2 Fluorescence labeling Assay

Fluorescence labeling binding assays are the promising alternatives to radioligand binding assay. Compared with radioligand detection, these labels are much safer with no health concerns or safety issues involved, and the detection methods can be more sensitive and versatile. However, when conjugate the fluorescent probe with the ligand, it adds steric hindrance as well as hydrophobicity modifications, which can significantly alter the

pharmacological properties of the ligand, sometimes diminishing its affinity to such an extent that it can become useless in pharmacological studies.

In fluorescence labeling binding assay, the fluorescence intensity is used to quantify the signal, which can be measure with different techniques. The currently effectively used techniques in protein-ligand binding include fluorescence anisotropy, fluorescence correlation spectroscopy, time-resolved fluorescence, fluorescence polarization, fluorescence and bioluminescence resonance energy transfer.

The most preferred detection technique in fluorescence labeling binding interaction is fluorescence resonance energy transfer (FRET) based assay. FRET is a distance dependent interaction between the electronic excited states of two dye molecules, one donor and one acceptor. When the donor molecule is excited, the energy will transfer to the acceptor molecule through nonradiative dipole-dipole coupling. The efficiency of this transfer is dependent on the inverse sixth power of the distance between two dye molecules, making it extremely useful in biological molecules interaction that produce change in molecular proximity. The distance at which the energy transfer efficiency is 50% efficient is defined by the Forster radius (R_0), which is typically in angstrom ranges.

To implement FRET based assay, two fluorophores have to be energy compatible, that the absorption spectrum of the acceptor must overlap the fluorescence emission spectrum of the donor, and close enough, typically 10 -100 Å distance. Figure 1.5 shows one example of the direct detection of binding interaction with FRET. Two biomolecules are each attached with a fluorescent label, one as donor and the other one as acceptor. When the two molecules are free in the medium, no FRET signal will be detected. Otherwise, as

soon as the two molecules bind together, the two fluorophores will be close enough to generate the FRET signal. Emission light from the acceptor fluorophore will show up to quantify the binding interactions.

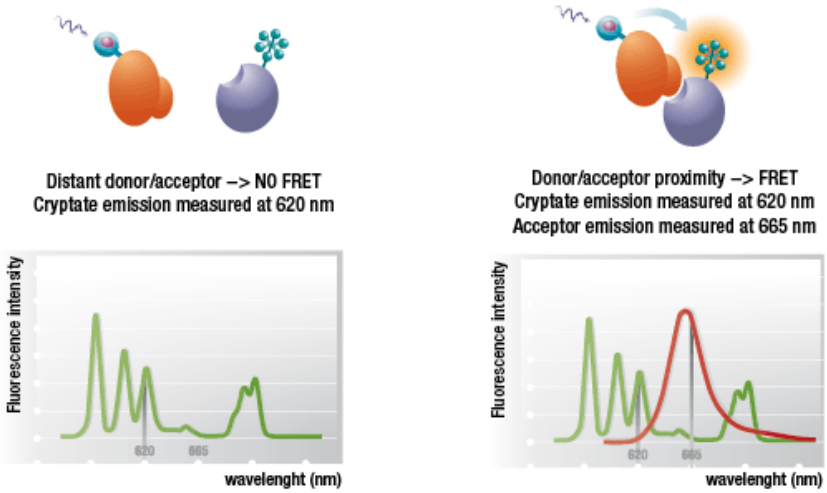

Figure 1.5 Detection mechanism of FRET. [From Cisbio at https://www.cisbio.com/drug-discovery/assay-kits-reagents]

In the traditional FRET assays, one big problem is the noise in the background that derived from scattered excitation light and significantly interfered by fluorescence from coexisting material in the sample (fluorescent compounds and dust), making it very difficult to obtain a highly sensitive measurement. To solve this problem, the time resolve FRET is developed, which combines the time-resolved (TR) measurement with FRET, allowing the elimination of short-lived background fluorescence. In TR-FRET, the donor fluorophores used are mainly lanthanide, either Europium cryptate (Eu3+ cryptate) or Lumi4-Tb (Tb2+ cryptate) mostly, which are not subject to photo-bleaching and have much longer fluorescence lifetimes. Whereas classical fluorophores have fluorescence lifetimes in the range of a few nanoseconds, lanthanides are characterized by much longer

fluorescence lifetimes, between several hundred microseconds to a few milliseconds. Thus, when introducing a time delay (50-150 microseconds) between the initial light excitation and fluorescence measurement, all the non-specific short-lived fluorescence emissions will be minimized, providing much better signal to noise ratio.

TR-FRET is a highly sensitive, flexible and robust assay for the detection of molecular interaction *in vitro* and has been frequently used in primary and secondary drug screening process. Being miniaturized into the 384 and 1536 well plate formats, TR-FRET is fully compatible with the automated liquid handling and robotic detection system, and has been applied to many antibody-based assays including GPCR signaling (cAMP and IP-One), kinases, cytokines and biomarkers, bioprocess (antibody and protein production), as well as the assays for protein-protein, protein-peptide, and protein-DNA/RNA interactions. However, there still exists some intrinsic limitations for these assays, for example, quenching generated by external interactions with the intramolecular excitation process (electron transfer, FRET, and bleaching) and fluorescence of library compounds or biological proteins. Also, false positive and false negative situations, although highly improved, still exist in various experiments.

1.4.3 Quartz Crystal Microbalance (QCM)

Quartz crystal microbalance (QCM) is a simple, cost-effective, label-free mass sensing technique, which can be used for the determination of binding kinetics. During the past several years, QCM has been rapidly evolved in the measurement of various bioanalytes, which can used for different applications such as the study of the kinetics of protein adsorption and desorption in real time, the determination of the thickness and

hydration level of protein films, and the characterization of the affinity between surface-bound receptors and soluble ligands [28-31].

The signal transduction mechanism of QCM is based on the piezoelectric effect of a quartz crystal, which was first discovered in 1880 [28]. The typical structure of QCM consists of a megahertz piezoelectric quartz crystal sandwiched between two gold electrodes. By applying a proper electric field at the electrodes, the crystal sensor will oscillate with a characterized frequency, termed resonant frequency. Then, even a very small mass change on the surface of crystal sensor, as low as subnanogram per cm^2, will alter the resonant frequency. As Sauerbrey demonstrated in 1959, the change in resonant frequency is linearly proportional to the change in mass coupled to the surface of the sensor crystal [28],

$$\Delta m = -\frac{C}{n}\Delta f$$

$$C = \frac{t_q \rho_q}{f_0}$$

where Δf is the change in resonant frequency at the vibrational mode number n, Δm is the mass change on the crystal surface, and C is the mass sensitivity constant of the instrument, which is related with the thickness of the quartz, t_q, the density of the quartz, ρ_q, and the original resonant frequency for the quartz, f_0. For example, this C constant for a 5-MHz crystal is 17.7 ng/Hz-cm^2. For different applications, various categories of target absorbing layers should be coated on the crystal surface and the targets absorbing on the surface will change the mass of the crystal and hence the resonant frequency for signal transduction. This process is highly sensitive and can be detected in real-time.

However, in order to hold Sauerbrey relationship, there are several requirements that must be fulfilled. First, the adsorbed mass must be small relative to the mass of the quartz crystal; second, the mass adsorbed is rigidly adsorbed; and third, the mass adsorbed is evenly distributed over the active area of the crystal, which are not always true especially when using the QCM for liquid applications. In the liquid applications of QCM, the mass change is often incorporated with the viscous and elastic changes, which violated the assumption of the Sauerbrey relation stating that the mass adsorbed must be rigidly adsorbed. To solve this problem, two main approaches are used, both of which monitor the decay of a crystal's oscillation (frequency or impedance) after a rapid excitation, since the decay rate is proportional to the energy dissipation of the oscillator. Thus, QCM can then be cooperated with the energy dissipation monitoring, which can not only detect the subtle mass changes in sensor surface, but also the viscosity change in the solution-surface interface.

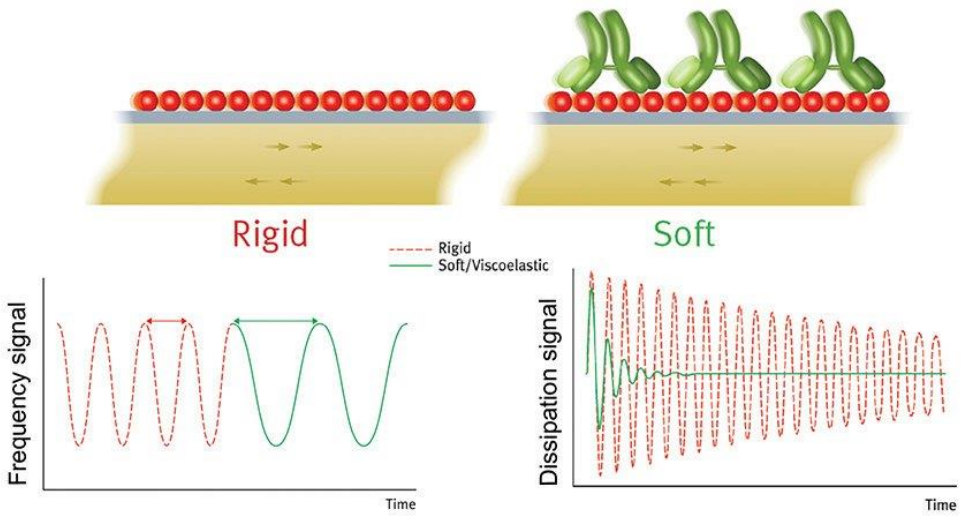

Figure 1.6 The QCM-D principle. [From Biolin Scientific at https://www.biolinscientific.com/]

QCM has been widely used with different biological systems, such as lipid bilayers, cells and bacterial. There is one commercial instrument (Q-Sense Gothenburg, Sweden), celled quartz crystal microbalance with dissipation monitoring (QCM-D), which can simultaneously measure the changes in both frequency (Δf) and dissipation (ΔD) at various vibrational modes of the crystal, as shown in Figure 1.6. The energy dissipation measurement of QCM-D is particular advantageous for the sensing of changes in surface elastic properties which can be used to characterize conformational and structural changes in molecular layers or whole cells on the sensor surface. These capabilities have great potential in drug discovery, allowing both detection of potential new pharmaceutical candidates in drug target screening assays, and improved understanding of target interactions mechanisms. QCM-D provides a sensitive platform for cell-surface interactions which can be monitored in real-time. Figure 1.7 shows the human carcinoma cells attached to the sensor ex-situ and their interaction with the epidermal growth factor (EGF). The binding of EGF to the EGF receptor (EGFR) results in cytoskeleton rearrangements in the cells which are successfully probed by QCM-D as changes in the viscoelasticity of the cell layer [32].

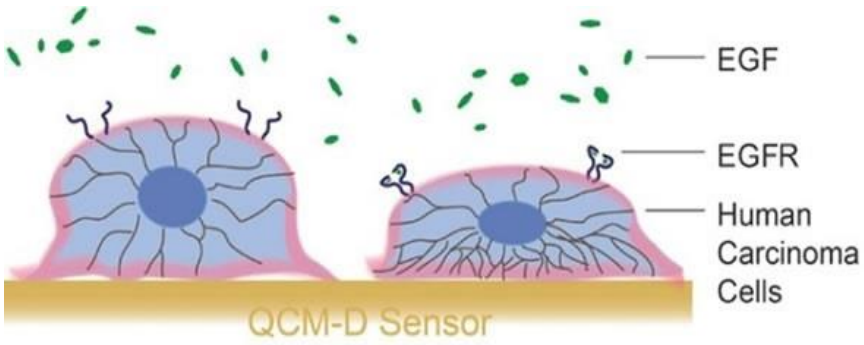

Figure 1.7 The EGF interaction with cells attached to QCM-D surface.[33]

QCM has a lot advantages in not only protein-ligand binding detection, but also other biochemical and biological applications. However, there are still some limitations. First, the accuracy and precision of this method is affected by the temperature and humidity changes, which can also induce the volatilization and condensation problems. Second, it is difficult to obtain an even distribution of the particle on crystal surface, which is important for signal transduction. Last, system calibration and frequency cleaning of the sensor surface are both required in every measurement, which add to the complexity of the detection procedure.

1.4.4 Bio-layer interferometry (BSI)

Bio-layer interferometry is a label-free technology that enables the real-time measurements of molecular interaction. BSI is based on the optical interferometry, which analyze the interference pattern of white a light reflected from two surfaces. One surface is a layer of immobilized biomolecules on the biosensor tip, the other one is an internal reference layer. The binding between the biomolecules immobilized on the biosensor tip surface and the analytes in solution produces an increase in optical thickness at the

biosensor tip, which in turn generate a shift (Δλ) in the light interference pattern that can be measure by a spectrometer for real-time signal detection (Figure 1.8).

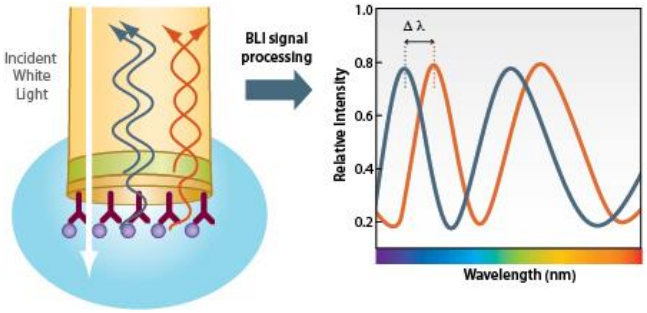

Figure 1.8 The working principles of bio-layer interferometry sensor. [From ForteBio at https://www.fortebio.com/]

BSI biosensor is a highly robust system in the measurement of biomolecular interaction. The typical configuration of this system is based on optical fibers, which allow the utilization of an innovative sample delivery system. Instead of using a fluidic system for sample delivery, the optical fiber based BSI sensors are moved and dipped into the sample wells, termed as 'dip and read' biosensors. A common binding measurement sequence is performed by dipping the sensors into different reagent solutions, such as the buffer and free ligands solution, which adds robustness to the systems and decreases maintenance and operating costs. BSI has been widely used in the kinetic applications targeting different biomolecules, including DNA, RNA, and proteins [34].

One commercially available system based on BSI technology is released by FertoBio (Menlo Park, CA) in 2006, called Octet system, which uses disposable sensors with an optical coating layer at the tip of each sensor. This optical surface is coated with a proprietary biocompatible matrix that can interact only with the targets and minimize the non-specific binding to the surface. When the ligands bind with the immobilized matrix,

the optical interference pattern will change and the binding signal will be detected in real-time. The unbound ligands in solution and other changes to the matrix do not change the interference pattern, which enables the use of crude cell lysates or periplasmic samples, such as the common cell culture media, serum-containing media and DMSO-containing media, dramatically reducing the sample preparation. Octet biosensors are now configured a standard 96-well format for high throughput and automatic handling. Various surface chemistry coating layers are available for different applications. To date, over 2.5 million biosensor assays have been run on Octet systems, attesting to the high reproducibility, accuracy, precision and robustness of the platform.

This approach has some disadvantages. First, for the biomolecule coating in multiple sensors, it is not possible to achieve identical coatings results. So it is not guaranteed that each sensor has an equal performance in later measurements. Second, this approach requires large sample volumes. A minimum sample volume of 180 μL is required in a standard 96-well microplate to make accurate measurements because smaller volumes than this can generate measurement artefacts due to internal reflections. Last, the limit of detection for BSI is around 0.1 ng/cm^2, which makes it difficult to follow the adsorption of small molecules.

CHAPTER 2 QUANTIFICATION OF MOLECULAR INTERACTION WITH MEMBRANE PROTEIN BY SURFACE PLASMON RESONANCE IMAGING

2.1 Introduction

Molecular interactions with membrane proteins play critical role in both studying cellular functions and screening new drugs. The quantification of the membrane protein density and molecular interaction process provides valuable information for biomarker identification and drug discovery. To fully preserve the function of membrane protein, it is important to detect the membrane protein interaction in their original cell surface without external labeling. Therefore, a label-free method for *in situ* quantification of membrane protein interaction is needed.

Various methods have been developed to measure the membrane protein interaction on the cell surface, most of which are using radioactive or fluorescent labeling. Surface plasmon resonance (SPR) is the typical label-free method that measure the kinetics of molecular interaction.[35] Surface plasmon resonance imaging (SPRi) extends the SPR measurement to microarray [36-41] and enable direct measurement of molecular binding kinetics on the surface of cells [42, 43] and bacteria.[44]

In this chapter, we report the *in situ* quantification of the membrane protein drug target binding interaction with its antibody drug for the establishment of a cell based label-free SPRi platform for drug evaluation [45]. The SPRi setup is built for both temporal and spatial detection of the binding interaction between membrane protein and the specific antibody. Epidermal growth factor receptor (EGFR, also known as ErbB-1 or HER-1) was used as an example of the membrane protein drug target, which has been associated with a

variety of solid tumors and the control of cell survival, proliferation and metabolism. Quantification of EGFR expression level in cells membrane and the interaction kinetics with drugs are thus important for drug screening and disease treatment. A monoclonal antibody, anti-EGFR, was used to study the binding kinetics and affinity in EGFR overexpressed cells with single cell resolution and the ability to map cell-to-cell heterogeneity. The binding of the anti-EGFR to EGFR overexpressed cells was monitored in real time, and the binding kinetics with association rate constant (k_a) and dissociation rate constant (k_d) were determined. Additional measurement with different EGFR positive cell lines (A431, Hela and A549) was performed to study the cell line-cell line variation in both receptor density and binding kinetics. Furthermore, the binding kinetics of cell lines with different EGFR-expressing levels were compared, which reveals microenvironment in the cell membranes affecting the drug-receptor interactions.

2.1.1 EGFR Receptor

Molecular targeting therapy is an advanced cancer therapy, which can improve tumor-targeting specificity compared with the traditional chemotherapy and radiotherapy. Among all the identified targets, one promising molecular target is the epidermal growth factor receptor (EGFR, also known as ErbB-1 or HER-1) in cell membrane. EGFR plays an essential role in regulating normal cell signaling, and the mutation of EGFR leads to cell proliferation, angiogenesis, invasion, metastasis and inhibition of apoptosis, accounting for the pathogenesis and progression of cancer cells (Figure 2.1).[46-50] Therefore, *in situ* quantification of EGFR expression level in cell membrane, and ligand binding kinetics and affinity are of great importance for cancer diagnosis and treatment.

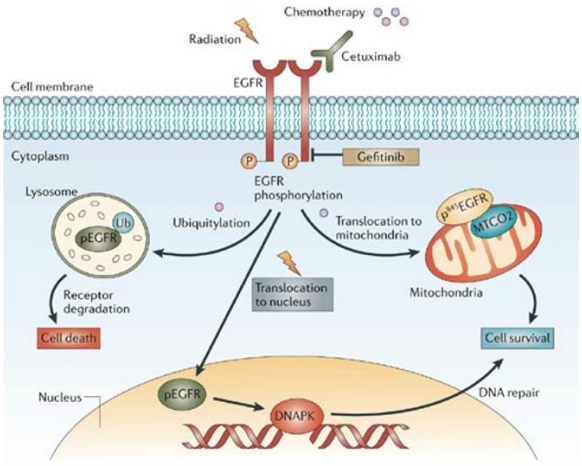

Figure 2.1 The signal transduction of EGFR activation.[51]

EGFR is a transmembrane protein, which consists of three major functional domains: an extracellular binding domain, a hydrophobic transmembrane domain and an intracellular tyrosine kinase domain.[52-55] When an epidermal growth factor (EGF) or transforming growth factor (TGF) ligands bind to the extracellular domain, EGFR undergoes a transition to form receptor homodimers or heterodimers with neighboring ErbB receptors, which activates the intrinsic receptor tyrosine kinase domain for signal transduction. Mutations that cause EGFR overexpression and constant activation often lead to uncontrolled cell dividing.[56-61] Therefore, quantification of EGFR expression density in cell membrane is a critical step for cancer diagnosis. Currently, the most used approach for receptor density measurement is radiolabeling assay [62, 63], which involves synthesis of radio-ligand and requires special training and safety protection. A label-free method is desired for rapid quantification of receptor density.

In order to prevent the unwanted downstream effects of EGFR signaling, two kinds of inhibitors have been proposed for cancer treatment: tyrosine kinase inhibitors targeting the intracellular domain and monoclonal antibodies targeting the extracellular domain. The

binding of these inhibitors to EGFR slows down or stops tumor cell growth.[64-71] Monoclonal antibodies targeting the extracellular domain of EGFR have been in various stages of pre-clinical development, and have shown good therapeutic efficacy for treatment of a number of cancers that have up-regulated EGFR expression levels.[46, 47, 68, 72, 73] The kinetic constants of the binding of these antibody drugs to EGFR are the key parameters to characterize the efficacy of these drugs.

2.1.2 Principle of Surface Plasmon Resonance

Surface Plasmon Resonance (SPR) is the most popular label-free technique, which has been widely used in various applications, such as the kinetic detection of biomolecular interaction, DNA hybridizations, metal ion concentrations, et al. SPR is an optical approach that measures the local refractive index change within the vicinity (~200 nm) of a metal surface, which has many advantages: (1) high sensitivity, (2) label-free detection, (3) real-time monitoring, (4) low volume sample consumption, (5) quantitative evaluation, and (6) determination of kinetic constants.

Surface plasmon resonance (SPR), to be simple, is the resonant oscillation phenomenon of electrons on metal surface when excited by the light evanescent wave.

To explicit explain the SPR theory, an electromagnetic plane wave that propagates in a medium with refractive index n can mathematically be described by an electric field E:

$$E = E_0 \exp(j\omega t - jk \cdot r) = E_0 \exp\left(j\omega t - jk_x x - jk_y y - jk_z z\right) \quad (2.1)$$

where E_0 is the amplitude of the electric field, ω is the angular frequency, k is the wave vector, r=(x,y,z) is the position vector. For the wave vector k, its direction is parallel to that of wave propagation, and the amplitude is given by

$$k = \sqrt{{k_x}^2 + {k_y}^2 + {k_z}^2} = n\frac{2\pi}{\lambda} = n\frac{\omega}{c} \tag{2.2}$$

where λ and c are the wavelength and propagation velocity in vacuum, respectively.

When a light is directed at the interface of two media with refractive index n_1 and n_2, respectively, the optical refraction will happen and follow the Snell's law. Assuming that k_z is 0, Snell's law is given by (Figure 2.2):

$$n_1 \sin\alpha = n_2 \sin\beta \tag{2.3}$$

or equivalently,

$$k_{x1} = k_{x2} = k_x \tag{2.4}$$

And then, combing eqs. (2.2) and (2.4), the y-component of the refracted light in medium 2 can be derived as

$${k_y}^2 = {n_1}^2 \left(\frac{2\pi}{\lambda}\right)^2 \left(\frac{{n_2}^2}{{n_1}^2} - \sin^2\alpha\right) \tag{2.5}$$

Now, if $n_1 > n_2$, it is quite possible that $\sin\alpha > n_2/n_1$, which means the right part of equation (2.5) is negative, and consequently, k_y is purely imaginary. In this case, the plane wave in medium 2 will only be parallel to the interface:

$$E_2 = E_0\, e^{-k_{y2}y} \exp(j\omega t - jk_x x) \tag{2.6}$$

with the amplitude of the electric field exponentially delaying along the y-direction with a characteristic distance. This electric field in medium 2 is termed as the evanescent field, which is generated in SPR for signal sensing and determines the properties that SPR is only

sensitive to change in the vicinity of the interface, and changing the refractive index will greatly influence the response [74].

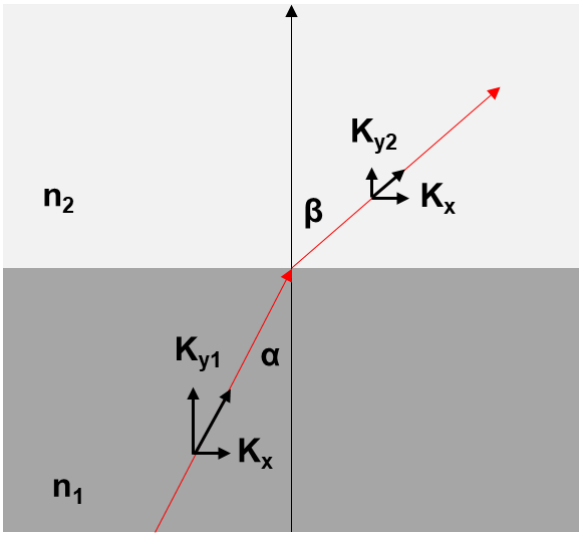

Figure 2.2 Optical refraction at the interface of two media.

Surface plasmon polaritons, shown in Figure 2.3, is non-radiative electromagnetic surface wave, expressed as

$$E = E_0 \exp(j\omega t - jk_x x - jk_z z) \quad (2.7)$$

where k_x and k_z are the wave numbers along x and z direction, respectively, and ω is the angular frequency.

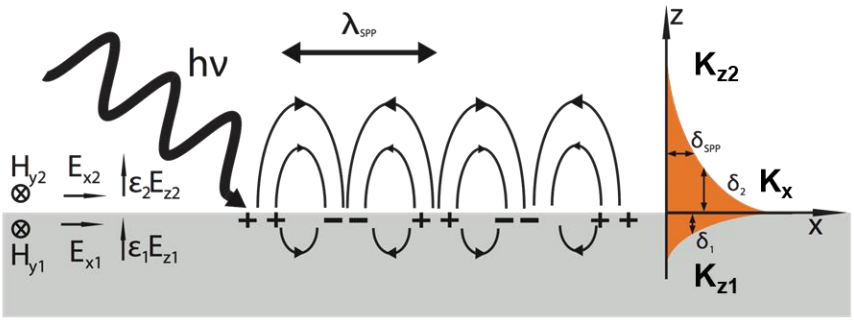

Figure 2.3 Surface plasmon polariton waves. [From Wikipedia] At the interface of the two materials, by solving Maxwell equations and using the boundary conditions, two equations are derived:

$$\frac{k_{z1}}{\varepsilon_1} + \frac{k_{z2}}{\varepsilon_2} = 0 \tag{2.8}$$

$$k_x{}^2 + k_{zi}{}^2 = \varepsilon_i(\frac{\omega}{c})^2 \tag{2.9}$$

where c is the speed of light, by combining these two equations, the dispersion relationship of surface plasmon polaritions is shown:

$$k_x = \frac{\omega}{c}(\frac{\varepsilon_1\varepsilon_2}{\varepsilon_2+\varepsilon_1})^{1/2} \tag{2.10}$$

As for metal, the dielectric function is

$$\varepsilon(\omega) = 1 - \frac{\omega_p{}^2}{\omega^2} \tag{2.11}$$

where ω_p is the bulk plasmon frequency

$$\omega_p = \sqrt{\frac{ne^2}{\varepsilon_0 m^*}} \tag{2.12}$$

Thus, the dispersion relationship was shown in Figure 2.4. When the dispersion relationship of the evanescent wave has intersection with this one, the surface plasmon resonance (SPR) will be excited.

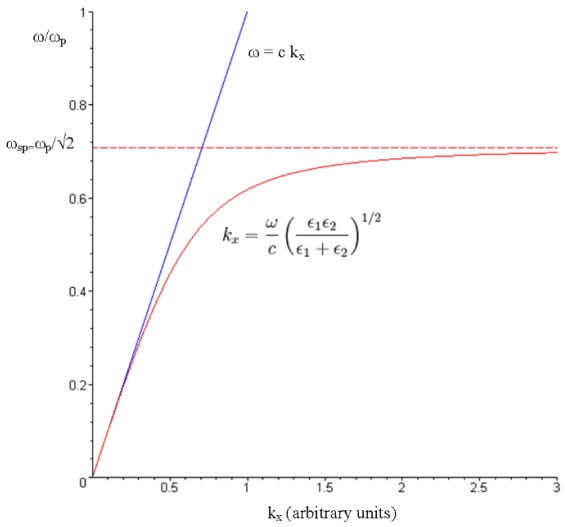

Figure 2.4 Dispersion relationship of SPPs. [From Wikipedia]

In order to realize the excitation of SPR, two different configurations as shown in Figure 2.5, which are developed by Otto [75] and Kretchmann [76], respectively. In both setups, p-polarized light is used because this particular polarization has the electric field vector oscillating in the normal direction to the plane of meatal surface, and the angle of incident light to a prism is θ. Reflected light intensity is recorded by photodiode or CCD camera for signaling. The difference in this two configuration is that Otto put the sample with lower optical density between the prism and metal, while in Kretchmann configuration the metal is between the prism and sample. In most cases, Kretchmann configuration is used because it is easy to facilitate and operate.

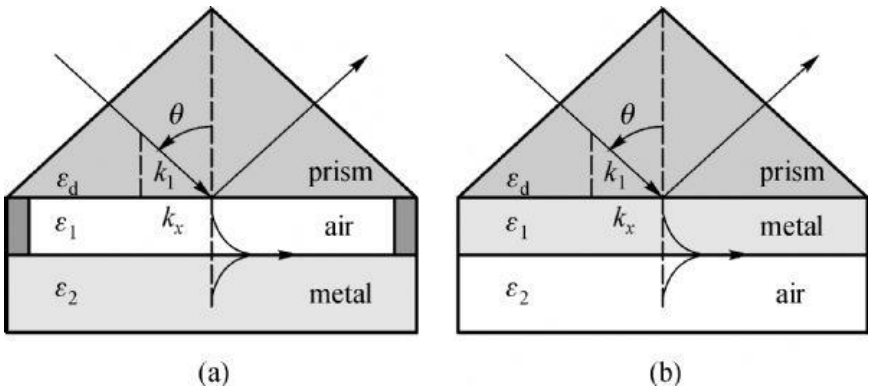

Figure 2.5 Configurations to excite SPR. (a) Otto; (b) Kretchmann.[77]

In Kretchmann configuration, the prism is used for the generation of surface plasmon resonance, in which dispersion relationship of light is given

$$k_x = k_1 \sin\theta = n_p k \sin\theta \tag{2.13}$$

$$\omega = \frac{ck_x}{n_p \sin\theta} \tag{2.14}$$

where n_p is the refractive index of prism and the dispersion curve is determined by both k_x and incident angle θ. As described in evanescent wave section, when the light transverses from dense medium (such as, prism) to light medium (such as, metal), the evanescent field can be generated, which is parallel to the media interface and decaying exponentially. The evanescent wave is able to couple with the surface plasmons in the metal film at a specific angle when the x-component wavevector of evanescent filed is consistent with that of SPPs.

Thus, with the certain light source, the x-component wavevector can be adjusted with a simple change of incident light angle. As shown in Figure 2.6, with the changes of incident angles, the slope of dispersion curve will change and at some point, it will intersect with that of SPP for surface plasmon resonance generation.

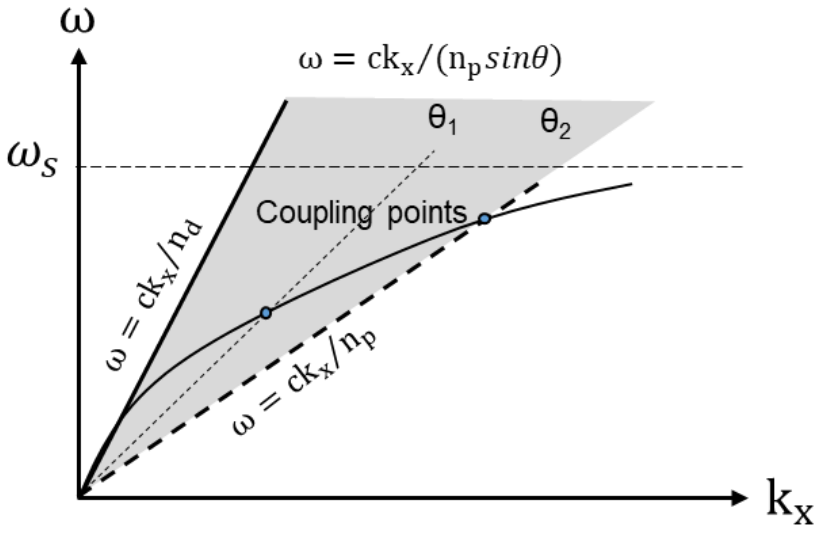

Figure 2.6 Coupling light wave vector to SPPs by tuning incident angle.

This excitation is known as wave vector matching. This causes energy from the incident light to be totally transferred to the metal film resulting in a reduction in the intensity of reflected light. As illustrated before, SPR cannot be achieved by direct illumination of metal surface with light. Wave vector matching does not occur in this situation because the light wave vector is always smaller than the wave vector that describes the surface plasmon polaritons. The prism is used to increase the light wave vector so that wave vector matching is possible.

In biomolecular interaction measurement, as shown in Figure 2.7, a typical SPR configuration consists a glass prism for light coupling, and metal film (mostly, gold or silver) for surface plasmon polaritons and sample layer for binding process. Normally, the receptors are immobilized on the metal surface, and the solution with targeted ligands is introduced for binding interaction. When the binding process proceeds, the refractive index of at the metal/dielectric interface will change, which induced the angle shift for resonance

dip. By fixing the detector at a specific angle along the resonance dip's linear regime, the reflected beam intensity is monitored as a linear function of refractive index change for real-time binding detection. The binding kinetics can then be derived from the typical binding curves.

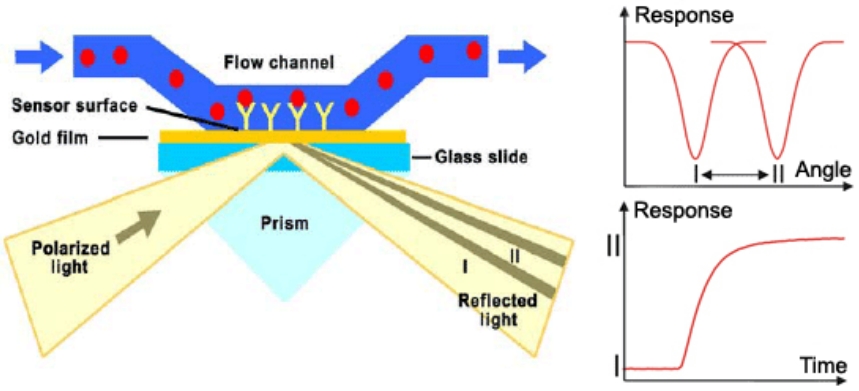

Figure 2.7 Schematic configuration of SPR in molecular binding interaction.[78]

As previous mentioned, by fixing the detector at a specific angle along the resonance dip's linear regime, the reflected beam intensity can be used as a linear function of refractive index change for signal transduction. When the detector used is a CCD camera, this detection system can be characterized as a SPR imaging system, which enables the visualization of the whole biochip. SPRi goes a step beyond the traditional setup, allowing high throughput screening of hundreds or thousands of samples [79, 80].

In typical SPRi system, as shown in Figure 2.8, a coherent polarized light beam is used instead of polychromatic light, which helps expand the light cover on a larger area of the sensing surface. The reflected light is captured by a charge-coupled device (CCD) camera for further imaging analysis. The high resolution CCD camera provides images across the array format in real-time detection of up to hundreds of active spots. Captured

images that show local changes at the chip surface can provide detailed information on molecular binding, interactions or kinetic processes [80]. Unlike conventional SPR, the measurement conducted by SPRI is stringently performed at a constant wavelength and a constant angle. Thus, changes in reflected light intensity are proportional to any variation of the refractive index near the metal surface.

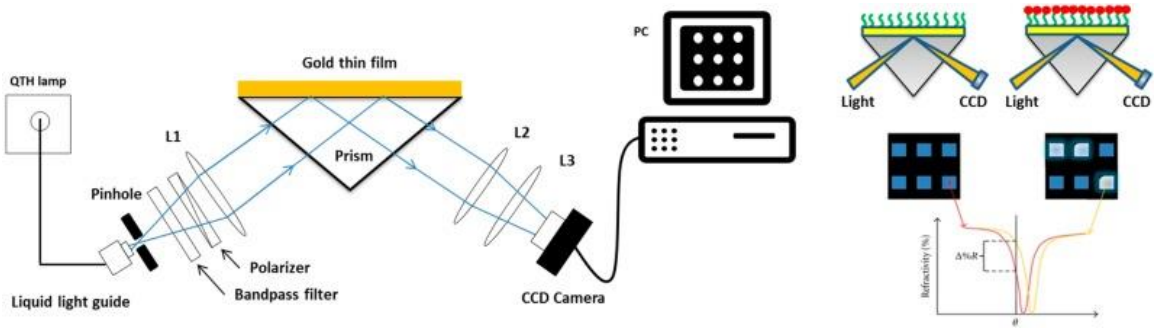

Figure 2.8 Schematic configuration of SPRi system and molecule interaction measurement. [81]

2.2 Materials and methods

Materials. Anti-EGFR monoclonal antibody (cat. no. 05-101) was purchased from EMD Millipore, which was dissolved as a 1 mg/mL stock solution, and stored in frozen aliquots. Anti-EGFR solutions used in the experiments were prepared by diluting the stock solution with phosphate buffer solution (PBS). Alexa Fluor 488 Goat Anti-Mouse IgG1 (γ1) Antibody (cat. no. A-21121) was obtained from Life Technologies. All reagents were analytical grade, purchased from Sigma-Aldrich, except those stated. Deionized water was used to prepare all the buffers.

SPRi setup. The prism based SPR imaging setup is a typical Kretchmann configuration, in which a collimated p-polarized light from a 680 nm light-emitting diode

(LED) was directed through a triangular prism onto the gold-coated glass coverslip placed on the prism [43]. The reflected beam was captured by a CCD camera (AVT Pike F032B) at a frame rate of 11 frames per second (fps) through a 12x variable zoom lens (Navitar). A Flexi-Perm silicon chamber (SARSTEDT) was placed on top of the gold chip to serve as a cell-culture well. A schematic diagram of the set-up is shown in Figure 2.9.

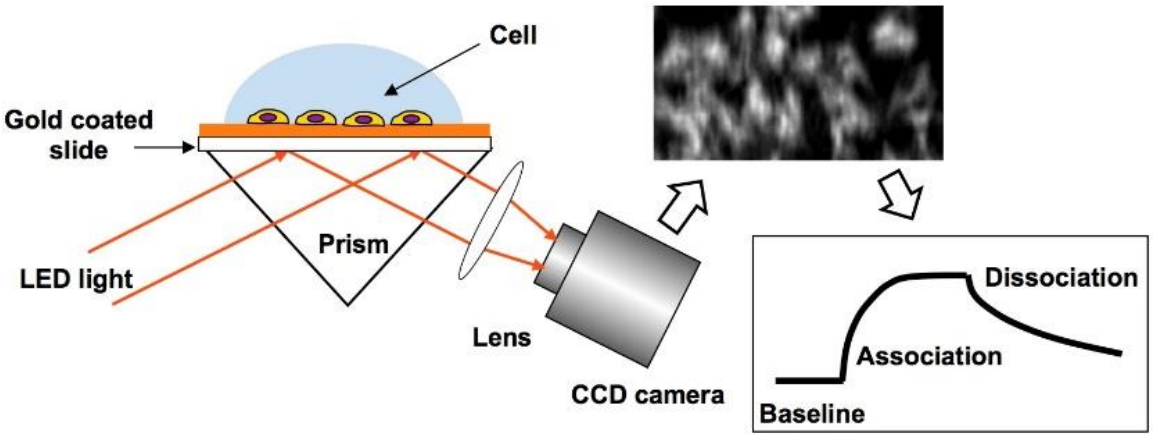

Figure 2.9 Schematic diagram of the SPRi setup.[45]

A gravity-based multichannel drug perfusion system (SF-77B, Warner Instruments, Connecticut) was used to deliver solutions to the target cells. The typical transition time between different solutions was about 1−2 s.

Cell Culture. A431, A549, HeLa, and HEK293 cell lines were obtained from the American Type Culture Collection (Rockville, MD). All the cells were cultured in a humidified incubator at 37 °C with 5% CO_2 and 70% relative humidity. A431, HeLa, and HEK293 cells were grown in Dulbecco Modified Eagle Medium (DMEM; Lonza, Walkersville, MD) with 10% Fetal Bovine Serum (FBS) and 1% penicillin and streptomycin. A549 cells were cultured in Ham's F-12K (Kaighn's) Medium (Lonza, Walkersville, MD) with 10% FBS and 1% penicillin and streptomycin. Cells were

passaged with 0.25% trypsin and 0.02% ethylenediaminetetraacetic acid in a Hank's balanced salt solution (Sigma-Aldrich, St Louis, Missouri) when they were approximately 75% confluent. In order to promote cell adhesion, the gold surface of the chips was incubated with 10 μg/mL collagen for 2 h. The collagen-coated chips were rinsed with PBS buffer twice prior to seeding. Each chip was seeded with 5000 cells in 300 μL of growth medium and was incubated for 1 day to allow the cells to attach and grow. The growth medium was replaced with PBS buffer solution prior to the experiment. The viability of cells on the chips was visually inspected prior to the experiment using a tissue culture microscope. A total of more than 50 chips were tested, and all cells showed consistent high viability similar to cells in a tissue culture plate. Cells were fixed by incubating in 4% paraformaldehyde solution for 10 min at room temperature prior to measurement.

Immunofluorescence. The immunofluorescence images were obtained with an inverted fluorescence microscope at 10× magnification (Olympus IX81). A 150 W mercury lamp was used as the light source. For EGFR staining, the fixed cells were incubated with 10 μg/mL anti-EGFR solution for 30 min, followed by 30 min incubation with Alexa Fluor 488 Goat AntiMouse IgG1 (γ1) after three rinses with PBS buffer. The fluorescence image was captured after rinsing the well twice with PBS buffer. The following optical filters were used to obtain the fluorescence image: excitation filter, 420−480 nm, emission filter, 515 nm.

2.3 *In Situ* Quantification of anti-EGFR and EGFR Interaction Kinetics on the Surface of A431 Cell

A431 cell is a model cell line (Epidermoid Carcinoma) that overexpresses EGFR in the cell membrane. To investigate the molecular interaction of EGFR in their native environment, we grew and fixed A431 cells on gold-coated glass coverslips and measured binding kinetics and affinity of anti-EGFR, the specific monoclonal antibody inhibitor targeted at the extracellular domain of EGFR, using a prism based SPRi setup. When anti-EGFR antibody binds to EGFR on the cell membrane, the mass (180 kDa for anti-EGFR) induced refractive index change was recorded as SPR image intensity changes, and presented in the form of SPR sensorgram. Three gold chips with different batches of cells were measured to validate repeatability of the technique. Non-specific binding signals were detected in the cell-free gold area and were subtracted from the original signals of all regions for only specific binding signals. For each measurement, the specific signals of all cells in the SPR images were extracted, and plotted along with the mean value.

Figure 2.10a shows a representative SPR image of A431 cells, in which the bright spots represent individual or clusters of cells. A431 cells tend to aggregate. The following steps were performed to measure the EGFR binding kinetics. First, PBS buffer was flowed over the cells for 300 seconds at a flow rate of 350 µL/min to record the baseline. Next, 2 µg/mL anti-EGFR was introduced to the cells for 350 seconds to record the association process. Last, PBS buffer was reintroduced to the cells for 400 seconds to measure the dissociation of the antibody. During the association process, obvious increases in SPR intensity at all cell regions were observed, as shown in the differential image (Figure 2.10b).

The differential image maps the SPR intensity changes in each pixel by subtracting the original SPR image prior to adding the antibody (t = 300th second) from the SPR image at the end of association phase (t = 650th second). Apart from the obvious intensity increase in all cell regions compared to the gold area, the image intensity changes at different cell regions were different, which indicated the heterogeneity of EGFR express level among individual cells.

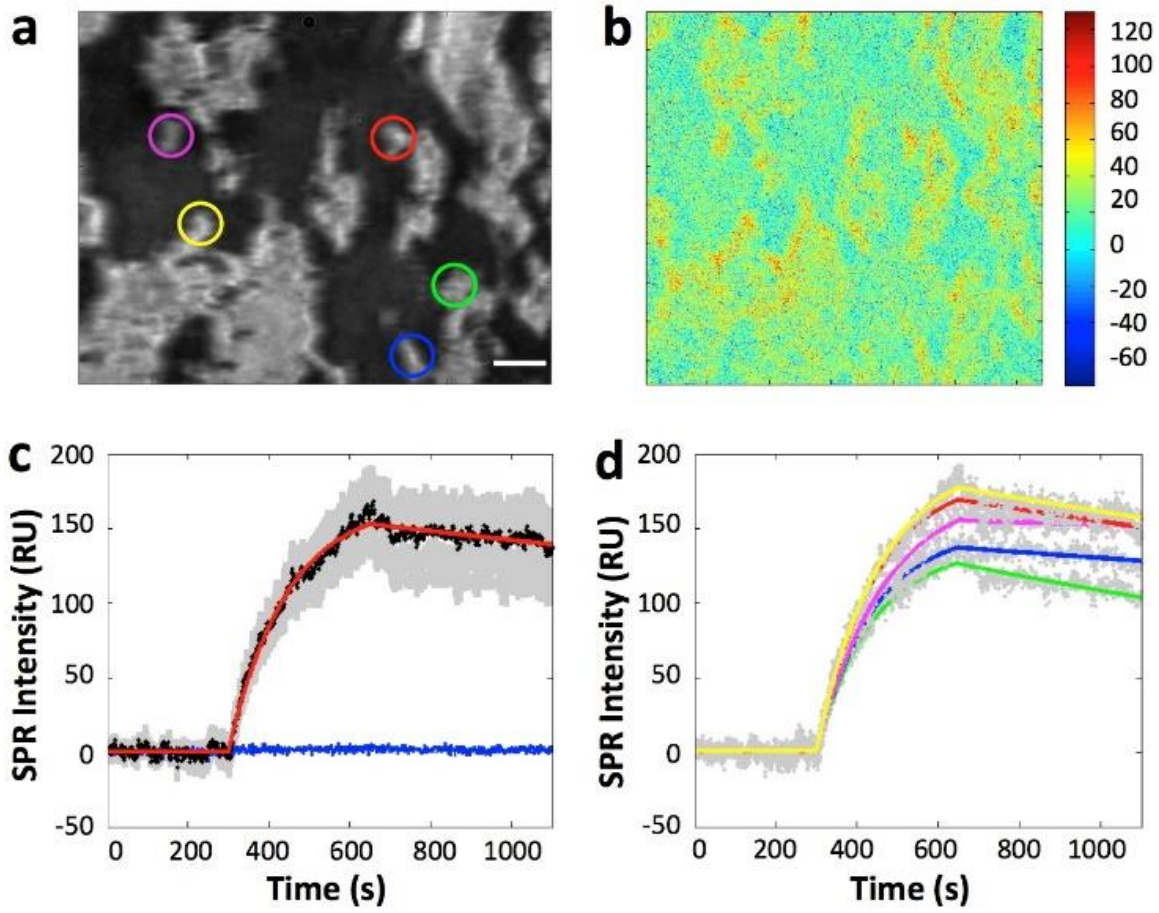

Figure 2.10 SPR responses after antibody binding with the receptor on cell surface. (a) A typical SPR image of a few tens of A431 cells adhered on the gold-coated glass slide. (b) Differential SPR image shows the maximum SPR intensity increase due to anti-EGFR binding to the surface of A431 cells. (c) The average SPR sensorgrams of all cells in view

(black curves: average SPR sensorgram, red curve: curve fitting, gray background: cell-to-cell variation) and the surrounding regions without cell coverage (blue curve). All the curves are abstained by subtracting the non-specific binding response from original signals. (d) The SPR sensorgrams of five individual cells of different regions (gray dotted curves: individual SPR sensorgram, colored curve: corresponding fitting curves). Scale bar, 50 μm.

Quantitative binding kinetics can be extracted from the SPR image sequences and plotted as sensorgrams, with a representative result shown in Figure 2.10c. A maximum averaged increase of 168 RU was found in the SPR sensorgram shown in Figure 2.10c, where the black curve represents the averaged response of all the cells in Figure 2.10a and the gray background area shows the response from individual cells or clusters. The binding kinetics of anti-EGFR in A431 cells were determined by fitting the averaged response curve with a 1:1 Langmuir binding model (the red curve). From three independent measurements, the corresponding association rate constant (ka), dissociation rate constant (kd) and dissociation constant (K_D) were calculated and showed in Table 2.1 as the mean value of three chips. These results validated the repeatability of the measurements, and indicated a fast and strong binding. The flat blue curve in Figure 2.10c shows that there is no response from the gold area without cells, and confirms the specificity of the antibody binding.

2.3.1 Heterogeneous Binding Kinetics of Individual Cells

An important capability of imaging based measurement is to quantify the heterogeneous responses of anti-EGFR interaction from individual cells, which is important for identifying tumor specificity therapy development, since tumor tissue sample

often mixed with normal cells. Figure 2.10d shows the association and dissociation processes of five individual cells selected from different regions of the chip, where the color curves are first order kinetic fitting to the data (gray dots). The corresponding cells are marked with corresponding colored circles in Figure 2.10a. From the sensorgrams, we can conclude that maximum association varies from cell to cell. Furthermore, the kinetic constants (Table 2.1) obtained from the fitting exhibit up to seven folds of variations, significantly larger than the measurement error. The measurement error (variation from different tests) was obtained by repeating the same tests for three times, and the standard deviation of kinetic constants was within 10%. These results reveal cell-to-cell heterogeneity in the binding of drugs to the cells, which underscores the importance of measuring binding kinetics at single cell level.

Table 2.1 Measured EGFR binding kinetic constants

	k_a ($M^{-1}s^{-1}$)	k_d (s^{-1})	K_D (nM)
Cell 1 (red curve)	6.0×10^{5}	2.6×10^{-4}	0.43
Cell 2 (blue curve)	6.4×10^{5}	1.5×10^{-4}	0.23
Cell 3 (green curve)	6.2×10^{5}	2.4×10^{-4}	0.70
Cell 4 (yellow curve)	5.5×10^{5}	2.7×10^{-4}	0.49
Cell 5 (purple curve)	5.3×10^{5}	5.5×10^{-5}	0.10
Mean value of 3 chips	6.7×10^{5}	3.3×10^{-4}	0.41

2.3.2 Dose Response, Global, and Equilibrium Fitting

To measure the dose response of EGFR to the antibody drug, anti-EGFR solutions with concentration increasing from 0.5 to 10 μg/mL were sequentially introduced to A431

cells on a sensor chip to record the association and dissociation kinetics. For each new dose of anti-EGFR, the cell surface was regenerated with 100 mM NaOH for 30 seconds. SPR sensorgrams for different doses of anti-EGFR were plotted in Figure 2.11a (black curves). Both the association rate constant and maximum SPR response increase with anti-EGFR concentration, which are expected for first order kinetics. The red lines are the global fitting results of the sensorgrams based on 1:1 binding kinetics model. The kinetic constants obtained from the global fitting are $k_a = (2.7 \pm 0.6) \times 10^5\ M^{-1}s^{-1}$, kd = $(1.4 \pm 0.5) \times 10^{-4}\ s^{-1}$, and $K_D = 0.53 \pm 0.26$ nM, and are consistent with the individual fitting result.

In addition to the kinetic analysis, equilibrium-fitting curve was plotted based on the equilibrium binding responses obtained at seven different concentrations (Figure 2.11b), and the obtained dissociation constant, K_D, was determined to be 5.1 nM, in the range of reported value.[82] K_D value obtained from the equilibrium-fitting curve is depending on the ligand (anti-EGFR) concentration. In general, K_D value will increase as the concentration of the ligand increases,[83] which may account for the difference between the global fitting result and equilibrium fitting result. As the concentrations of anti-EGFR used in our experiments are all bigger than the dissociation constant calculated in global fitting, it is reasonable that the K_D obtained from the equilibrium-fitting curve is larger than the K_D obtained from kinetic response curves.

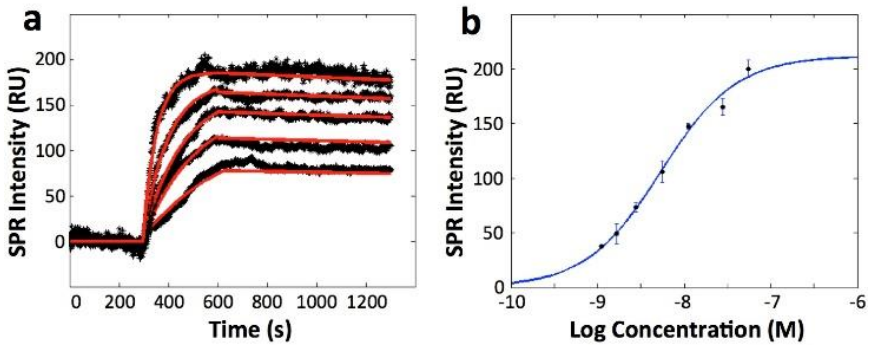

Figure 2.11 The SPR sensorgrams of different concentrations. (a) SPR sensorgrams of a cell at different concentrations of anti-EGFR and the corresponding global fitting (red curves). Anti-EGFR concentrations are 0.5, 1, 2, 5 and 10 μg/mL from bottom to top curve, respectively. (b) The equilibrium-fitting curve. The anti-EGFR concentration (plotted in log scale) was 0.2, 0.3, 0.5, 1, 2, 5 and 10 μg/mL, respectively. The equilibrium response values at different concentrations are obtained by fitting association section of sensorgrams with first order kinetics. At least 3 independent measurements were performed for each concentration.

2.3.3 EGFR Binding Kinetics and Expression Levels in Different Cell Lines

In addition to determination of binding kinetics, the SPR signal can also be used to quantify the expression level of EGFR in A431 cell membrane. In SPR sensorgram, the equilibrium response represented the saturated amount of anti-EGFR bound to A431 cells, from which we can estimate EGFR receptor density by assuming the 1:1 binding between anti-EGFR and EGFR on cell surface. With 10 μg/mL anti-EGFR stimulation, the equilibrium response was calculated to be 190 RU increase in SPR intensity, which can be used for receptor density calculation. Assume 1 RU SPR response corresponds to 1 pg/mm^2 mass application, the binding of anti-EGFR induced 190 pg/ mm^2 in the cell surface, which

corresponds to ~636 receptors/μm^2. Given the average diameter of 25 μm for suspended A431 cells, the average number of EGFR receptors is around 5×10^5 per cell. This number is consistent with the results measured by flow cytometry and fluorescent labeling.[84] This result shows that cell-based SPRi is able to quantify membrane receptor density without any labeling, and is a potentially a valuable tool for biomarker discovery and cancer diagnosis.

To investigate how the native cellular microenvironment affects the drug-receptor interactions, binding kinetics of anti-EGFR to EGFR in four cell lines with different expression levels were studied. These cell lines include EGFR-positive A431, Hela and A549, and EGFR-negative HEK293 as a negative control. Figure 2.12a shows the SPR images of different cell lines before the antibody administration. Differential SPR images in Figure 2.12b shows the SPR intensity increase due to anti-EGFR binding. Obvious increase was observed in A431 cells, while Hela cell and A549 cells showed much smaller responses. Figure 2.12c shows the averaged responses curves of a few tens of cells (black lines) and the kinetic fitting curves (red lines). The gray area represents the distribution, which measures the heterogeneity for each cell line. Typical association and dissociation curves observed in Hela and A549 cell with reduced responses compare with A431. No response from EGFR-negative HEK293 cells was observed, confirming that the specific anti-EGFR and EGFR interactions were responsible for the SPR responses in cell regions. From the equilibrium binding responses, EGFR density in Hela and A549 were found to be 270 and 142 receptors/μm^2, respectively, corresponding to 0.21 and 0.11 million per cell, much lower than A431.

For cross validation, the EGFR expression levels in different cell lines were confirmed by immunofluorescence imaging. Figure 2.12d shows the fluorescence image of the four cell lines stained with anti-EGFR antibody followed by a fluorescence-labeled secondary antibody. The intensity of fluorescent signal is proportional to the EGFR abundance. In consistence with SPRi results, A431 cell has the highest fluorescence intensity, while Hela and A549 cells exhibit lower emission, and HEK293, the negative control, shows no detectable fluorescent signal.

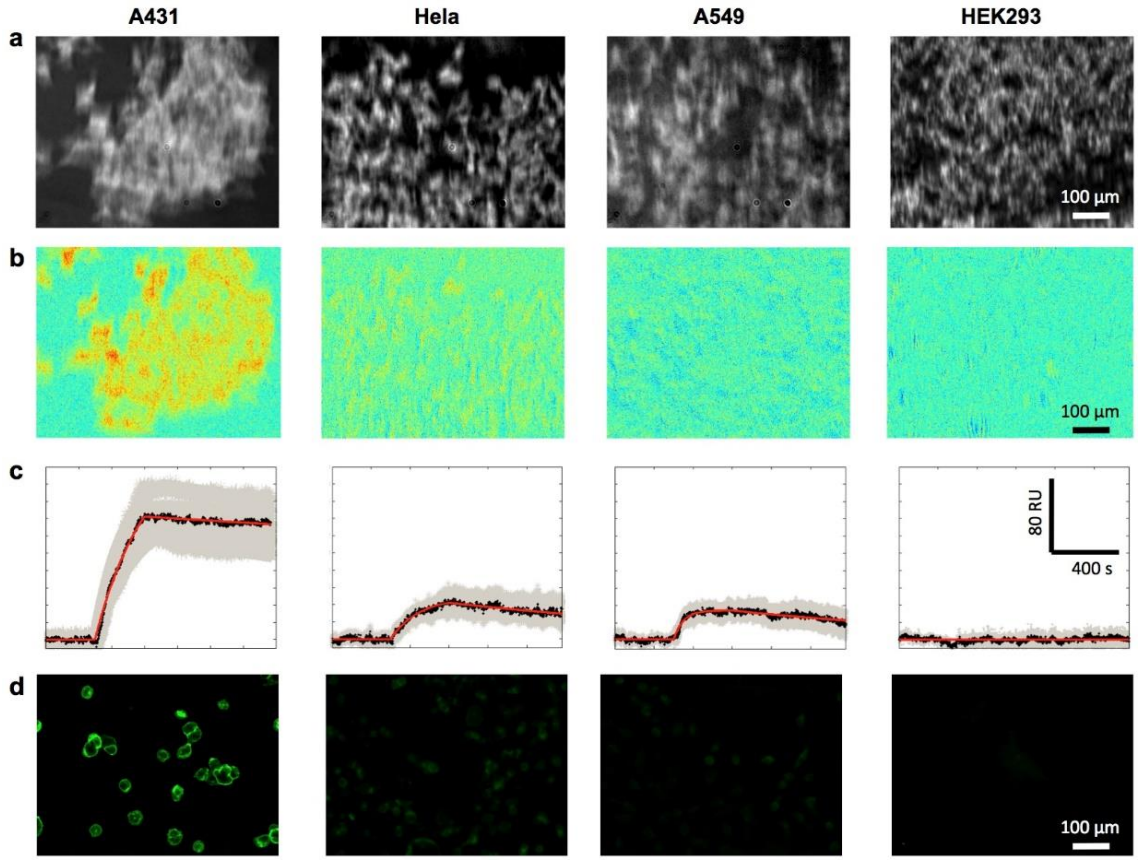

Figure 2.12 Anti-EGFR interactions with EGFR-positive (A431, Hela and A549) and EGFR-negative (HEK 293) cell lines. (a) SPR images before anti-EGFR binding. (b) Differential SPR images after anti-EGFR binding. (c) The SPR sensorgrams of 2 µg/mL

anti-EGFR binding. All the curves are abstained by subtracting the non-specific binding response from original signals. (d) Immunofluorescence images by staining EGFR.

The kinetic constants in the three EGFR-positive cell lines were determined from fitting the averaged cell responses with first order kinetics. Table lists the EGFR density and binding kinetics of the three cell lines we measured. The table shows a trend of increased rate constants (ka and kd) and stronger affinity (lower K_D) with lower receptor density, which could be caused by steric hindrance effect. This observation show that the membrane microenvironment of the EGFR receptors may plays an important role in drug/receptor interactions, and this information could not be obtained by traditional approaches that study proteins isolated from the cells.

Table 2.2 EGFR densities and binding kinetic constants with anti-EGFR in different cell lines

Cell line	**EGFR density (Molecules/μm^2)**	**k_a ($M^{-1}s^{-1}$)**	**k_d (s^{-1})**	**K_D (nM)**
A431	636	2.7×10^5	1.4×10^{-4}	0.53
Hela	270	5.4×10^5	2.4×10^{-4}	0.45
A549	142	2.4×10^6	7.0×10^{-4}	0.29

2.4 Conclusions

In this chapter, we have quantified the binding kinetics of the monoclonal anti-EGFR antibody to its membrane bound target receptor EGFR in cultured cells with SPRi. The imaging capability of this label free method enables the mapping of individual cell responses. The real time detection capability provides quantitative information on the

membrane bound receptor density and ligand interaction kinetics. While the averaged kinetic constants are consistent with the literature data, we have observed several fold cell-to-cell variations in kinetic constants. Furthermore, we found a correlation between EGFR density and binding kinetics among different EGFR positive cell lines. Our results demonstrated that SPRi is able to directly quantify the membrane bound receptor expression level and ligand binding kinetics without the need of labeling. Our findings also underscore the importance of an *in situ* study of drug/receptor interaction in intact cells.

CHAPTER 3 QUANTIFICATION OF SMALL MOLECULE INTERACTION WITH MEMBRANE PROTEINS WITH MECHANICAL AMPLIFICATION METHOD

3.1 Introduction

We have demonstrated that SPRi technique can be used for the binding of antibody with membrane protein on cell surface, which greatly simplifies the sample preparation process for protein purification. However, the limitation of this SPRi is also obvious. As the SPR signal in molecular binding is mostly generated by the mass changes on the gold surface, only big molecules (>10 kDa) can be detected. Thus SPRi is not a suitable detection method for small molecules, which are the most popular drugs. Therefore, a new platform for small molecules binding detection on cell surface is of great importance.

Despite the importance, quantifying the binding kinetics of small molecules with membrane proteins on whole cells has been a difficult task. A common approach to study molecular interactions is to use radioactive [85-88] or fluorescent labels.[89-93] The latter includes total internal reflection fluorescence (TIRF) microscopy [94, 95] and super-resolution microscopy.[96, 97] TIRF is limited to imaging of the bottom of cells only because the evanescent wave penetration length is ~200 nm from the surface on which the cells are attached. Super-resolution microscopy takes several minutes to acquire one image frame, making it difficult to track binding kinetics in real time. To determine the kinetics, the current mainstream practice is to isolate membrane proteins from the cell membranes and measure the binding with a label-free detection technology, such as surface plasmon resonance (SPR), quartz crystal microbalance (QCM) and Bio-layer interferometry.[34,

98-102] The isolation procedure involves extraction of membrane proteins from cells, purification and immobilization of them on a sensing surface, which is laborious, and often difficult because of the low solubility and low expression levels of many membrane proteins. Furthermore, the isolated membrane proteins may lose their native structures and functions outside the lipid environment. Studying membrane proteins in the native cellular membranes is thus important.[42, 103, 104] A significant advance is the study of membrane proteins on the surfaces of unilamellar vesicles with a backscattering interferometry technology.[105] The technology is still an endpoint assay.

All the above label-free technologies are mass based detection, and their signals diminish with the molecular weight, making them difficult to measure small molecule binding to proteins. Small molecules account for more than 90% FDA approved drugs, and play essential roles in various cellular functions. We have recently shown that molecular binding to a cell adhered on a surface causes it to deform.[103] However, the molecular binding-induced cellular deformation is sensitive to the detail of the cell-surface adhesion, and varies from one region of the cell to another, which complicates the interpretation of the data.

In this chapter, we report a method to trap single cells onto an array of micro-holes with a microfluidic device, and measure the molecular binding to membrane proteins by tracking the cellular mechanical deformation with sub-nm precision using an optical imaging system[106]. This label-free method offers a capability of measuring both large and small molecule binding to membrane proteins on single cells in real time. We demonstrate this capability by measuring the binding kinetics of major types of

transmembrane proteins, including glycoproteins, ion channels, G-protein coupled receptors (GPCRs) and tyrosine kinase receptors on single whole cells. We establish the basic principle of the method by developing a model to express the binding-induced nanometer-scale cellular deformation in terms of molecular interactions, and cellular mechanical properties, and carrying out experiments to validate the model.

3.2 Materials and Methods

Materials. Wheat germ agglutinin (WGA), acetylcholine chloride, AMD3100 octahydrochloride hydrate, SDF-1 α and insulin molecules were purchased from Sigma-Aldrich (St. Louis, MO). Anti-EGFR monoclonal antibody was purchased from EMD Millipore (Billerica, MA). Pertussis Toxin was purchased from List Biological Labs. All solutions used in the experiments were prepared with 1X PBS. All reagents were analytical grade from Sigma-Aldrich, except those stated.

Cell Culture. SH-EP1, SH-EP1_ α4β2, A549, Hep G2, A431, HeLa and HEK293 cell lines were obtained from the American Type Culture Collection (Rockville, MD). All the cells were cultured in a humidified incubator at 37°C with 5% CO_2 and 70% relative humidity. SH-EP1, SH-EP1_ α4β2, Hep G2, A431, HeLa and HEK293 cells were grown in Dulbecco Modified Eagle Medium (DMEM) (Invitrogen, Carlsbad, California) with 10% Fetal Bovine Serum (FBS) and 1% penicillin and streptomycin. A549 cells were cultured in F-12K with 10% FBS and 1% penicillin and streptomycin. Cells were passaged with 0.25% trypsin and 0.02% ethylenediaminetetraacetic acid in Hank's balanced salt solution (Sigma-Aldrich, St Louis, Missouri) when they were approximately 75% confluent.

Before experiments, suspension cells in 1X PBS buffer solution were prepared. First, the cells were trypsinized from the flask to round up, and centrifuged for 5 mins to discard the old medium. Then, the centrifuged cell piles were suspended in 4% paraformaldehyde solution for 10 mins fixation. Finally, the fixed floating cells were centrifuged again to discard the fixatives and transferred to the 1X PBS. Overnight recovery was performed after cell fixation to improve cell elasticity and deformability.

For living cell binding kinetic measurements, the cells were also trypsinized from the flask and centrifuged for 5 min to discard the old medium. Then, the centrifuged cells were suspended in live cell imaging solution (Life Technologies) and immediately used for kinetic measurements to maintain cell viability.

Optical Imaging. An inverted microscope (Olympus IX-81) equipped with a top illuminating white light, a phase contrast condenser and 40x phase contrast objective was used as the imaging device. The trapped cells within the microfluidic plate were imaged from bottom with a CCD camera (AVT Pike F032B) at a frame rate of 7 frames per second (fps). The spatial resolution of the system was ~0.5 μm.

Microfluidic Device for Cell Trapping and Binding Kinetics Measurement. As shown in Figure 3.1, we used a homemade and modified commerical (AX150, AXIS™ Axon Isolation Device from Millipore) PDMS-microfluidic device to trap single cells. The fabrication used the standard soft lithography. The homemade microfluidic plate had two parallel channels (10.6 mm long, 1500 μm wide and 40 μm high), separated with a barrier. The barrier had 60 holes (each hole is 150 μm long, 10 μm wide, separation between two holes is 50 μm) to trap cells. Sample solution containing suspended cells was flowed in one

channel while keeping a lower pressure in the second channel. This allowed trapping of one cell in each hole for binding kinetics measurement (~5 mins). The optics allowed imaging of two cells simultaneously. When one measurement was completed, the cells were released from the trapping holes, and new cells were trapped for repeated measurement. The sample and buffer flows were controlled with a drug perfusion system (SF-77B, Warner Instruments, Connecticut). The typical transition time between different solutions was about 1-2 seconds.

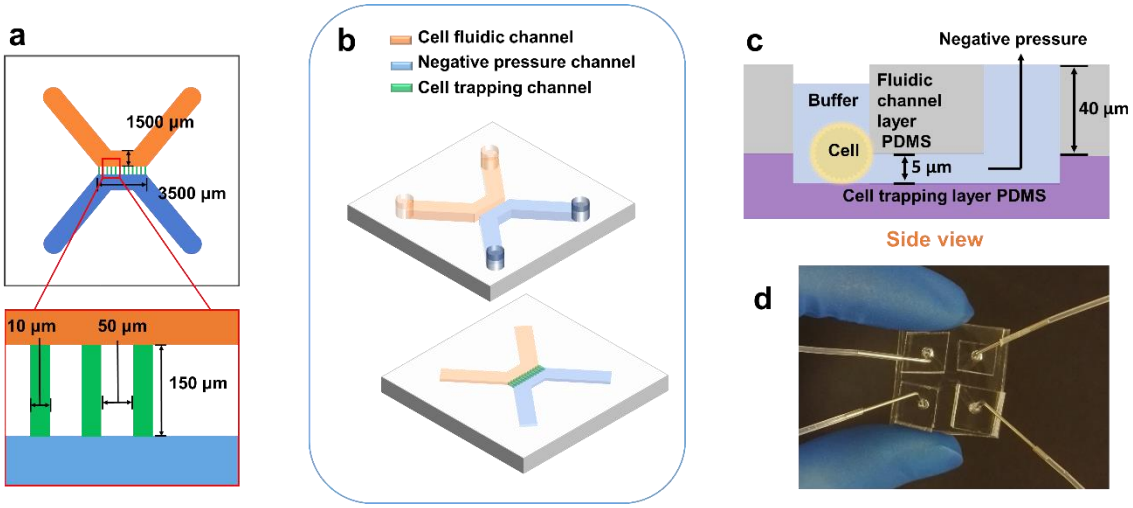

Figure 3.1 Microfluidic chip for single cell trapping. (a) Schematic illustration of the microfluidic chip showing two parallel fluidic channels (orange and blue). (b) Top and bottom layers of the microfluidic chip. (c) Side view of the microfluidic chip showing trapping of a cell via the micro-holes on the wall that separates the two parallel fluidic channels. (d) Photo of the microfluidic chip together with tubing connected to the inlets and outlets.

3.3 Detection Principle

3.3.1 Thermodynamic model

Thermodynamics predicts that molecular binding to a surface changes the surface tension. This phenomenon was manifested in microcantilever biosensors, where molecular binding to a microcantilever causes it to bend, and the amount of bending increases with decreasing thickness of the microcantilever.[107] Cell membranes are a few nanometers thick, much thinner than typical microcantilevers (a few microns), so we expect to observe cell membrane deformation upon molecular binding to the membrane proteins on a cell surface. By tracking the membrane deformation in real time, we can thus quantify the kinetics of molecular binding taking place on the surface of a trapped cell as shown in Figure 3.2. The free energy of the cell surface can be expressed as [108, 109]

$$F = \frac{1}{2}\kappa(2H - C_0)^2 A + \gamma A + k_B T f(\phi) A - \Lambda_1 H \phi A - \Lambda_2 H(1-\phi)A, \qquad (3.1)$$

where the first term is bending energy (κ is the bending modulus, H is the mean membrane curvature, C_0 is the spontaneous curvature), the second term is surface tension (γ), the third term is the entropic contribution from the membrane proteins (k_B is the Boltzmann constant and T is temperature, and $f(\phi)$ is a dimensionless parameter that depends on concentrations of the membrane proteins with and without bound ligand molecules), the fourth and fifth terms describe the interactions of the membrane proteins (with and without bound ligand molecules) with the lipid bilayer (Λ_1 and Λ_2 are the interaction strengths between the lipids and the membrane proteins with and without bound ligand molecules, respectively, and ϕ is the fraction of the membrane proteins with bound ligand molecules). If assuming ideal mixing, $f(\phi)$ can be expressed as

$$f(\phi) = \ln[\phi(1-\phi)]. \quad (3.2)$$

By minimizing the free energy given by Eq. 3.1, we have

$$2\kappa(2H - C_0)\delta H A + \frac{1}{2}\kappa(2H - C_0)^2\delta A + \gamma\delta A + k_B T \ln[\phi(1-\phi)]\,\delta A +$$

$$k_B T \frac{1-2\phi}{\phi(1-\phi)}\delta\phi A - \Lambda_1\delta H\phi A - \Lambda_1 H\delta\phi A - \Lambda_1 H\phi\delta A - \Lambda_2\delta H(1-\phi)A + \Lambda_2 H\delta\phi A -$$

$$\Lambda_2 H(1-\phi)\delta A = 0, \quad (3.3)$$

If we assume spherical cells, $A = \frac{4\pi}{H^2}$, and Eq.3.3 can be simplified as

$$\frac{\Delta D}{D} = -\frac{1}{2}\frac{(\Lambda_2 - \Lambda_1)H + k_B T\frac{1-2\phi}{\phi(1-\phi)}}{\frac{\kappa}{2}(2H - C_0)(-C_0) + \gamma + k_B T \ln[\phi(1-\phi)] - \frac{1}{2}\Lambda_1 H\phi - \frac{1}{2}\Lambda_2 H(1-\phi)}\Delta\phi, \quad (3.4)$$

If the interaction energy between the membrane proteins and lipids is much greater than the thermal energy, $k_B T$, and the binding induced membrane deformation is relatively small, Eq. 3.4 can be simplified as,

$$\frac{\Delta D}{D} = \frac{(\Lambda_2 - \Lambda_1)H}{\kappa(2H - C_0)C_0 - 2\gamma}\Delta\phi. \quad (3.5)$$

where Λ_1 and Λ_2 are the interaction strengths between the membrane lipids and the membrane proteins (receptors) with and without bound molecules (ligands), respectively, H is the mean curvature, κ is the bending modulus, C_0 is the spontaneous curvature of the cell, γ is the surface tension, and ϕ is the fraction of the receptors with bound ligands. Eq. 3.5 shows that the molecular binding induced membrane deformation is proportional to the number of ligands bound to the receptors.[110-112] According to this model, the membrane deformation depends on the nature of ligand-receptor interactions, but it is not directly related to the masses of the ligands. So the present method works for both large and small molecule ligands, as long as the binding changes the interactions of the receptors with the membrane.

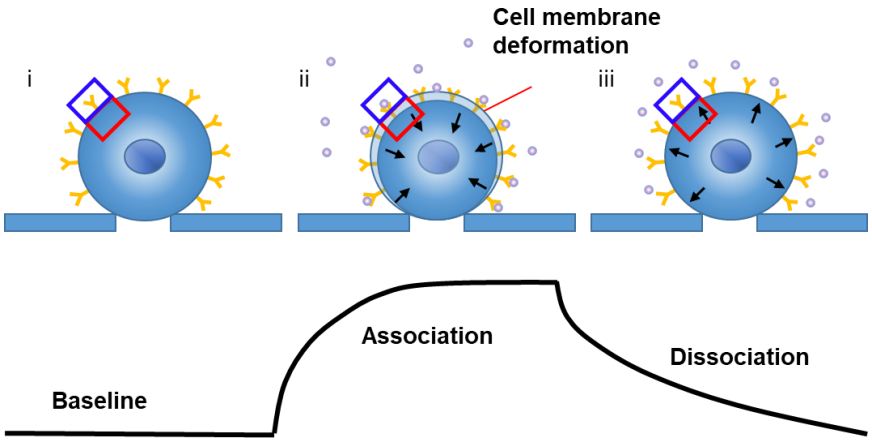

Figure 3.2 Schematic of the principle for measuring binding kinetics from the cell deformation. Cell edge positions before binding (i), during binding (association) (ii), and during dissociation (iii), where the blue and red boxes indicate a region of interest (ROI) used in a differential optical tracking algorithm of the cell deformation.

3.3.2 Microfluidic Device

We used a microfluidic chip consisting of two parallel fluidic channels separated with a thin wall with micro-holes (diameter of 10 μm) to trap single cells for measurement. Channel 1 had an inlet and outlet to allow sample and buffer solutions to flow in and out, and channel 2 had a lower pressure than channel 1 (Figure 3.3a). We flew cells along channel 1 while maintaining a lower pressure in channel 2, which resulted in trapping of the cells onto the individual micro-holes (Figure 3.3b).[113] We then introduced ligands from channel 1, and studied binding of the ligands to the membrane protein receptors on each of the trapped cells by measuring the binding-induced mechanical deformation of the cell as stated in Eq. 3.5.

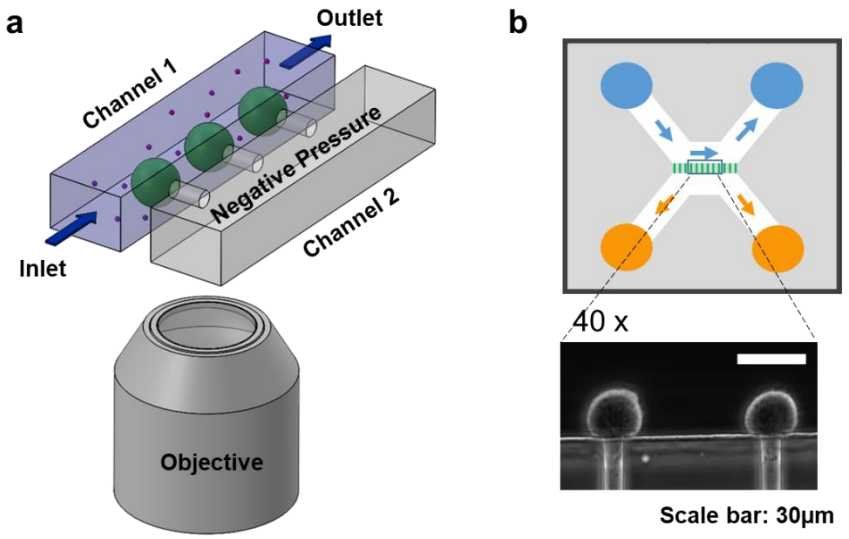

Figure 3.3 Setup for measuring binding of small and large molecules to membrane proteins on trapped cells. (a) Schematic illustration of the experimental setup consisting of a microfluidic system for trapping single cells onto micro-holes, and for introducing ligand molecules at different concentrations for binding kinetics measurement, and an optical imaging and signal processing system for tracking the cell deformation associated with the binding in real time. (b) Flow design of the cell trapping microfluidic chip and optical images of trapped cells with 40x phase contrast objectives.

3.3.3 Differential Optical Tracking Method

To measure the small molecule binding induced cell deformation, we used a differential optical tracking method (Figure 3.4). First, we imaged the trapped cells with phase contrast microscopy, which clearly revealed the edge of each cell. We then selected a rectangular region of interest (ROI) such that the cell edge passed through the center of the ROI, and then divided the ROI into two equal halves, one was inside the cell (red), and the other half fell outside of the cell (blue, Figure 3.5). When the cell deformed, the image

intensity in one half increased, and the other half decreased. The differential image intensity of the two halves was defined as, $(I_1-I_2)/(I_1+I_2)$, where I_1 and I_2 are the intensities of the first and second halves, respectively, which was proportional to cell deformation. We calibrated this differential deformation-tracking algorithm by shifting the ROIs over different numbers of pixels in the direction normal to the cell edge (Figure 3.5d). The differential image intensity was linearly proportional to the cell deformation within a certain range (Figure 3.5e and f).

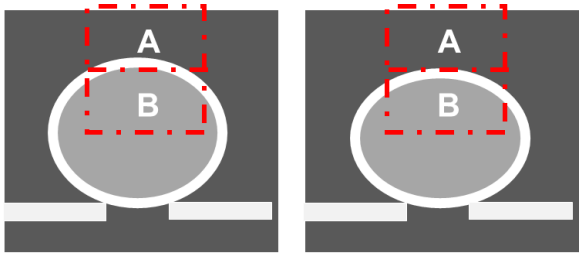

$$d = \alpha \frac{I_A - I_B}{I_A + I_B}$$

Figure 3.4 Schematic illustration of the differential optical detection method. The membrane deformation is related with the differential intensity of ROI A and ROI B with a calibration factor of α.

The detailed tracking procedure of the differential optical detection method is illustrated in Figure 3.5. First, the edge of the cell was manually chosen, and the center of the cell was determined (Figure 3.5a). Then, the calibration curve at each location along the cell edge was obtained by shifting the ROI (1.11 × 2.22 μm) from outside to inside of the cell, in the direction perpendicular to the cell edge (Figure 3.5d, e and f). Using the calibration curves, the cell deformation (edge movement) at each point along the cell edge was determined, and the cell deformation averaged over the entire cell was used to

determine the molecular binding kinetics. Depending on the cell lines, both contraction and expansion were observed, but the binding kinetics was determined from the absolute values of the cell deformation vs. time.

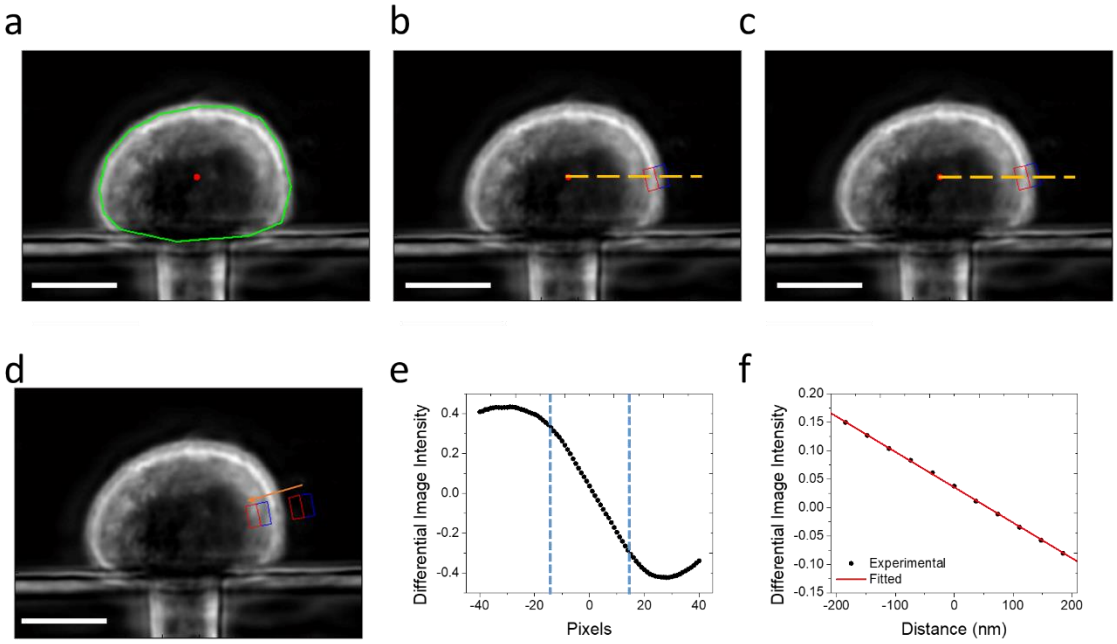

Figure 3.5 Calibration of the optical tracking of cellular deformation. (a) The edge (green line) and the centroid (red dot) of the cell were determined with an imaging-processing algorithm. (b) and (c) A region of interest (ROI) (1.11 μm by 2.22 μm) was selected to include the edge, and the ROI was rotated at every 1 degree along the cell edge, where the angle was defined by a radial line (from the cell centroid to the cell edge). (d) The optical tracking method was calibrated by shifting the ROI by different numbers of pixels from outside to inside of the cell in the direction perpendicular to the tangential line at the cell edge. (e) Differential image intensity vs. cell edge position (d), where the two vertical dashed lines mark a linear region used in the differential optical tracking algorithm. (f) A

typical calibration curve to determine the cell deformation from the differential image intensity. Scale bar: 10 μm.

The differential optical detection method subtracted the common noise (e.g., light intensity and mechanical perturbation) in the optical system, thus providing precise tracking of subtle cell deformation associated with the molecular binding. The standard deviation of the cell deformation averaged over a cell was as small as ~0.4 nm (Figure 3.6b). To further analyze the noise source, we tracked the edge movement of a fixed object created with a marker (inset of Figure 3.6a) with the same optical system and differential tracking algorithm, where the noise was purely due to the optical system, including light source and camera. The noise level was ~0.1 nm, several times smaller than the noise observed for cells (Figure 3.6). This observation suggests that the cell edge detection limit of the present system was mainly determined by the intrinsic mechanical instability of the cells.

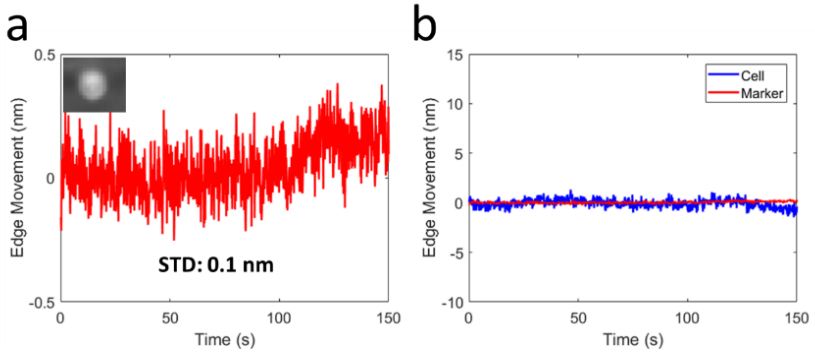

Figure 3.6 Noise Analysis. (a) Noise in the position (edge movement) of a fixed object (marker dot). (b) Comparison of noises in the edge movements of a cell and the marker dot.

3.4 Label Free Detection of Small Molecules Interaction with Membrane Proteins

3.4.1 Binding Kinetics of Four Major Types of Cell Surface Membrane Proteins

To measure the molecular interaction with membrane protein, we transfected the targeted membrane proteins in cell lines, cultured and then harvested them as cell suspensions, followed by briefly fixing and re-suspending the cells in 1X PBS buffer. We injected the cell suspension of each membrane protein into channel 1 of the microfluidic chip, trapped the individual cells onto the micro-holes by applying a small negative pressure. For the binding process measurement, the PBS buffer was first injected to obtain baseline. Then the drug molecules were added to measure the association process, during which the cell deformed. Last, the solution was switch back to PBS buffer, and the dissociation process was measured, during which the cell recovered back. By tracking the edge movement averaged over the entire cell with the differential tracking algorithm, the binding kinetic curved was plotted as shown in Figure 3.7.

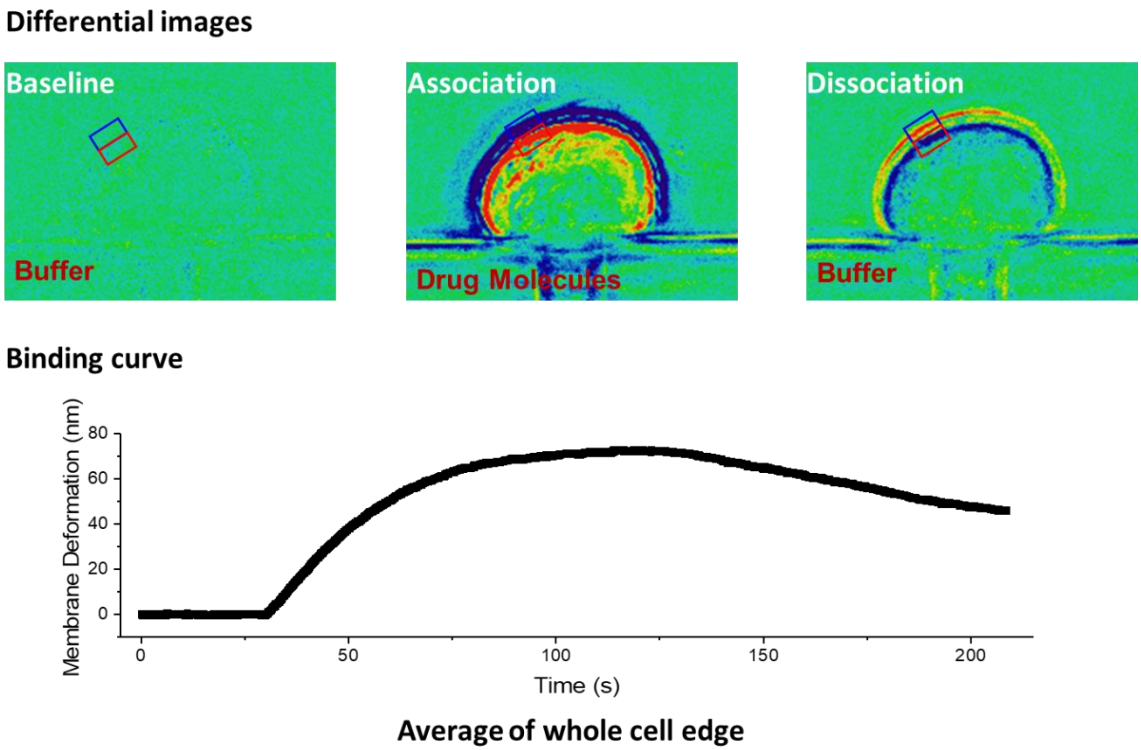

Figure 3.7 Cell membrane deformation during molecular interaction. The differential images is the cell membrane deformation during WGA binding with glycoprotein in SH-EP1 cells. Cell shows very little change in baseline. Cell contracted during association process and recover back during dissociation process. The binding kinetic curve is extracted with the differential tracking algorithm.

To demonstrate the capability of the method, we studied different transmembrane proteins, glycoproteins, ion channel proteins, G-protein coupled receptors (GPCRs) and tyrosine kinase receptors, each representing a major membrane protein type. These membrane proteins are involved in most of the cellular signaling pathways,[114, 115] and determining the binding kinetics of ligand molecules with them are important for cell biology research, biomarker discovery and drug development.

Glycoprotein: Glycoproteins are critical for cell recognition and communication,[4, 116] and lectins are carbohydrate-binding proteins that recognize and bind to the specific sugar groups of glycoproteins on cell surfaces for regulation of cell adhesion and synthesis of glycoproteins. We studied wheat germ agglutinin (WGA; molecular weight, 35 kDa), a lectin that recognizes N-acetylglucosamine (GlcNAc) and sialic acid groups on the surface of brain neuroblastoma SH-EP1 cells. First, 1X PBS buffer was injected in channel to flow over the trapped cells (Figure 3.8a, inset) with a flow rate of 300 μL/min for 50 s to obtain a baseline. Then, WGA (in 1X PBS buffer) solution was introduced for 100 s to allow the binding (association) of WGA with the glycoproteins on the cells. After the association process, the flow was switched back to 1X PBS buffer for another 100 s to allow dissociation of WGA from the cells. The entire procedure was repeated for three times with different WGA concentrations, starting from low to high concentrations (70, 140 and 280 nM). The cell contracted gradually during the association process, and expanded back during the dissociation process. By tracking cell deformation vs. time, we obtained binding curves, shown in Figure 3.8a (black curves), presenting up to 225 nm cellular deformation. Both the rate of association and the amount of cell deformation increased with WGA concentration, which is expected for first order kinetics. By globally fitting the binding curves obtained at different concentrations with a 1:1 binding kinetics model, the association rate constant (k_{on}), dissociation rate constant (k_{off}), and dissociation constant (K_D) were found to be $k_{on} = 1.8 \pm 0.02 \times 10^5\ M^{-1}s^{-1}$, $k_{off} = 5.6 \pm 0.01 \times 10^{-3}\ s^{-1}$ and $K_D = 31 \pm 0.5$ nM. These results are consistent with those obtained with SPR imaging method.[42]

Ion channel protein: Ion channels are membrane proteins that establish electrical signals (action potentials) in cells, and mediate communication across the synapses in nerve systems. We studied here nicotinic acetylcholine receptor (nAChR), an ion channel protein that plays a critical role in neurotransmission and drug addiction, and measured its binding to acetylcholine, a neurotransmitter. The neurotransmitter has a small mass (182 Da), which is difficult to study with traditional label-free detection methods. We transfected brain neuroblastoma SH-EP1 cells with human α4β2 receptor (SH-EP1- α4β2) for binding kinetics measurement (Figure 3.8b). The estimated expression level of the receptor is ~110 nAChRs/μm^2 (~0.8 million per cell).[117] Following a similar procedure as described above for the glycoproteins, we measured the binding of acetylcholine at different concentrations to nAChR (Figure 3.8b) and obtained obvious membrane deformation signals and the maximum deformation was around 70 nm. The red lines are the global fitting to the binding curves (black) using the 1:1 binding kinetics model. The association (k_{on}) and dissociation (k_{off}) rate constants were found to be $2.9 \pm 0.01 \times 10^4\ M^{-1}s^{-1}$ and $2.0 \pm 0.02 \times 10^{-3}\ s^{-1}$, respectively, from which the dissociation constant (K_D) was determined to be 69 ± 0.4 nM. Both the kinetic rate and equilibrium constants are consistent with those reported for adherent cells.[103]

G-protein coupled receptor: GPCRs are a major type of drug targets,[118] accounting for 25% of all current drugs. We studied C-X-C chemokine receptor type 4 (CXCR-4), a common GPCR broadly expressed in central nervous and immune cells. CXCR-4 is responsible for leukocyte trafficking, human immunodeficiency virus type 1 (HIV-1) infection and the proliferation and metastasis of various carcinomas.[119] To

inhibit the activation of CXCR-4 in cancer treatment, various antagonists are used to block the binding pocket of the receptor, among which AMD3100 (Plerixafor, a small molecule drug, 794 Da) has been approved for clinic use.[120, 121] Quantification of binding kinetics between CXCR-4 and the antagonist is essential to evaluate the therapeutic effect. We measured the binding of AMD3100 to CXCR-4 on the surface of human lung carcinoma cells (A549). The A549 cells (Figure 3.8c, inset) are smaller and more rigid than the SH-EP1 cells (Figure 3.8b, inset), and the binding induced membrane deformation was smaller with a maximum value of 46 nm. We obtained the binding curves for CXCR-4 at different AMD3100 concentrations (black curves), and performed global fitting of the binding curves (red curves) with the first order binding kinetics model and obtained, k_{on} = $3.8 \pm 0.05 \times 10^3\ M^{-1}s^{-1}$, k_{off} = $7.7 \pm 0.07 \times 10^{-4}\ s^{-1}$ and K_D = 0.2 ± 0.003 μM. The affinity constant is in good consistence with the literature value (0.1 μM) measured by the radioligand assay.[122]

Tyrosine kinases Receptor: Kinases are enzyme-linked receptors, which are responsible for the regulation of normal cells and also for the initiation and progression of various types of cancers.[123] An important example is insulin receptor that binds with insulin, which is a critical step in regulating glucose homeostasis, a functional process that is directly relevant to diabetes and cancer. Determining the binding between insulin and the receptor is thus needed for understanding type 2 diabetes, and discovering related drugs. Studying the binding interaction to the insulin receptor with the existing technologies has been a challenge because of its low expression levels and difficulty in purification. We measured the binding kinetics of insulin with insulin receptor on the surface of human liver

cancer cells (Hep G2) (black curves, Figure 3.8d) and performed global fitting of the data (red curves) with binding kinetic constants of $k_{on} = 7.5 \pm 0.20 \times 10^3\ M^{-1}s^{-1}$, $k_{off} = 2.5 \pm 0.04 \times 10^{-4}\ s^{-1}$ and $K_D = 33 \pm 0.8$ nM. The binding induced deformation is smaller but detectable, presenting about 17 nm signal for high concentration ligand interaction. The affinity constant is within the literature reported range,[99, 124] but the kinetic constants on intact cells have not been reported before due to the lack of a suitable technology.

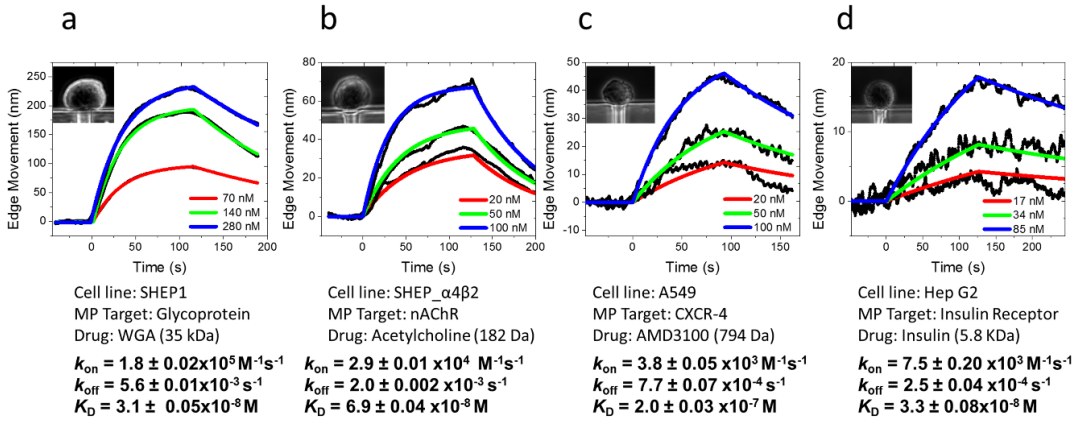

Figure 3.8 Representative binding kinetics curves of different molecular ligands to four major types of membrane proteins on cells. The cells contracted upon molecular binding, and the absolute edge movements were used to obtain binding kinetics. (a) WGA binding to glycoprotein on SH-EP1 cells (inset). (b) Acetylcholine binding to nicotinic acetylcholine receptors (ion channel) on SH-EP1- α4β2 cells (inset). (c) AMD3100 binding to CXCR-4 receptors (GPCR) on A549 cells (inset). (d) Insulin binding to insulin receptors (tyrosine kinase receptor) on Hep G2 cells (inset).

3.4.2 Validation of the Binding Kinetic Measurements with Control Experiments

To verify the cell deformation is originated from the binding of the ligands to the corresponding membrane protein receptors, we measured acetylcholine binding to wild

type SH-EP1 cells (had no nAChRs expressed on their surfaces), and did not observe cell deformation (Figure 3.9a). This control experiment shows that the deformation in the engineered SH-EP1- α4β2 cells was indeed due to the binding of acetylcholine to the nAChRs.

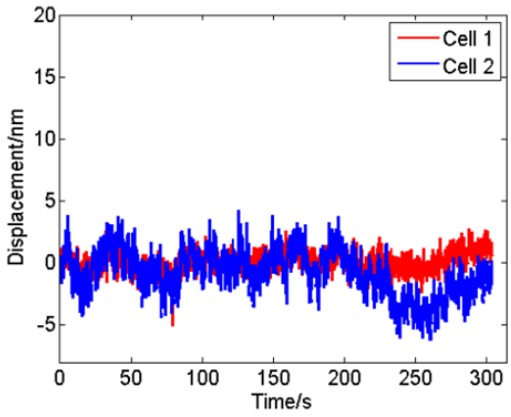

Figure 3.9 Negative Control experiments. Cell deformation (cell edge displacement) of two wild-type SH-EP1 cells to high dose (500 nM) acetylcholine. Since the wild-type cells do not express nicotinic acetylcholine receptors, the lack of cell deformation indicates the observed cell deformation in cell lines with the receptors is due to the molecular binding.

To examine if the cell deformation was resulted from a cell downstream effect triggered by the binding, we measured ligand binding to CXCR-4 receptors by blocking the downstream pathway with pertussis toxin (PTX). PTX is known to block the downstream events of many GPCRs, including CXCR4, by binding to the G protein, while leaving the GPCR outer membrane-binding sites available for the ligand to bind. We treated A549 cells with 100 ng/mL pertussis toxins in the cell culture medium for 2 hours to block CXCR-4 downstream events,[125, 126] and then measured binding of the ligands to the cells with and without PTX treatment. The binding curves are similar (Figure 3.10)

with kinetic constants of k_{on}=4.5 $\pm$ 0.03 $\times$ 10^3 $M^{-1}s^{-1}$, k_{off}=1.1 $\pm$ 0.01 $\times$ 10^{-3} s^{-1} and K_D= 0.25 $\pm$ 0.002 µM without PTX blocking and k_{on} = 2.9 $\pm$ 0.02 $\times$ 10^3 $M^{-1}s^{-1}$, k_{off}= 0.7 $\pm$ 0.01 $\times$ 10^{-3} s^{-1} and K_D = 0.24 $\pm$ 0.002 µM after downstream blocking, showing little difference in the binding kinetics. This finding indicates that the cell membrane deformation is a direct response of the cell to ligand binding, rather than due to an indirect downstream event.

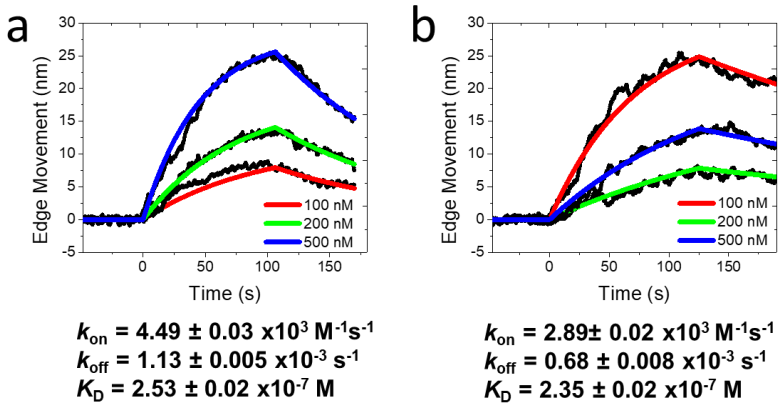

Figure 3.10 Downstream block control experiments. (a) and (b) Binding kinetics curves of untreated (a) and pertussis toxin-treated (b) A549 cells to AMD3100 with concentrations of 100, 200, and 500 nM. Pertusis toxin binds to G proteins and blocks their downstream processes. The similarity in the binding kinetics of cells with and without blocking the downstream processes shows that the cell deformation signal is not from a downstream event. A549 cells contracted upon binding, and the absolute cell deformation values (edge movements) were used to extract binding kinetics.

3.4.2 Binding of Ligands with Different Functions to Membrane Protein Receptors

After establishing that our method can be applied to different types of membrane proteins, we examined the binding of ligands with different functions to a given membrane

protein receptor, such as CXCR-4 receptor. Stromal-derived-factor-1 (SDF-1) is a natural peptide agonist, which binds to CXCR-4 and activates it. In contrast, AMD3100 is a competitive antagonist, which inhibits the activation by blocking the binding site of the receptor. Although both SDF-1 and AMD3100 bind to the same pocket of the receptor, their functions are completely different.[122] We performed binding kinetics measurements of the two ligands to A549 cells. The results (Figure 3.11) show that both the agonist and antagonist bind to the CXCR-4 receptor on A540 cells, but the binding kinetics are significantly different with k_{on}=1.2 $\pm$ 0.03 $\times$ 10^4 $M^{-1}s^{-1}$, k_{off}=9.4 $\pm$ 0.1 $\times$ 10^{-4} s^{-1} and K_D=80 $\pm$ 2 nM for SDF-1, and k_{on}=4.5 $\pm$ 0.03 $\times$ 10^3 $M^{-1}s^{-1}$, k_{off}=1.1 $\pm$ 0.01 $\times$ 10^{-3} s^{-1} and K_D=250 $\pm$ 2 nM for AMD3100.

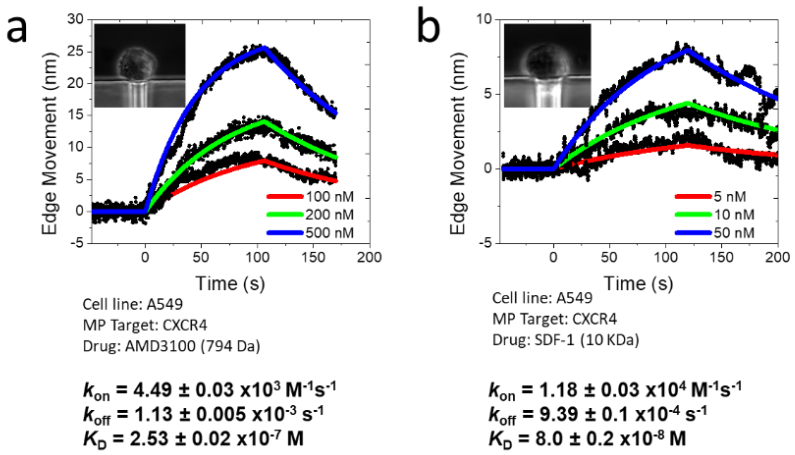

Figure 3.11 Variability of binding kinetics of different ligands to the same cell line. (a) Binding kinetic curves of antagonist AMD3100 (100, 200, and 500 nM) to CXCR-4. (b) Binding kinetic curves of agonist SDF-1 (5, 10, and 50 nM) to CXCR-4. The cells contracted upon binding, but the absolute cell deformation values (edge movements) were used to extract binding kinetics.

3.4.3 Effect of Cellular Microenvironment on Membrane Protein Binding Kinetics

An advantage of the present single cell-based assay is its ability to evaluate the effect of the membrane protein microenvironment on the molecular binding kinetics. Because different cell lines provide different lipid microenvironments to membrane protein receptors, we studied anti-EGFR binding to EGFR receptor expressed on two different cell lines, A431 cells and HeLa (Figure 3.12), and determined binding kinetic constants of $k_{on}=8.2 \pm 0.07 \times 10^4\ M^{-1}s^{-1}$, $k_{off}=3.0 \pm 0.04 \times 10^{-4}\ s^{-1}$ and $K_D=3.6 \pm 0.03$ nM for A431, and $k_{on}=4.3 \pm 0.04 \times 10^4\ M^{-1}s^{-1}$, $k_{off}=2.0 \pm 0.05 \times 10^{-4}\ s^{-1}$ and $K_D=4.6 \pm 0.04$ nM for HeLa. The differences in the kinetic constants are small but detectable for the two cell lines. This finding underscores the importance of studying membrane proteins in their native cellular environment in order to obtain accurate and physiologically relevant ligand-receptor binding kinetics.

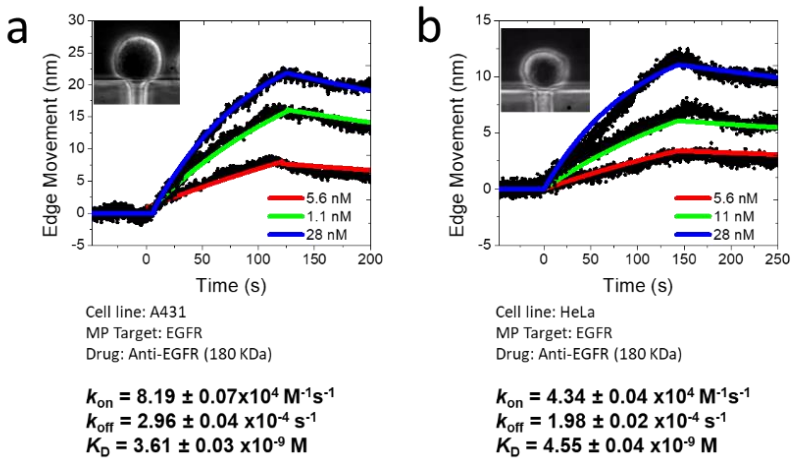

Figure 3.12 Variability of binding kinetics of same ligands to different cell lines. (a) Binding kinetic curves of anti-EGFR to EGFR on A431 cell surface. (b) Binding kinetic curves of anti-EGFR to EGFR on HeLa cell surface. The cells expanded upon binding, and

the absolute cell deformation values (edge movements) were used to extract binding kinetics.

3.4.4 Heterogeneity of Different Cells, and Different Regions of a Cell

The present method measures binding kinetics on single cells, which offers an opportunity to measure cell-to-cell variability in the binding kinetics. Before the analysis of cell-to-cell variability, we first tested the repeatability of our method to evaluate the measurement errors. The binding kinetic measurement on one cell was repeated for three times and the standard deviation of the kinetic constants were within 10% (Figure 3.13 and Table 3.1).

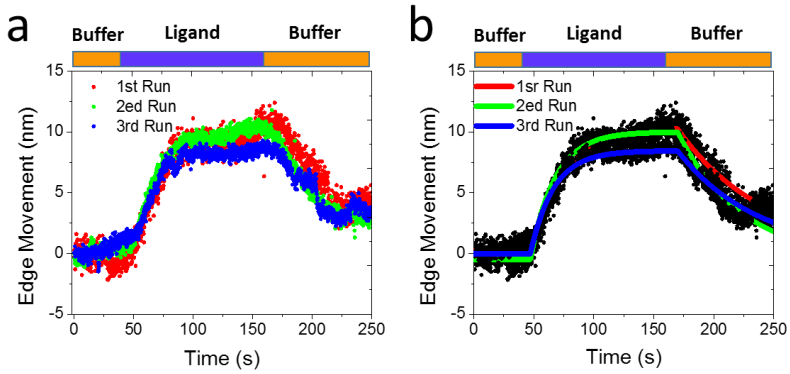

Figure 3.13 Repeatability of binding kinetic measurements. Binding kinetic curves of three repeated runs of acetylcholine (5 nM) binding with nAChRs on one single SH-EP_α4β2 cell. (a) Experimental data. (b) Fitted result.

Table 3.1 Variability of repeated binding kinetic measurements.

	$K_{on}/M^{-1}s^{-1}$	K_{off}/s^{-1}	K_D/nM
Run 1	$3.6x10^4$	$1.5x10^{-3}$	41
Run 2	$3.6x10^4$	$1.6x10^{-3}$	43
Run 3	$3.8x10^4$	$1.3x10^{-3}$	36
Mean	$3.67x10^4$	$1.47x10^{-3}$	40.0
SD	$0.12x10^4$	$0.15x10^{-3}$	3.6

Then, we measured the binding of WGA to the glycoprotein receptor on two SH-EP1 cells trapped on the same microfluidic chip simultaneously for cell-cell variation study (Figure 3.14a and b). The results revealed ~2 fold difference in the dissociation rate constant for the two cells. To further validate the finding, additional cells were tested and statistical analysis of four different membrane proteins is presented in Table 3.2. The high spatial resolution of the method also allows analysis of region-to-region variability within a cell. We examined the local variability in the binding kinetics by tracking local cell deformation along the edge of the cell (Figure 3.14c) and determined binding kinetic curves (Figure 3.14d), and observed local variations in the binding kinetics. A possible reason for this local variability is the heterogeneous membrane protein distribution on the cell surface, which is known to play an important role in cell communication and recognition.[127]

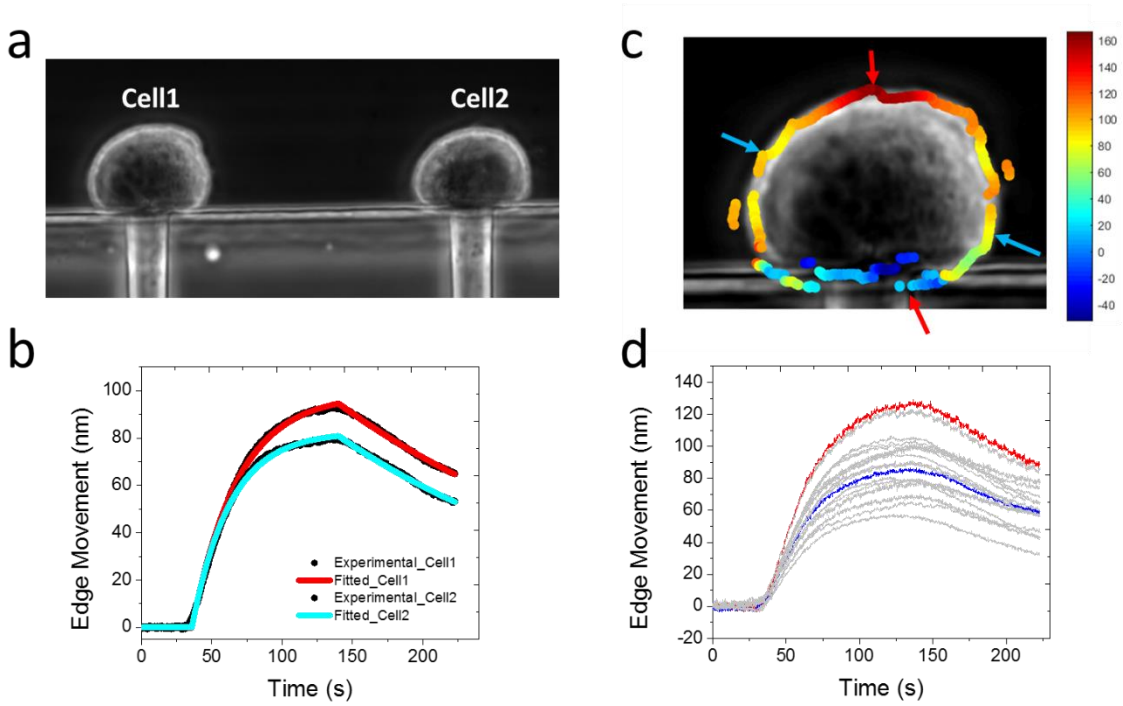

Figure 3.14 Variability of different cells and different regions of the same cell. (a) Phase contrast images of two wild type SH-EP1 cells. (b) Binding curves (edge movement) of two individual cells. (c) Variability in the cell deformation (edge movement) along the edge of a cell. (d) Binding curves (edge movement) of different locations along the edge of a cell.

Table 3.2 Statistical analysis of the association rate constants (k_{on}), dissociation rate constants (k_{off}), and equilibrium constants (K_D) for different membrane proteins (n is cell number).

Membrane Receptors/ligands	$K_{on}/M^{-1}s^{-1}$		K_{off}/s^{-1}		K_D/nM	
	Mean	SD	Mean	SD	Mean	SD
Glycoprotein/WGA (n=10)	$2.43x10^5$	$1.94x10^5$	$4.23x10^{-3}$	$3.56x10^{-3}$	17.4	6.85
nAChRs/Acetylcholine (n=14)	$1.56x10^5$	$1.39x10^5$	$5.08x10^{-3}$	$3.69x10^{-3}$	53.7	37.4
CXCR4/AMD3100 (n=10)	$7.21x10^3$	$4.04x10^3$	$1.63x10^{-3}$	$0.70x10^{-3}$	280	184
Insulin Receptor/Insulin (n=10)	$5.07x10^4$	$3.9x10^4$	$1.44x10^{-3}$	$1.7x10^{-3}$	28.4	13.1

3.4.5 Membrane Deformation Dependence on Cell Stiffness

The thermodynamic model (Eq. 3.5) predicts that ligand binding to membrane proteins causes the cell to deform, and the deformation magnitude decreases with the stiffness (bending modulus) of the cell. To examine the effect of cell mechanical stiffness on the binding-induced cell deformation, we first determined the cell stiffness by measuring cell edge movement associated with a change in the osmotic pressure created by decreasing 300 mOsm (1X PBS) to 270 mOsm (0.9X PBS). In isotonic buffer solution (300 mOsm), the cell preserves the normal shape, and it is expected to expand in the hypotonic solution (270 mOsm) as the water is transported into the cell to balance the osmotic pressure difference. We tracked the osmotic pressure-induced cell membrane expansion and used the average expansion to determine the membrane stiffness. The cell used in this study was A431 cells expressed with EGFR. We then studied the binding of anti-EGFR to EGFR receptors on the cell surface, and determined the associated cell deformation (Figure 3.15). Our result indicates that the binding-induced cell deformation in soft cells is greater than that in the stiff cells, and the mean correlation ratio is 0.96 with

the standard deviation of 0.04 (n=3). Despite the dependence of the deformation magnitude on cell stiffness, the binding kinetic constants are not affected by the cell mechanical properties (Figure 3.15).

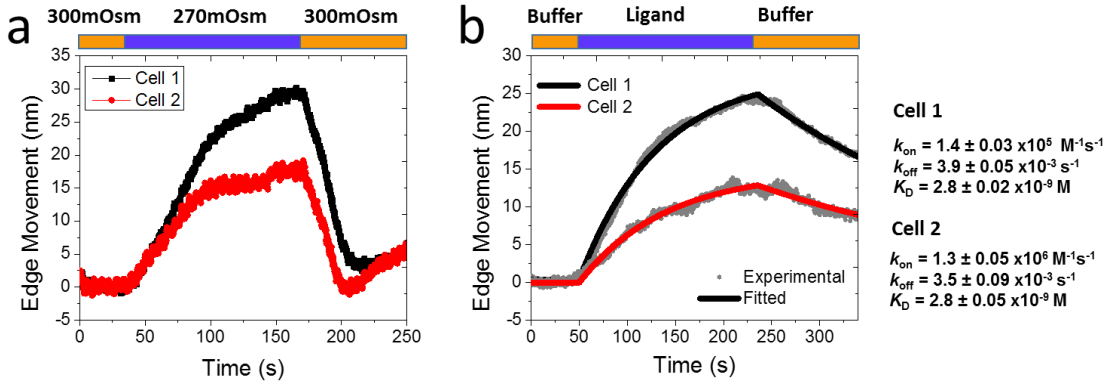

Figure 3.15 Dependence of binding-induced cell deformation on cell stiffness. (a) Cell edge deformation associate with osmotic pressure introduced by switching the buffer from 300 mOsm (1X) to 270 mOsm (0.9X) PBS. (b) Cell deformation and kinetic constants associated with the binding of anti-EGFR to EGFR.

3.4.6 Membrane Deformation Dependence on Receptor Density

The thermodynamic model also predicts that the binding-induced cell deformation is proportional to the density of the expressed membrane proteins on a cell surface. We examined this prediction by measuring the binding of anti-EGFR with EGFR on different cell lines, which are known to express EGFR with different densities.[104] These cell lines include A431 cell, HeLa cell, A549 cell and Hek 293 cell (Figure 3.16), and the EGFR densities are 1.2, 0.53, 0.28, and 0.02 million per cell, respectively.[92, 104] The binding curves for these cell lines were calibrated and normalized with the osmotic pressure-induced cell deformation (using 0.9X PBS, 270 mOsm). The data shows that the cell

deformation increases with EGFR density, which is in agreement with the thermodynamic model (Eq. 3.5).

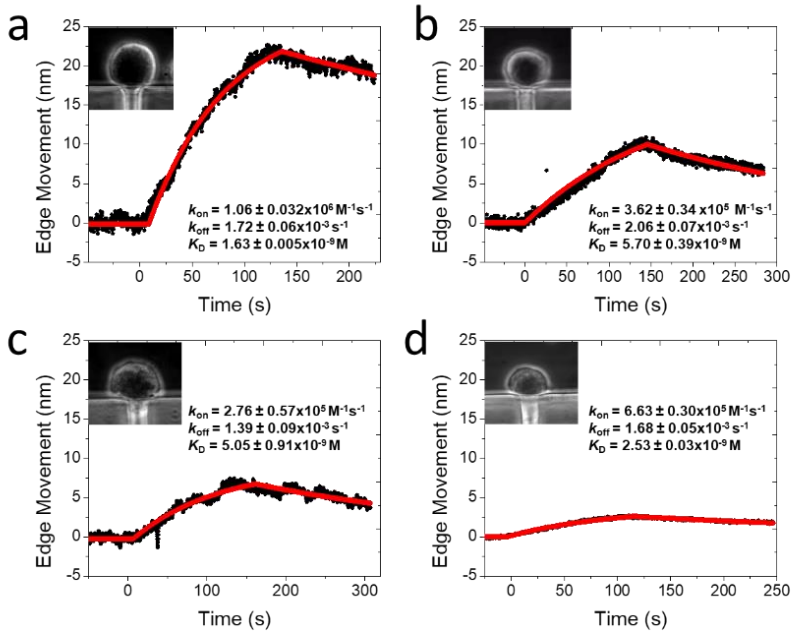

Figure 3.16 Dependence of cell deformation on receptor density. Optical images of trapped cells (insets), and Anti-EGFR –EGFR binding curves for (a) A431, (b) HeLa, (c) A549, and (d) Hek 293 cell lines. The cells expanded upon anti-EGFR-EGFR binding, and the absolute edge movements were used to extract binding kinetics.

We analyzed multiple cells and plotted the distribution vs. the receptor density (Figure 3.17), and observed a clear correlation between the binding-induced cell deformation and receptor density.

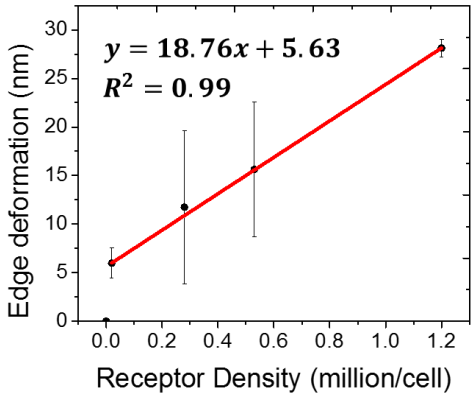

Figure 3.17 Cell deformation vs. Receptor density. Linear correlation between the magnitude of the cell deformation and receptor density on cell surface.

We also examined possible dependence of the cell deformation on the binding kinetic constants (Figure 3.18) but found no obvious correlation between them. This observation is also consistent with the thermodynamic model.

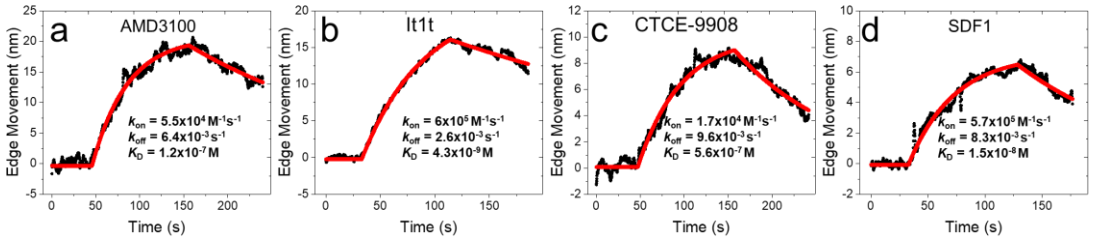

Figure 3.18 No correlation between the magnitude of the cell deformation and binding kinetic constants. Cell deformation and kinetic constants for (a) AMD3100-CXCR-4 binding, (b) It1t-CXCR-4 binding, (c) CTCE-9908-CXCR-4 binding, and (d) SDF1-CXCR-4 binding.

3.4.7 Comparison of Fixed and Live Cells

In this work, we mainly focused on the fixed cells for binding kinetic measurements, because it minimizes cell micro-motion (Figure 3.19).

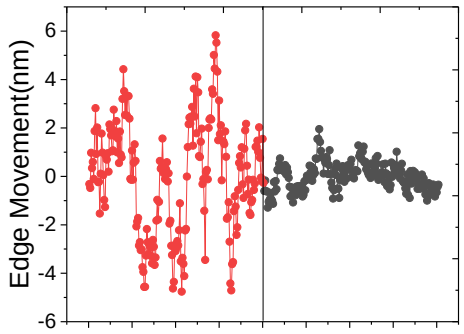

Figure 3.19 Cell membrane fluctuation decreases after fixation.

The fixation used 4% paraformaldehyde (PFA), the most common fixation that has been widely used for various immune-assays using fluorescence and other detection technologies. This procedure may crosslink proteins at certain epitopes, and could thus affect the binding kinetics. However, it has been shown that only several amino acids (e.g., lysine and tryptophan side chains) can be easily cross-linked by the fixation, and even for these amino acids, the crosslinking rate is between 3-22% [128-131] after 48 h fixation. In the present work our fixation time is brief (10 mins) at 4% PFA, which should significantly reduce the chance of crosslinking in the binding pockets of the target membrane proteins. Additionally, the formaldehyde cross-links are reversible in buffer solutions,[132] so a majority of the membrane proteins, especially their binding pockets, are expected to remain intact. To further examine the possible fixation effect, we carried out the binding kinetic measurements on living cells (Figure 3.20). Despite of the increased noise and difference in the absolute amount of cell deformation in the living cells, the binding kinetic constants are similar within the experimental uncertainty for fixed and living cells examined here.

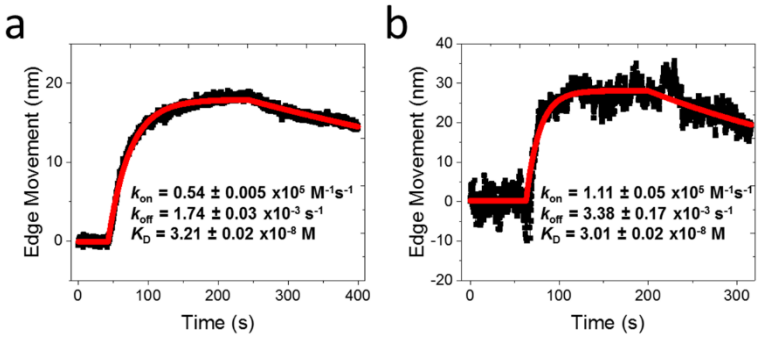

Figure 3.20 Comparison of fixed and live cells. WGA- glycoprotein binding kinetic curves on (a) fixed and (b) live SH-EP1 cells (WGA concentration=200 nM). The SH-EP1 cells contracted upon WGA binding, and the absolute edge movements were used to extract binding kinetics.

To further compare the binding kinetics of fixed and live cells, the statistical analysis of multiple cells were performed. Figure 3.21 shows the comparison of k_{on}, k_{off} and k_D between fixed and live cells. No significant difference were observed between fixed and live cells.

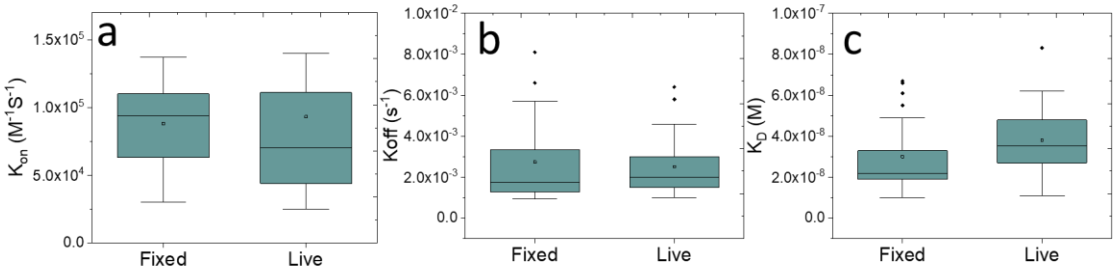

Figure 3.21 The statistical comparison of binding kinetics between fixed and live cells. (a) Association rate constant k_{on}. (b) Dissociation rate constant k_{off}. (c) Binding kinetic constant k_D. (n=21)

Molecular binding to membrane proteins is critical for both cellular function study and drug development, which has motivated researchers to develop various detection

technologies. The current detection technologies fall into two categories: labeled and label-free methods. The former includes fluorescence methods (e.g., TIRF), which are typically end-point assays, and thus not for kinetics. The latter includes SPR and other optical and mechanical methods. These methods allow real time tracking of binding kinetics, but often face challenges of detecting small molecules (low molecular mass ligands). The method presented here measures molecular binding by tracking binding-induced cell deformation at sub-nm with an optical tracking method. It is label-free, yet its detection sensitivity does not diminish with molecular mass, which is thus capable of studying both large and small molecules. Furthermore, by integrating the sensitive optical cell edge tracking method with a microfluidic device, single cells can be trapped and analyzed, which is particularly attractive for studying suspension cells. The basic principle of the present detection method, as described with a thermodynamic model, is universal. Predicting the actual amount of the molecular binding-induced cell deformation (contraction or expansion) with the model requires details of the ligand-membrane receptor interactions, and cell mechanical properties. However, the binding kinetics measures how fast a ligand binds to its receptor, which is determined by the time evolution of the cell deformation, rather than by the amount of cell deformation.

3.5 Conclusion

In this chapter, we described a label-free optical detection method coupled with a microfluidic device to measure the kinetics of both large and small ligands binding with membrane protein receptors on whole cells. The method uses a microfluidic chip to trap individual suspended cells onto microfabricated holes, and measure the molecular binding

induced-cell membrane deformation of the trapped cells with sub-nanometer precision. Using the method, we studied the molecular interactions of large and small molecule ligands, and agonists and antagonists with four major types of membrane proteins (glycoprotein, nAChR, CXCR-4 and insulin receptors), demonstrating the capability of measuring both large and small molecule binding kinetics with membrane proteins on whole cells. We developed a thermodynamic model to describe the basic mechanism of the method, and validated the model by changing the cell stiffness, receptor density and binding kinetics. The single-cell detection capability revealed variability in the binding kinetics of a membrane protein receptor expressed on different cell lines, demonstrating the importance of the cellular microenvironment in membrane protein functions. The method offers single cell detection capability, which enabled the study of heterogeneity in the membrane protein binding within the same cell line. The microfluidic design allowed trapping of the individual cells, measuring the binding kinetics, and then releasing the trapped cells, thus potentially compatible with high throughput need for studying multiple cells.

CHAPTER 4 MEASUREMENT OF MOLECULAR INTERACTION INDUCED DOWNSTREAM EFFECT WITH MECHANICAL TRACKING METHOD

4.1 Introduction

By tracking the cell membrane deformation, we have successfully measured the small molecules interaction with membrane proteins on cell surface. To further explore this mechanical tracking methods, we applied this platform on live cell function measurements. One example is the monitoring of granule exocytosis on single cells.

Granule exocytosis is a basic cellular process that secrets intracellular substances, such as neurotransmitters, hormones and enzymes, for various functions, including cell-cell communications, synaptic signal transmission and cellular metabolism.[133-135] Uncontrolled exocytosis results in cell proliferation, migration, invasion and tumor development.[136] Tracking of granule exocytosis in real time is critical for both understanding normal cellular functions and detecting cellular disorders.

Current methods of monitoring granule exocytosis mainly rely on electrophysiological recording, electrochemical detection and fluorescence imaging.[137-139] The electrophysiological recording method measures cellular membrane capacitance by the whole cell patch clamping technique.[140, 141] As the membrane capacitance is proportional to the membrane area, granule fusion during synaptic exocytosis and endocytosis is thus detected as it changes the membrane area.[142, 143] Although powerful, the membrane capacitance reflects an overall cellular surface area change, which does not provide the spatial information of an exocytosis event. Furthermore, the electrophysiological recording method has limited throughput because it measures one cell

at a time. The electrochemical method detects the oxidation current of molecules released from granules with a microelectrode,[144-150] which can quantify the amount of the secretory molecules with high sensitivity, but it is limited to granules containing electroactive species. The fluorescence imaging approach [151] can detect individual granule exocytosis events with high spatial resolution,[152-156] but its temporal resolution is limited by the number of photons emitted from the fluorophores. The fluorescence imaging requires the introduction of the fluorescent dye to the granule, and the signal does not provide direct information on the cell membrane changes during granule release.

In this chapter, we report a label-free method to image single granule exocytosis events by tracking granule fusion-induced local mechanical deformation in cellular membrane with sub-nm precision and milliseconds temporal resolution. We achieve this capability with a phase contrast imaging method and a differential optical tracking algorithm. Using this capability, we monitor the granule release events in single cells and map the spatial distribution of the cell membrane deformation induced by the granule fusion and its evolution over time. From the temporal and spatial patterns, we identify different types of granule release. We also monitor the granule release processes by simultaneous fluorescence recording to validate the label-free cell membrane deformation tracking method. The simultaneous cell membrane deformation detection and fluorescence recording allow the study of the propagation of the granule release induced membrane deformation along cellular membrane surfaces.

4.2 Materials and Methods

Materials. Monoclonal anti-Dinitrophenyl (anti-DNP) IgE, fluorescein isothiocyanate-dextran (FITC-dextran) and serotonin molecules were purchased from Sigma-Aldrich (St. Louis, MO). 2,4-dinitrophenylated albumin from bovine serum (DNP-BSA) was purchased from Life Technologies (Carlsbad, CA). All solutions used in the experiments were prepared with home-made fresh extracellular buffer (135 mM NaCl, 5 mM KCl, 20 mM HEPES, 1.8 mM $CaCl_2$, 1 mM $MgCl_2$, 5.6 mM glucose, pH = 7.4). All reagents were analytical grade from Sigma-Aldrich, except those stated.

Cell culture. RBL-2H3 cells were purchased from American Type Culture Collection (ATCC, Rockville, MD). RBL-2H3 cells were cultured in a humidity incubator at 37˚C with 5% CO_2 and 70% relative humidity. Eagle's Minimum Essential Medium (EMEM, ATCC 30-2003) with 15% heat inactivated Fetal Bovine Serum (FBS, Life Technologies, Carlsbad, CA) and 1% penicillin-streptomycin (BioWhittaker, Basel, Switzerland) were used as culture medium for cell growing. RBL-2H3 cells were cultured in 25 cm^2 flask and passaged when approximately 80% confluence was reached. 0.05% trypsin-EDTA (Life Technologies, Carlsbad, CA) was used for cell passage.

Granule release initiation. For granule exocytosis experiment, the RBL-2H3 cells were transferred to 35 mm diameter tissue culture petri dish (Corning Inc., Corning, NY) for overnight culture. 200 μM serotonin, 0.5 μg/ml monoclonal anti-Dinitrophenyl (anti-DNP) IgE and 1 mg/ml fluorescein isothiocyanate-dextran (FITC-dextran, molecular weight 150,000) were added to the culture medium for granule release preparation. Serotonin was used to increase the size of granule [157]. FITC-dextran was used to label

the cells for simultaneous tracking of granule release with fluorescence imaging and cell membrane deformation. Anti-DNP IgE was used to bind with the cell surface expressed high affinity IgE receptors (FcεRI). When the antigen, 2,4-dinitrophenylated albumin from bovine serum (DNP-BSA) was added, the binding of DNP-BSA to anti-DNP IgE will make the cross-linking of FcεRI which initiates a signaling cascade leading to degranulation of the cells and release of chemical mediators (Figure 4.1).

Before measurement, the RBL-2H3 cells were rinsed with 0.1% BSA in extracellular buffer (135 mM NaCl, 5 mM KCl, 20 mM HEPES, 1.8 mM $CaCl_2$, 1 mM $MgCl_2$, 5.6 mM glucose, pH = 7.4) for three times to block the surface followed by another three times wash with extracellular buffer only to remove the extra BSA. The petri dish with cells in 1 ml extracellular buffer was moved on the microscope for imaging. Recording of both phase contrast and fluorescent images was right after addition of 1 ml 5 μg/ml DNP-BSA into the petri dish.

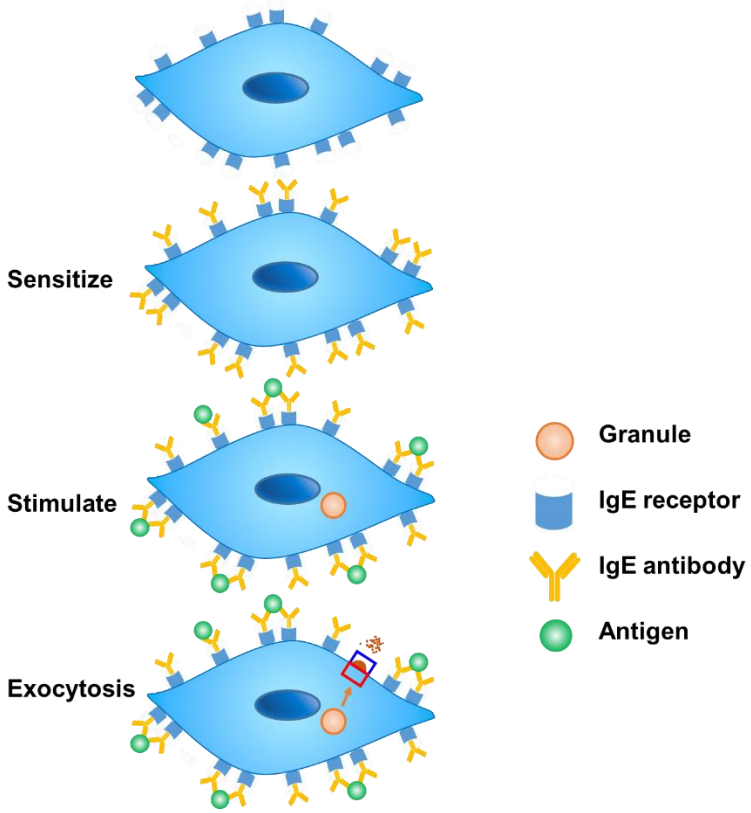

Figure 4.1 Granule exocytosis initiation.

Optical setup. An inverted microscope (Olympus IX81) equipped with a phase 2 condenser and phase 2 40X objective was used with illumination from the top of the sample cells (Figure 4.3a). Top illumination light pass through a long pass filter with 600 nm cut-on wavelength before illuminating on cell sample. The phase contrast image was recorded by a Hamamatsu camera with frame rate of up to 400 fps after another long pass filter with 600 nm cut-on wavelength. A set of optical filters (Ex420-480/Em515) was used for the fluorescence imaging and another Hamamatsu camera was used for recording with frame rate of 8 fps. With a beam splitter, both of the phase contrast image and fluorescence image were able to be obtained simultaneously through the microscope side port. To synchronize the recording time of the phase contrast and the fluorescent image sequences, a shutter was

used to cut off the light path to black out both images as a time mark. By carefully aligning the intensity versus time plots of fluorescent and phase contrast images (Figure 4.2), the two recordings are synchronized.

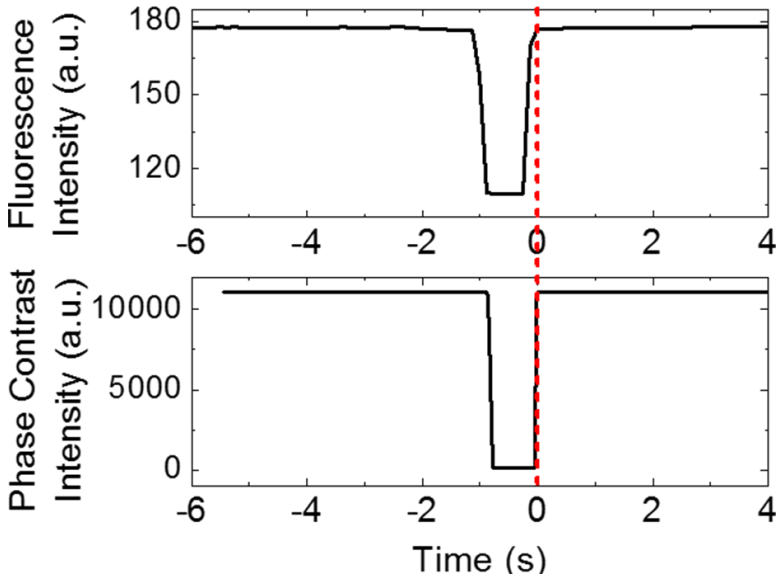

Figure 4.2 Recording synchronization.

Fluorescence imaging. The fluorescence signal of granule release was obtained with fluorescein isothiocyanate–dextran (FITC-dextran), which was added to the cell before overnight culture. FITC-dextran was sensitive to the pH of the medium. Before granule release, the fluorescence signal of FITC-dextran was quenched by the low-pH of granule medium, and during granule release, the fluorescence signal was activated by neutral pH extracellular medium, giving a bright spot as fluorescence signal. The fluorescence image was captured simultaneously with the phase contrast images for granule release validation. The following optical filters were used to obtain the fluorescence image: excitation filter 420-480 nm, emission filter 515 nm.

Signal Analysis. The cell membrane deformation in color scale was obtained by tracking the whole cell edge with the differential edge tracking method (Figure 4.4) and plot the maximum membrane deformation magnitude at the time period that the granule release happened. To get the localized distribution of the membrane deformation upon granule release, the membrane deformation along an 8 μm-long edge that is close to the granule release position was tracked. The temporal profile of membrane deformation at different locations along the localized edge was extracted and plotted. By averaging these membrane deformation of different locations, the temporal profile of the granule release was obtained. The spatial profile was plotted by extracting the membrane deformation magnitude of different positions near the time point where the deformation is maximum. By fitting of the spatial distribution profile with Gaussian distribution, the peaks of each granule releases were resolved and the full width at half maximum (FWHM) was calculated as the effective expansion area. The 2D temporal-spatial correlation was the mapping of the membrane deformation value along this 8 μm long cell edge over the granule release time period.

4.3 Detection principle

We studied granule release in RBL-2H3, a rat basophilic leukemia cell line The RBL-2H3 cell surface were expressed with immunoglobulin E (IgE) receptors (FcεRI),[152] which were activated by IgE antibody binding. Degranulation in the cells were initiated by specific binding of an antigen to the IgE antibody on the cell surface,[158] during which the granule docks and interacts with the plasma membrane of the cells (Figure 4.1). To investigate the plasma membrane responses during the granules release, as well as

to validate the granule release by fluorescence, a dual-optical system was developed with both phase contrast imaging and fluorescence imaging. As shown in Figure 4.3a, the phase contrast imaging is obtained with a top illumination for cell morphology recording, and the fluorescence imaging is recorded with a bottom excitation for granule release validation. In the phase contrast-imaging pathway, two 600 nm long pass filters (f1 and f4) were used to avoid the interference from fluorescence signal. In the fluorescence imaging pathway, a filter set (f2: Ex = 420-480 nm, f3: Em = 515 nm) was used to selectively detect the fluorescence signal from granule release. FITC-dextran was used as the fluorescence reporter to validate the granule release, which was sensitive to the pH of the medium. Before granule release, the fluorescence signal was quenched by the low-pH of granule medium, and during granule release, the fluorescence signal was activated by the neutral pH of extracellular medium. With a beam splitter, both of the phase contrast image and fluorescence image were able to be obtained simultaneously through the microscope side port. Figure 4.3b show the phase contrast image and the corresponding fluorescence image from the same sample location, respectively.

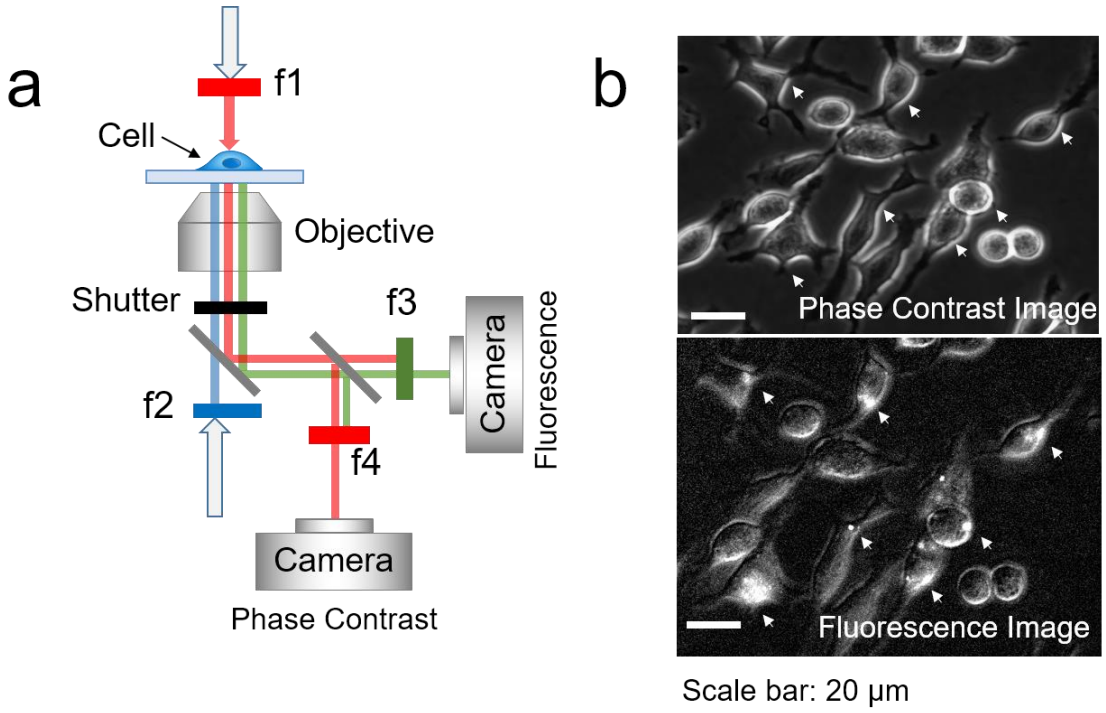

Figure 4.3 Schematic illumination of the dual-optical system. (a) Schematic illumination of the imaging setup based on an inverted phase contrast microscope with 40x phase 2 objective. A top mounted white light source passes through a 600 nm long pass filter (f1) and illuminates on sample cells. Phase contrast images are recorded by a camera after another 600 nm long pass filter (f4) to separate from the fluorescence imaging signal. A bottom mounted mercury lamp and a set of fluorescence image filters (excitation wavelength 420 nm – 480 nm (f2), emission wavelength at 500-550 nm (f3)) are used for fluorescence imaging. A shutter is used to block both phase contrast and fluorescence light for time synchronization of the two imaging modes. (b) Phase contrast image and the Fluorescence image of RBL-2H3 cells. The white arrows mark the position where there is a granule release. The bright spot in fluorescence image pointed by the white arrow is due to the fluorescence from granule release.

To sensitively measure the exocytosis induced membrane deformation, we used a differential optical method for edge tracking (Figure 4.4). From the phase contrast imaging, the edge of the cells can be clearly resolved (Figure 4.3b). To track the edge deformation, a rectangular region of interest (ROI) is defined such that the edge of a cell passes through the center of the rectangle. The rectangular ROI is divided into two equal halves, with one half inside of the cell (red) and the other half outside of the cell (blue, Figure 4.4a). When the cell plasma membrane deforms, the image intensity of one half increases, and the other half decreases. The differential image intensity of the two halves is defined as, $(I_1-I_2)/(I_1+I_2)$, where I_1 and I_2 are the intensities of the first and second halves, respectively, and used to determine the cell edge movement at each location. The calibration between the differential image intensity and the cell edge movement is determined experimentally (Figure 4.4b, c and d). This differential optical detection subtracts the common noise in optical system, thus providing high detection limit.

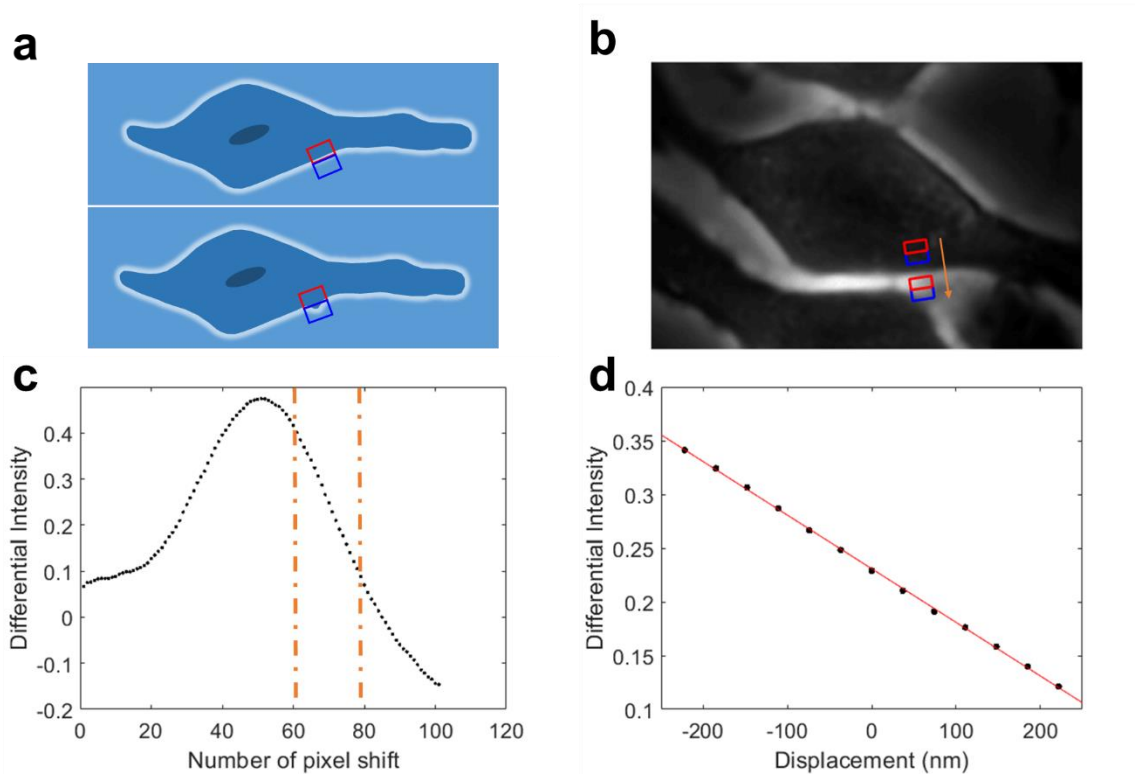

Figure 4.4 Edge deformation tracking with differential detection method. (a) Illustration of cell edge changes during the granule release, measured by differential detection method. Red and blue rectangles are the region of interest (ROI) for differential detection. (b) The optical tracking method was calibrated by shifting the ROI by different numbers of pixels from inside to outside of the cell in the direction perpendicular to the tangential line at the cell edge. (c) The differential intensity change during the ROI shifting, in which a linear region (dotted line marked) is used for membrane deformation calibration. (d) A typical calibration curve to determine the cell deformation from the differential image intensity.

4.4 Granule Release Measured by Tracking Cell Edge Deformation

4.4.1 Temporal Evolution of Granule Release induced Cell Membrane Response

To demonstrate the capability of measuring granule exocytosis with cell plasma membrane responses, the RBL-2H3 cells were labeled by FITC-dextran and the granule release was triggered by DNP binding to anti-DNP IgE on cell surface. The granule release induced cell edge membrane deformation was observed. One example is shown in Figure 4.5a, a rapid expansion is detected from the edge where granule release occurred. The simultaneous recording of the fluorescence signal was used to validate the granule release process. As is shown in Figure 4.5b, an obvious fluorescence peak signal was detected at the same time period and location. Therefore, by tracking the cell edge deformation, we were able to monitor single granule release event in single cells.

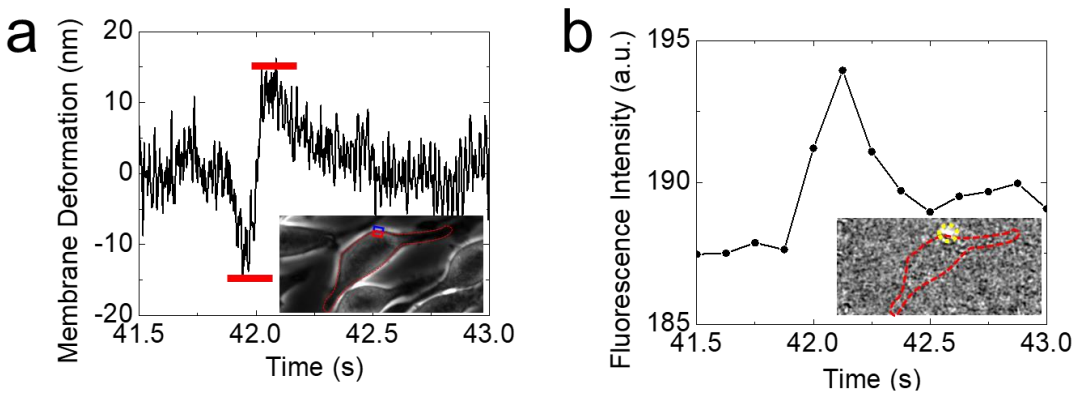

Figure 4.5 One example of granule release induced cell edge deformation and fluorescence signal. (a) Cell edge deformation over time at the location marked with the red and blue ROIs. (b) Fluorescence intensity change during the granule release event in (a) at the location marked with yellow dashed circle.

To further confirm that the observed membrane expansion was related to granule release, we examined membrane deformation at other locations along the cell edge during the granule release and found that the stepwise cell deformation occurred only near the location of the fluorescence emission (Figure 4.6).

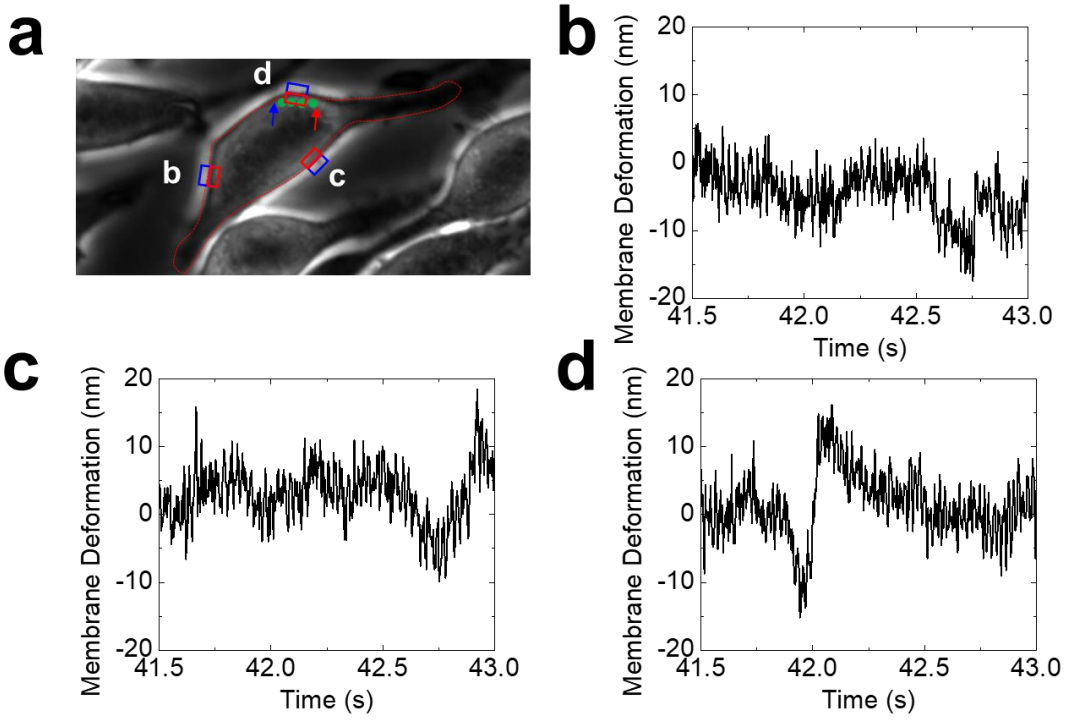

Figure 4.6 Cell edge deformation at different locations along the cell edge. (a) Phase contrast image of a RBL-2H3 cell. The blue and red rectangles are regions of interest (ROI) that mark the locations labeled by letter b, c, and d. (b-d) Cell edge movement at the locations marked by b, c and d, respectively.

After the study of granule release events in different cells, two representative types of membrane deformation were observed. The first type exhibits a rapid expansion of the cell edge upon granule release followed by slow or little recovery. We refer this type of granule release to as Type 1. One such example shown in Figure 4.7a is a cell that expands

by ~18 nm over 0.125 s followed by small recovery at the location marked by a red arrow in the phase contrast images (Figure 4.7a1-a4). Figures a1-a4 are snapshots of the phase contrast images at time points marked by I, II, III and IV on the temporal profile of the cell deformation in Figure 4.7a. The cell deformation is too small to be visible in the phase contrast images, so the magnitude of the cell deformation determined by the differential tracking method is represented with a color scale overlaid on the phase contrast images (Figure 4.7a1-a4). The insets in Figure 4.7a1-a4 are zoom-in images of the cell deformation.

To validate that the cell expansion in Type 1 is due to a granule release event, we compared the cell deformation images with the simultaneously recorded fluorescence images (Figure 4.7a and Figure 4.7b). The fluorescence images (after background subtraction) show a bright spot due to fluorescence emission at the location marked by a dashed circle (Figure 4.7b1-b4). The location of the observed fluorescence emission coincides with that of cell expansion, which confirms that the cell edge expansion is due to granule release. Unlike the stepwise cell expansion detected by the differential tracking method, the fluorescent emission shows a rapid increase followed by a rapid decrease during the granule release event, which are due to plasma membrane fusion (I), during fusion (II), and diffusion of fluorescein isothiocyanate–dextran (FITC-dextran) (III and IV, Figure 4.7b).

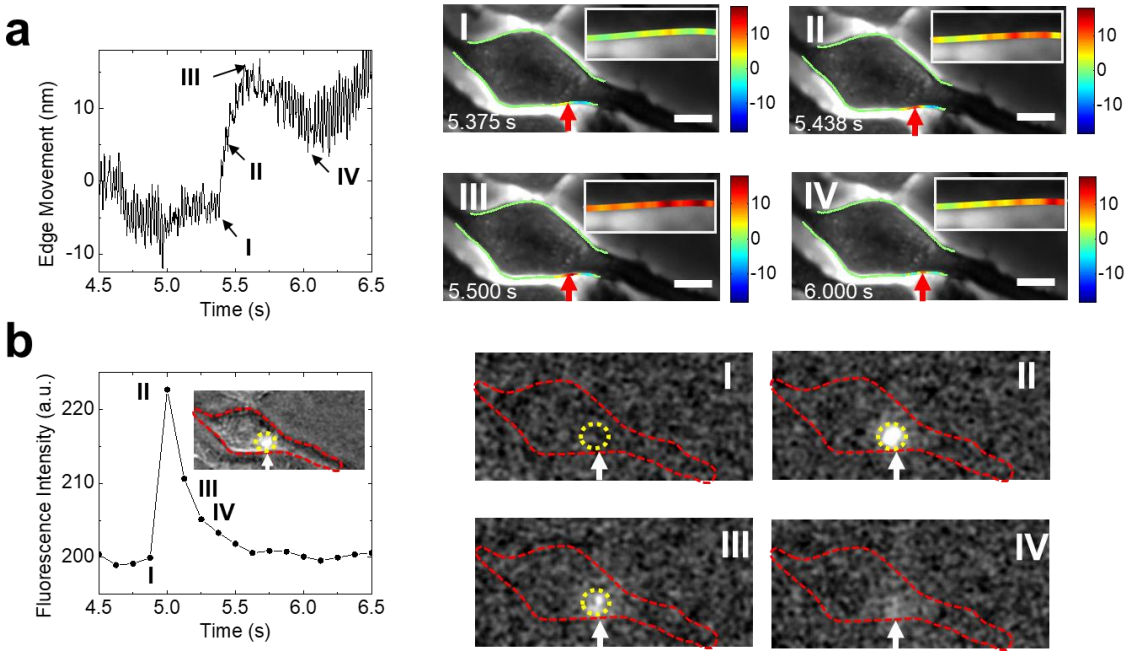

Figure 4.7 . Type 1 cell edge deformation. Granule releases measured by cell edge tracking and validated by fluorescence imaging, showing two representative types of cell edge deformation (a) Type 1 cell edge deformation over time at the location marked with the red arrows in the snapshots of phase contrast images at the time points marked by I, II, III and IV. Insets: zoom-in images of the cell edge deformation location. (b) Fluorescence intensity change during the granule release event in (a) at the location marked with yellow dashed circle and the fluorescent images at the time points marked by I, II, III, and IV (first frame subtracted out). Inset: fluorescence image of the cell, where the red dashed line marks the cell edge. The red arrows in a and the white arrows in b point to the location of granule release.

The second type of cell deformation observed during granule release is pulse-like, a rapid expansion followed by a complete recovery. Figure 4.8 is the temporal profile of cell deformation of a such case, where I, II, III and IV mark different stages of the cell

expansion. The time duration is 0.020 s, much faster than the stepwise expansion in Type 1. We refer this type of membrane deformation to Type 2. The location of the cell deformation is marked by a red arrow in the snapshots of the phase contrast images at the time points of I, II, III and IV. The simultaneously recorded fluorescence images during this granule release event shows an obvious bright spot near the cell deformation position (Figure 4.8b1-b4). The temporal profile of the fluorescence emission displays a sharp increase followed by a decrease, which is similar to that in Type 1. However, the fluorescence peak intensity is significantly lower than that in Type 1. We also tracked cell deformation along the entire cell edge and detect significant edge deformation near the fluorescence emission spot only.

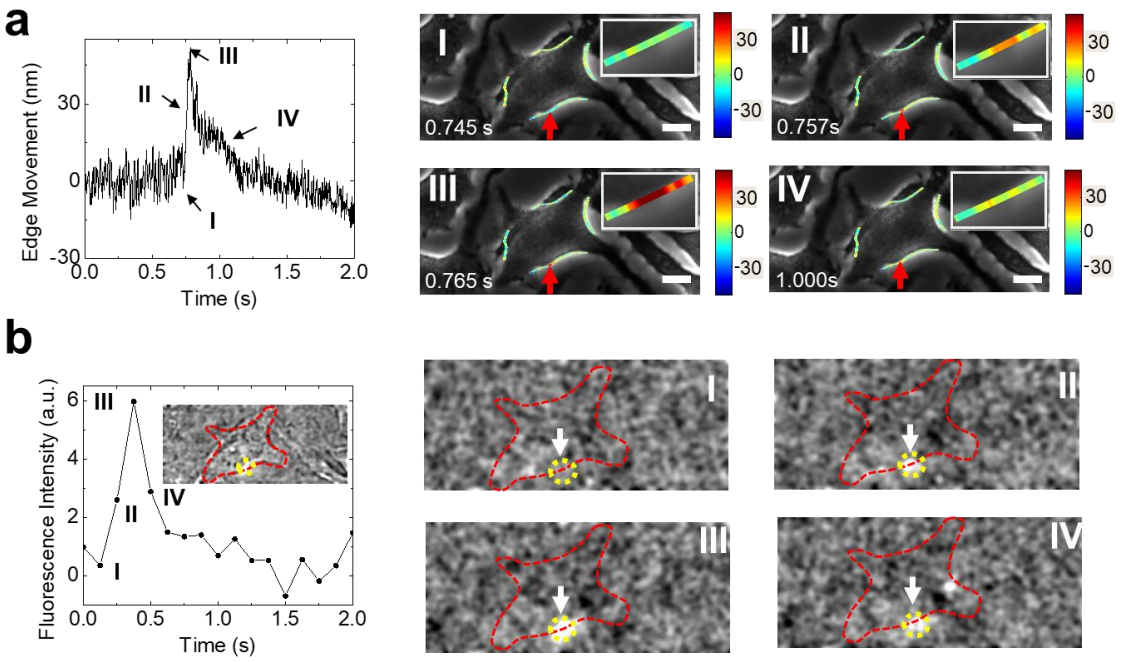

Figure 4.8 Type 2 cell edge deformation. Granule releases measured by cell edge tracking and validated by fluorescence imaging. (a) Type 2 cell edge deformation over time at the location marked by the red arrows in the snapshots of phase contrast images at the time

points marked by I, II, III and IV. Insets: zoom-in images of the cell edge deformation location. (b) Fluorescence intensity change during the granule release event in (a) at the location marked with yellow dashed circle and the fluorescent images at the time points marked by I, II, III, and IV (first frame subtracted out). Inset: fluorescence image of the cell and the cell edge is depicted by red dashed line. The red arrows in a and the white arrows in b point to the location of granule release. Scale bar: 10 μm.

We analyzed 130 individual granule release events from the fluorescent signals in 52 cells and found that 110 granule release events showed detectable edge deformation. The histogram distribution of the granule release induced membrane deformation is present in Figure 4.9. For the cells that show deformation during granule release, ~90% of them display Type 1 deformation and ~10% show Type 2 deformation. Type 1 cell deformation indicates an increase in the cell area that sustains after granule release, which is consistent with the typical stepwise capacitance responses.[159] We thus attribute Type 1 to a full fusion process, where a granule fuses into the cell membrane after releasing its chemical content. In contrast, Type 2 cell deformation shows only transient increase in the cell area and cell edge returns to the pre-granule release position quickly, similar as the capacitance flickers observed with patch-clamp techniques.[159] This type of membrane response to granule release is consistent with 'kiss-and-run' process, where the granule interacts with the cell membrane and release its content to the outside of the cell via a transient fusion pore while preserving granule integrity and then detach from the cell membrane. The fluorescent signal of Type 2 deformation is much smaller than Type 1 deformation, which is likely due to the partial release of granule in 'kiss-and-run' process.[160, 161]

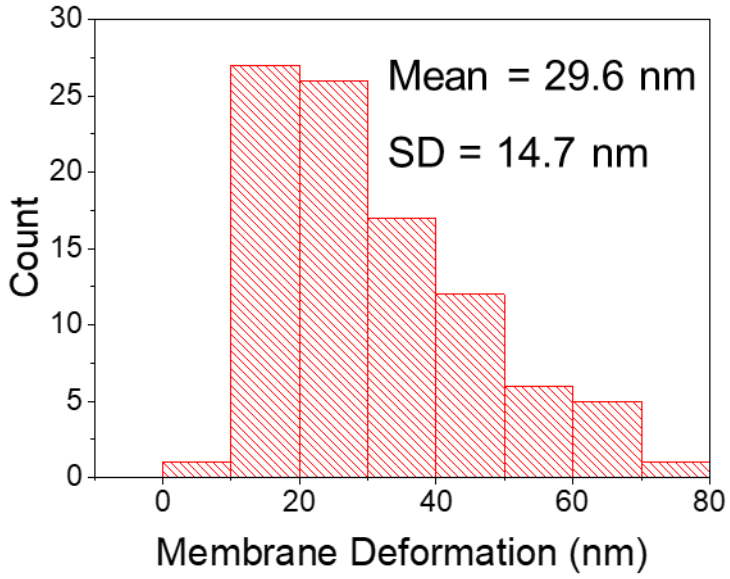

Figure 4.9 The distribution of the membrane deformation magnitude induced by different granule release events (n=95).

4.4.2 Localized Cell Membrane Deformation Due to Granule Release

The cell edge tracking method provides spatial and temporal resolutions, which allowed us to reveal complex membrane responses and resolve multiple granule releases that took place close in time and location. We determined cell membrane deformation along the entire edge of a cell during a granule event (Figure 4.10a) and obtained both temporal (Figure 4.10b) and spatial (Figure 4.10c) profiles of the membrane response to a granule release event. To examine the correlation between the temporal and spatial evolution of the granule release event, we extracted a 2D temporal-spatial correlation map (Figure 4.10d).

The cell shown in Figure 4.10 corresponds to the Type 1 cell deformation, where the color scale represents cell deformation magnitude. To examine the localized

distribution of the cell edge deformation upon granule release, the membrane deformation was extracted over time along an 8 μm-long cell edge (marked by arrows in Figure 4.10a). Figure 4.10b shows the cell edge membrane deformation at different locations along the localized edge. By plot cell deformation magnitude near the time point where the deformation is maximum, the spatial distribution of the granule release-induced membrane response is obtained (Figure 4.10c). Fitting the spatial distribution with a Gaussian function leads to a full width at half maximum (FWHM) of ~2 μm, which measures the spread of the cell deformation from the point of granule release. 2D temporal-spatial correlation of this granule release event reveals more complete information on the spatial distribution and temporal evolution of the cell deformation (Figure 4.10d). For example, it shows that maximum deformation shifts in location over time, indicating that the granule fusion induced membrane deformation propagates along the cell edge. From the slope of the line marked on Figure 4.10d, the membrane deformation propagation speed is about 5 μm/s. The propagation along the cell edge lasted for more than 0.5 s.

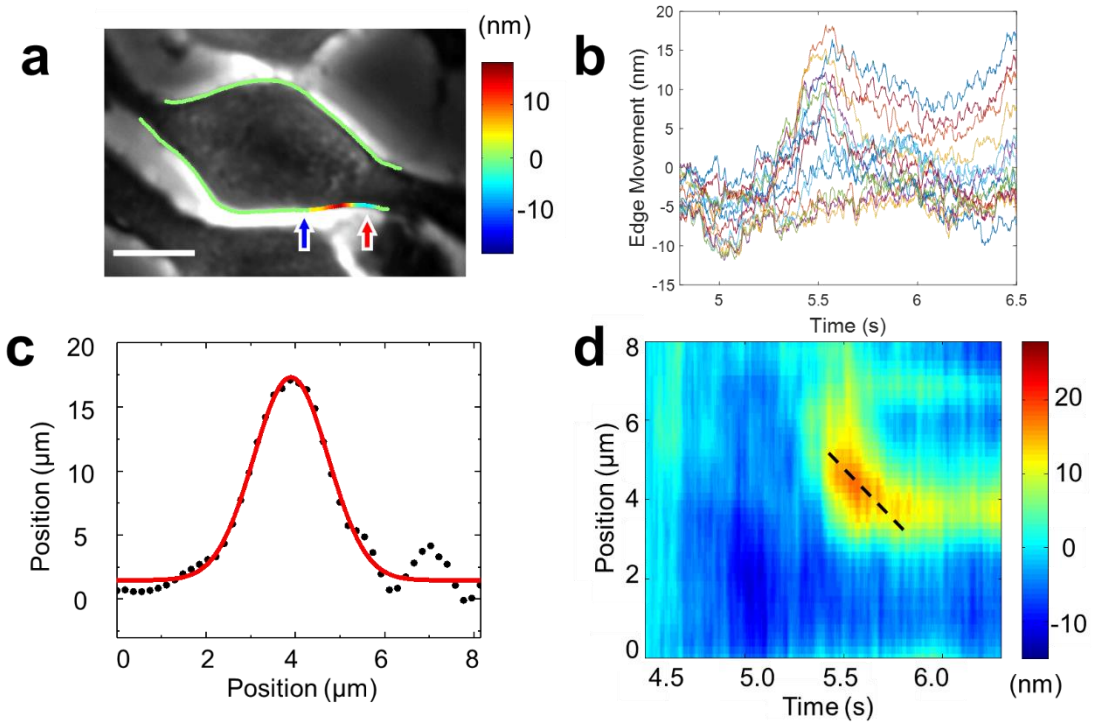

Figure 4.10 Temporal-spatial correlation between membrane edge deformation and granule of a cell with Type 1 release. (a) Phase contrast images of RBL-2H3 cell overlapped with corresponded edge movement. The color represents the amount of cell membrane deformation in nm. Red and blue arrows marked the localized edge area being analyzed. (b) The plasma membrane responses of different locations along the localized edge area marked red and blue arrows. (c) The cell membrane edge deformation amount along the localized edge area between the red and blue arrows. (d) 2D plot of cell edge movement with x axis in time, y axis in position. The region are between the cell edges indicated by the red and blue arrows. The color represents the cell edge change in nm.

Figure 4.11 show the Type 2 cell deformation, where the color represents the local magnitude of the deformation. The cell deformation in this case appears to be more localized and decay rapidly over time. 2D temporal-spatial correlation (Figure 4.11d) of

this granule release shows a well-defined spot, indicating that the edge expansion is confined in both time and location. Also, there is little evidence of shift in the spot location, which means the cell deformation is localized at the place of granule release without propagating along the cell edge.

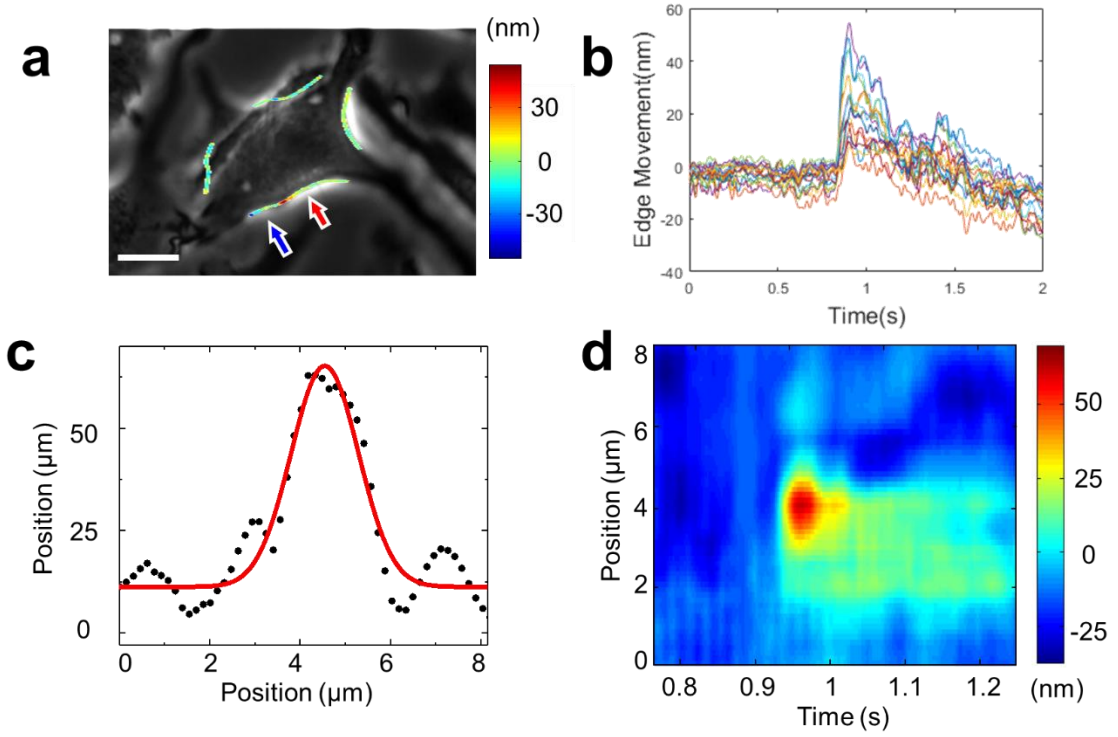

Figure 4.11 Temporal-spatial correlation between membrane edge deformation and granule release of a cell with Type 2 release. (a) Phase contrast images of RBL-2H3 cell overlapped with corresponded edge movement. The color represents the amount of cell membrane deformation in nm. Red and blue arrows marked the localized edge area being analyzed. (b) The plasma membrane responses of different locations along the localized edge area marked red and blue arrows. (c) The cell membrane edge deformation amount along the localized edge area between the red and blue arrows. (d) 2D plot of cell edge

movement with x axis in time, y axis in position. The region are between the cell edges indicated by the red and blue arrows. The color represents the cell edge change in nm.

Figure 4.12 show a complex situation, where two granule release events occur closely in both time and location, and thus may interact with each other. The color representation of the cell edge deformation (Figure 4.12a) reveals two bright (red) spots (inset is the zoom-in of these two spots), each corresponding to one release event. The spatial distribution of the membrane deformation along the cell edge reveals two peaks, each corresponds to one granule release (Figure 4.12c). The two-granule release events decay over time slowly without propagation along the cell edge as shown in the 2D temporal-spatial correlation (Figure 4.12d). The 2D temporal-spatial correlation also shows that one granule release event (marked by a black arrow) occurs ~0.1 s earlier than the second one (marked by a white arrow), and the two release event induced membrane deformation interact with each other.

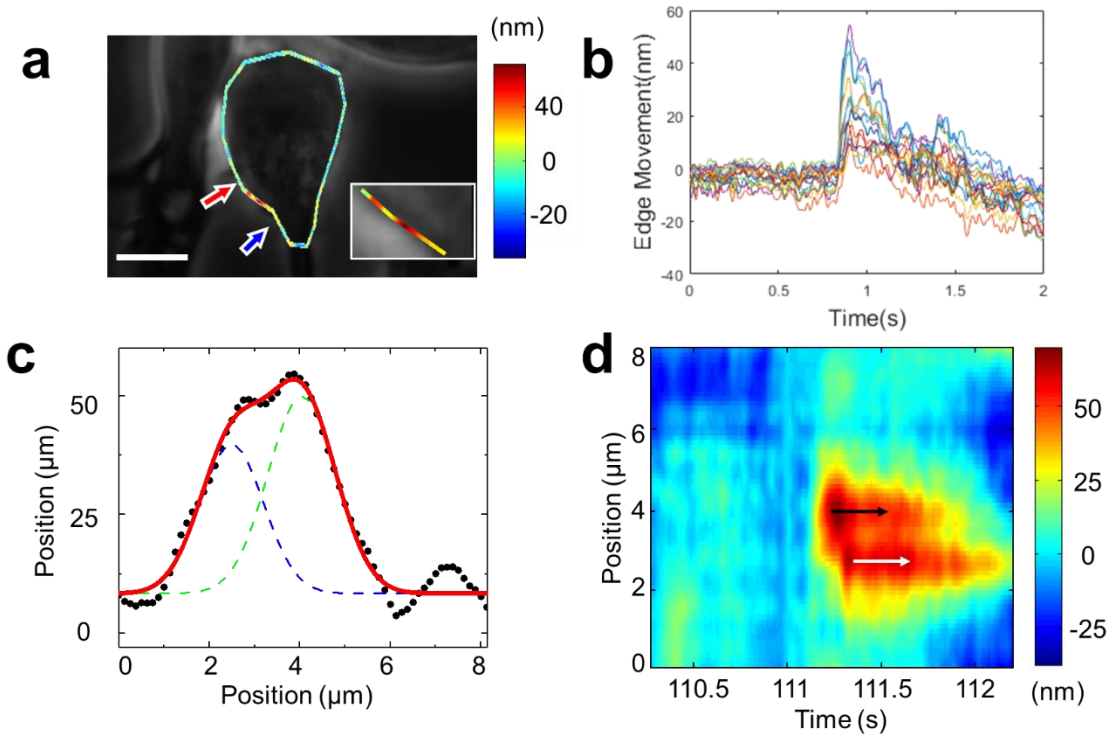

Figure 4.12 Temporal-spatial correlation between membrane edge deformation and granule release of a cell with complex release. (a) Phase contrast images of RBL-2H3 cell overlapped with corresponded edge movement. The color represents the amount of cell membrane deformation in nm. Red and blue arrows marked the localized edge area being analyzed. (b) The plasma membrane responses of different locations along the localized edge area marked red and blue arrows. (c) The cell membrane edge deformation amount along the localized edge area between the red and blue arrows. (d) 2D plot of cell edge movement with x axis in time, y axis in position. The region are between the cell edges indicated by the red and blue arrows. The color represents the cell edge change in nm.

Other examples of complex granule releases are given in Figure 4.13. These complex granule releases are resolved because of the spatial and temporal resolutions of the present label-free optical detection method.

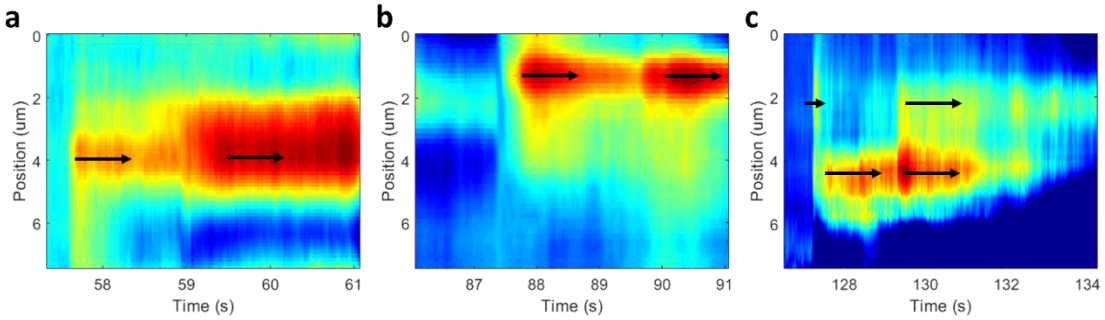

Figure 4.13 Cell edge responses upon complex granule release. (a) Temporal-spatial correlation mapping of two stepwise granule releases happened close in time at the same location. (b) Temporal-spatial correlation mapping of two pulse-like granule releases happened in series at the same location. (c) Temporal-spatial correlation mapping of four granule releases happened close in both time and location.

The observed cell expansion during granule release is consistent with the capacitance measurement, which detects cell surface area increases associated with the fusion of granules with the cell membrane[162]. The cell expansion is expected for a full fusion process of granules (Type 1)[163, 164], where a secretory granule docks onto the plasma membrane of the cell, forms a fusion pore and becomes fully incorporated with the cell membrane after releasing chemical contents in the granule to the extracellular medium. The incorporation of the granule into the cell membrane increase the area and detected as an expansion of cell edge. Type 2 cell deformation is a 'kiss-and-run' process, it is reasonable to expect a temporary cell expansion followed by recovery of the cell edge.

4.4.3 The Propagation of Granule Release induced Membrane Deformation

The simultaneous recording of phase contrast and fluorescent images allows us to examine the temporal relation between the cell membrane deformation and fluorescence

signals. Figure 4.14 shows cell membrane deformations and the corresponding fluorescence signal of four representative cells. All the cells belong to Type 1, stepwise deformation (Figure 4.14a-d). The location of fluorescence emission in each case is in close proximity with the location of cell edge deformation (Figure 4.14e), however, there is a time delay between the cell deformation and fluorescence emission. As shown in Figure 4.14a to Figure 4.14d, the fluorescence peaks are always ahead of the membrane expansion by an amount of time. And this temporal delay is proportional to the distance between the fluorescence emission spot and the deformed cell edge, which indicates the propagation of the membrane deformation from the location of granule release to the cell edge (Figure 4.16b).

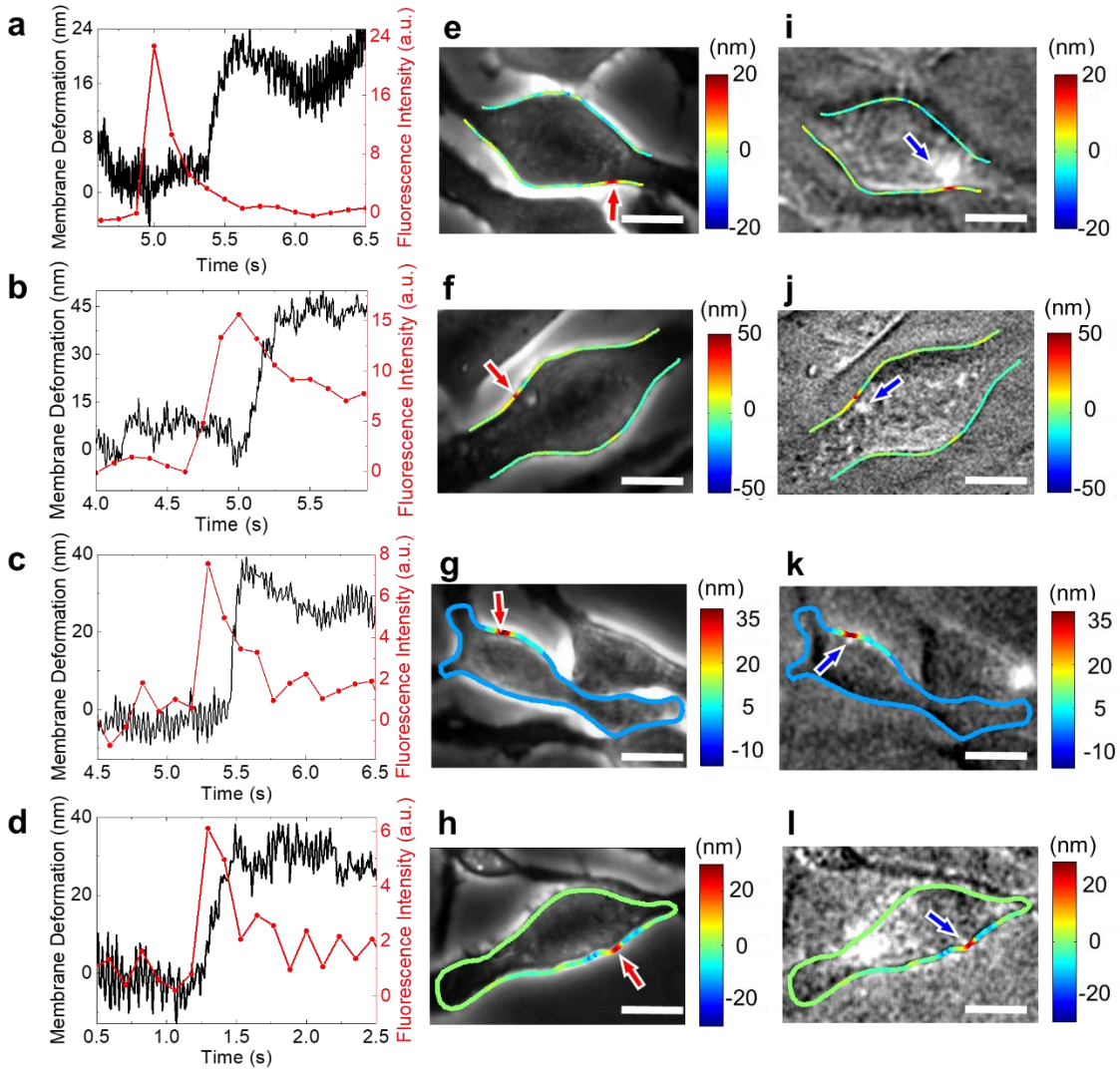

Figure 4.14 Cell edge deformation and corresponded fluorescence signal on different cells. (a-d) The cell edge movements and corresponded fluorescence signals caused by granule release from different RBL-2H3 cells. The corresponded phase contrast and fluorescence images are shown in e/i, f/j, g/k, and h/l, respectively. The red arrows in e-h indicate the locations of the edge movement plotted in a-d respectively. (e-h) Phase contrast images of RBL-2H3 cells overlap with corresponded local edge movement. The color represents the

amount of cell membrane edge deformation at different locations in nm. (i-l) Fluorescence images of RBL-2H3 cells overlap with corresponded local edge movement. The color represents the amount of cell membrane edge deformation in nm. The granule release location is pointed out by black arrows in i-l.

To further validate the propagation of the granule release induced membrane deformation, we analyzed the membrane responses upon single granule release along the whole cell surface. With the 2.5 ms temporal resolution, we were able to capture the fast response of the cell membrane to each granule exocytosis. Figure 4.15 shows the membrane responses of whole cell surface to four granule release events. When granule exocytosis happens, the cell membrane deformed quickly, showing pore-like spots on cell surface, and propagates away from the releasing point (Figure 4.15a). By coloring the deformation magnitude of the cell surface during granule release event (Figure 4.15b), we could clearly see the spatial propagation of membrane deformation induced by each granule release. By plotting the deformation along the propagation path (Figure 4.15 c-f), we see the wave-like deformation within about 3 μm along the cell surface. Most of the membrane deformation propagates mainly in one direction to the cell edge.

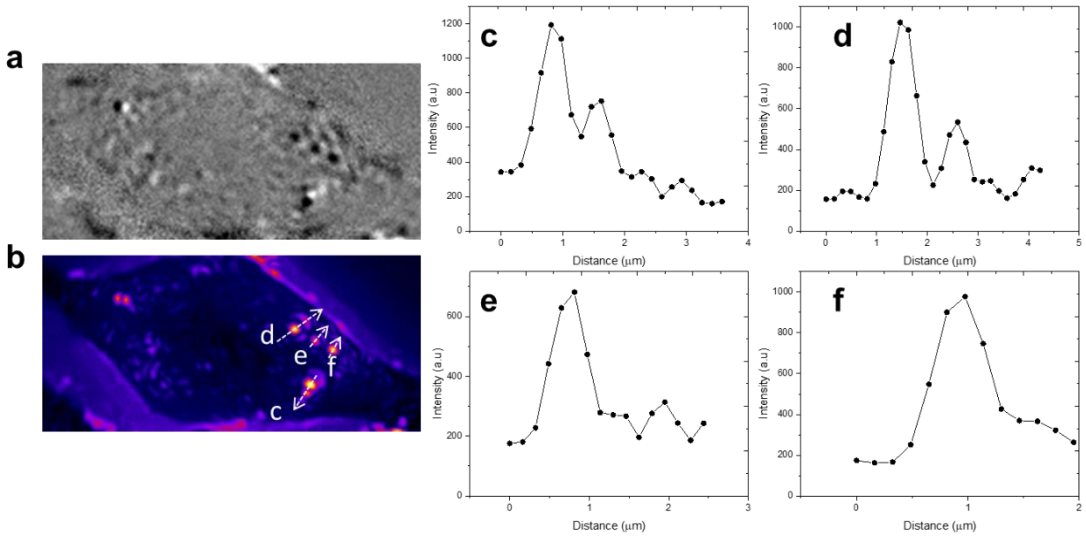

Figure 4.15 Spatial propagation of the granule release induced membrane deformation. (a) The cell membrane response caused by four granule release events in RBL-2H3 cells. The black spots correspond to the granule release positions. (b) The colormap of the cell membrane deformation upon four granule release. The white arrows marked the propagation path of each granule release. (c-f) The propagation plots of the membrane deformation along the propagation path marked in b.

By correlating the propagation distance and the time delay, we were able to calculate the propagation speed of the membrane deformation along the cell surface in each cell. The propagation distance of each granule release is measured between the center of the fluorescence emission spot and the maximum cell edge expansion, and the calculated propagation speed distribution is shown in Figure 4.16a, which shows that the speed varies from cell to cell. The average speed is about 5.2 ± 1.8 μm/s (n=24), which is consistent with membrane shape mediated wave propagation speed [167, 168].

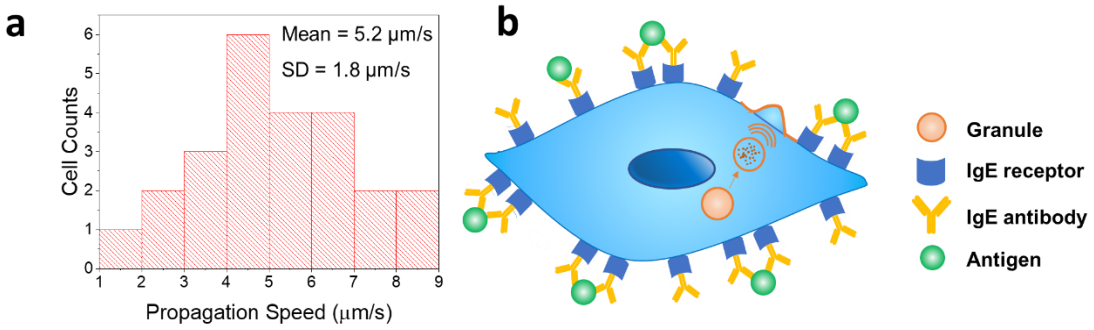

Figure 4.16 Propagation of granule release-induced membrane deformation on cell surface. (a) The histogram distribution of the propagation speed of granule-release induced membrane deformation of different cells. The average speed is 5.2 μm/s, and the standard deviation is 1.8 μm/s (n=24). (b) Schematic illustration of the membrane deformation propagation from the place where the granule release occurs to the cell edge.

4.5 Conclusion

In this chapter, we demonstrated here a label-free optical method to detect single granule release events in single cells by tracking the cell edge deformation. With the combination of phase contrast imaging and the differential optical tracking method, we have tracked the plasma membrane response to single granule exocytosis in real time with sub-nm precision and ms temporal resolution. Using this method, we have detected the sharp membrane expansion upon each granule releases in single cells and revealed two types of membrane deformation, corresponding to full fusion and 'kiss-and-run' exocytosis processes. The high spatial and temporal resolution of the method allows to resolve complex granule release patterns, including multiple granules release events that occur closely in both time and position. A time delay between fluorescence emission and cell edge deformation is detected and found to be proportional to the distance between granule

release location and the cell edge, indicating propagation of the membrane deformation along cell surface with an average speed of 5.2 μm/s. This work presents a simple and label-free method to monitor single granule release events in single cells. The method tracks cell membrane deformation, which is not directly accessible by the traditional fluorescence and electrochemical measurements, and its high spatial and temporal resolutions offer new insights into the important processes of exocytosis. This method is not limited to the cell types and is promising for label free study of synaptic granule release.

CHAPTER 5 CONCLUSION AND PERSPECTIVE

In this dissertation, we have developed three label-free platforms for the detection of molecular interaction of membrane protein on cell surface. The imaging capability of these optical imaging based platforms enable the mapping of individual cell responses for the study of cell-cell heterogeneity. The real time detection capability provides quantitative information on the both large and small molecular interaction kinetics and granule-membrane interaction kinetics.

In chapter two, we introduced a SPRi based method for the detection of the binding interactions between membrane protein and their specific antibody on cell surface. Using this method, EGFR receptor and the anti-EGFR binding process was monitored and the binding kinetics were derived. Both cell-cell variation and cell line-cell line variation were evaluated. SPRi platform is a simple way to quantify the molecular interaction on different samples. It has potential to be used for the detection of molecular interaction in thin tissue slice, which can map the receptor distribution on tissue level to distinguish the healthy cells from disease cells, and has the potential to evaluate the pharmacokinetics for drug discovery.

The third chapter described a label-free optical detection method coupled with a microfluidic device to measure the kinetics of both large and small ligands binding with membrane protein receptors on whole cells. Using this method, we are able to detect the molecular binding interaction of both large and small molecules with different types of membrane proteins. A thermodynamic model was developed to describe this method and various validations were performed to correlate the signal responses with different

parameters, including cell membrane mechanics, membrane protein density and molecular interaction kinetics. With this method, we can monitor various cellular responses related with membrane deformation, including cell adhesion, cell apoptosis and cell toxicity.

In chapter four, we have demonstrated that by tracking the cell edge membrane deformation, single granule release in single cells can be monitored. Using this method, we can measure the localized membrane deformation distribution along the cell edge and the temporal-spatial distribution of the membrane responses during granule release. By correlate the granule release induced fluorescence signal and the cell edge deformation, we were able to quantify the speed of granule release induced membrane deformation on cell surface. This method provides a simple, label free way to monitor the exocytosis process, and has great potential for the detection of neuron transmitter release in neuron network.

REFERENCES

[1] M.F. Dunn, Protein–ligand interactions: General description, in Els. 2001, *John Wiley & Sons, Ltd*.

[2] M.F. Dunn, Zinc-ligand interactions modulate assembly and stability of the insulin hexamer -- a review. *Biometals*, 2005. 18(4): p. 295-303.

[3] P.V. Escriba and G.L. Nicolson, Membrane structure and function: Relevance of lipid and protein structures in cellular physiology, pathology and therapy preface. *Biochimica Et Biophysica Acta-Biomembranes*, 2014. 1838(6): p. 1449-1450.

[4] J.P. DiNitto, T.C. Cronin, and D.G. Lambright, Membrane recognition and targeting by lipid-binding domains. *Sci STKE*, 2003. 2003(213): p. re16.

[5] W. Cho and R.V. Stahelin, Membrane-protein interactions in cell signaling and membrane trafficking. *Annu Rev Biophys Biomol Struct*, 2005. 34: p. 119-51.

[6] H. Yin and A.D. Flynn, Drugging membrane protein interactions. *Annu Rev Biomed Eng*, 2016. 18: p. 51-76.

[7] A.L. Hopkins and C.R. Groom, The druggable genome. *Nat Rev Drug Discov*, 2002. 1(9): p. 727-30.

[8] D.C. Swinney, The role of binding kinetics in therapeutically useful drug action. *Current Opinion in Drug Discovery & Development*, 2009. 12(1): p. 31-39.

[9] R.A. Copeland, D.L. Pompliano, and T.D. Meek, Opinion - drug-target residence time and its implications for lead optimization. *Nature Reviews Drug Discovery*, 2006. 5(9): p. 730-739.

[10] R.A. Copeland, The dynamics of drug-target interactions: Drug-target residence time and its impact on efficacy and safety. *Expert Opinion on Drug Discovery*, 2010. 5(4): p. 305-310.

[11] K. High, Y. Meng, M.W. Washabaugh, and Q. Zhao, Determination of picomolar equilibrium dissociation constants in solution by enzyme-linked immunosorbent assay with fluorescence detection. *Anal Biochem*, 2005. 347(1): p. 159-61.

[12] L. Prystay, M. Gosselin, and P. Banks, Determination of equilibrium dissociation constants in fluorescence polarization. *J Biomol Screen*, 2001. 6(3): p. 141-50.

[13] D.C. Swinney, The role of binding kinetics in therapeutically useful drug action. *Curr Opin Drug Discov Devel*, 2009. 12(1): p. 31-9.

[14] M. Baker, Making membrane proteins for structures: A trillion tiny tweaks. *Nature Methods*, 2010. 7(6): p. 429-434.

[15] D.M. Kullmann and M.G. Hanna, Neurological disorders caused by inherited ion-channel mutations. *Lancet Neurology*, 2002. 1(3): p. 157-166.

[16] E.C. Cooper and L.Y. Jan, Ion channel genes and human neurological disease: Recent progress, prospects, and challenges. *Proceedings of the National Academy of Sciences of the United States of America*, 1999. 96(9): p. 4759-4766.

[17] D.C. Gadsby, P. Vergani, and L. Csanady, The abc protein turned chloride channel whose failure causes cystic fibrosis. *Nature*, 2006. 440(7083): p. 477-483.

[18] S.C. Bull and A.J. Doig, Properties of protein drug target classes. *PLoS One*, 2015. 10(3): p. e0117955.

[19] K.M. Giacomini, S.M. Huang, D.J. Tweedie, L.Z. Benet, K.L.R. Brouwer, et al., Membrane transporters in drug development. *Nature Reviews Drug Discovery*, 2010. 9(3): p. 215-236.

[20] A. Tsuji, Role and relevance of membrane transporters in pharmacokinetics, pharmacological activity and toxicity and in drug development. *Yakugaku Zasshi-Journal of the Pharmaceutical Society of Japan*, 2007. 127: p. 3-4.

[21] J.A. Ware, Membrane transporters in drug discovery and development: A new mechanistic adme era. *Molecular Pharmaceutics*, 2006. 3(1): p. 1-2.

[22] I. Cascorbi, Role of pharmacogenetics of atp-binding cassette transporters in the pharmacokinetics of drugs. *Pharmacology & Therapeutics*, 2006. 112(2): p. 457-473.

[23] A.H. Schinkel and J.W. Jonker, Mammalian drug efflux transporters of the atp binding cassette (abc) family: An overview. *Advanced Drug Delivery Reviews*, 2012. 64: p. 138-153.

[24] S.T. Mccarthy, E. Harris, and R.C. Turner, Glucose control of basal insulin-secretion in diabetes. *Diabetologia*, 1977. 13(2): p. 93-97.

[25] S.M. Foord, T.I. Bonner, R.R. Neubig, E.M. Rosser, J.P. Pin, et al., International union of pharmacology. Xlvi. G protein-coupled receptor list. *Pharmacological Reviews*, 2005. 57(2): p. 279-288.

[26] M.C. Lagerstrom and H.B. Schioth, Structural diversity of g protein-coupled receptors and significance for drug discovery (vol 7, pg 339, 2008). *Nature Reviews Drug Discovery*, 2008. 7(6): p. 542-542.

[27] U. Jonsson, L. Fagerstam, B. Ivarsson, B. Johnsson, R. Karlsson, et al., Real-time biospecific interaction analysis using surface-plasmon resonance and a sensor chip technology. *Biotechniques,* 1991. 11(5): p. 620-&.

[28] S.K. Vashist and P. Vashist, Recent advances in quartz crystal microbalance-based sensors. *Journal of Sensors*, 2011.

[29] N. Moll, E. Pascal, D.H. Dinh, J.L. Lachaud, L. Vellutini, et al., Multipurpose love acoustic wave immunosensor for bacteria, virus or proteins detection. *Irbm*, 2008. 29(2-3): p. 155-161.

[30] C.K. O'Sullivan and G.G. Guilbault, Commercial quartz crystal microbalances - theory and applications. *Biosensors & Bioelectronics*, 1999. 14(8-9): p. 663-670.

[31] M. Liss, B. Petersen, H. Wolf, and E. Prohaska, An aptamer-based quartz crystal protein biosensor. *Analytical Chemistry*, 2002. 74(17): p. 4488-4495.

[32] J.Y. Chen, M.H. Li, L.S. Penn, and J. Xi, Real-time and label-free detection of cellular response to signaling mediated by distinct subclasses of epidermal growth factor receptors. *Analytical Chemistry*, 2011. 83(8): p. 3141-3146.

[33] J.Y. Chen, M. Li, L.S. Penn, and J. Xi, Real-time and label-free detection of cellular response to signaling mediated by distinct subclasses of epidermal growth factor receptors. *Anal Chem*, 2011. 83(8): p. 3141-6.

[34] J. Concepcion, K. Witte, C. Wartchow, S. Choo, D.F. Yao, et al., Label-free detection of biomolecular interactions using biolayer interferometry for kinetic characterization. *Combinatorial Chemistry & High Throughput Screening*, 2009. 12(8): p. 791-800.

[35] R.B.M. Schasfoort and A.J. Tudos, Handbook of surface plasmon resonance. 2008, Cambridge: Royal Society of Chemistry.

[36] Y. Li, H.J. Lee, and R.M. Corn, Detection of protein biomarkers using rna aptamer microarrays and enzymatically amplified surface plasmon resonance imaging. *Analytical Chemistry*, 2007. 79(3): p. 1082-1088.

[37] W.J. Zhou, A.R. Halpern, T.H. Seefeld, and R.M. Corn, Near infrared surface plasmon resonance phase imaging and nanoparticle-enhanced surface plasmon resonance phase imaging for ultrasensitive protein and DNA biosensing with oligonucleotide and aptamer microarrays. *Analytical Chemistry*, 2012. 84(1): p. 440-445.

[38] Y. Chen, K. Nakamoto, O. Niwa, and R.M. Corn, On-chip synthesis of rna aptamer microarrays for multiplexed protein biosensing with spr imaging measurements. *Langmuir*, 2012. 28(22): p. 8281-8285.

[39] T.H. Seefeld, A.R. Halpern, and R.M. Corn, On-chip synthesis of protein microarrays from DNA microarrays via coupled in vitro transcription and translation for surface plasmon resonance imaging biosensor applications. *Journal of the American Chemical Society*, 2012. 134(30): p. 12358-12361.

[40] W.B. Liang, S.P. Wang, F. Festa, P. Wiktor, W. Wang, et al., Measurement of small molecule binding kinetics on a protein microarray by plasmonic-based electrochemical impedance imaging. *Analytical Chemistry*, 2014. 86(19): p. 9860-9865.

[41] C. MacGriff, S.P. Wang, P. Wiktor, W. Wang, X.N. Shan, et al., Charge-based detection of small molecules by plasmonic-based electrochemical impedance microscopy. *Analytical Chemistry*, 2013. 85(14): p. 6682-6687.

[42] W. Wang, Y.Z. Yang, S.P. Wang, V.J. Nagaraj, Q. Liu, et al., Label-free measuring and mapping of binding kinetics of membrane proteins in single living cells. *Nature Chemistry*, 2012. 4(10): p. 846-853.

[43] W. Wang, L.L. Yin, L. Gonzalez-Malerva, S.P. Wang, X.B. Yu, et al., In situ drug-receptor binding kinetics in single cells: A quantitative label-free study of anti-tumor drug resistance. *Scientific Reports*, 2014. 4.

[44] K. Syal, W. Wang, X.N. Shan, S.P. Wang, H.Y. Chen, et al., Plasmonic imaging of protein interactions with single bacterial cells. *Biosensors & Bioelectronics*, 2015. 63: p. 131-137.

[45] F. Zhang, S. Wang, L. Yin, Y. Yang, Y. Guan, et al., Quantification of epidermal growth factor receptor expression level and binding kinetics on cell surfaces by surface plasmon resonance imaging. *Anal Chem*, 2015. 87(19): p. 9960-5.

[46] J. Mendelsohn and J. Baselga, The egf receptor family as targets for cancer therapy. *Oncogene*, 2000. 19(56): p. 6550-6565.

[47] R.I. Nicholson, J.M.W. Gee, and M.E. Harper, Egfr and cancer prognosis. *European Journal of Cancer*, 2001. 37: p. S9-S15.

[48] M.F. Press and H.J. Lenz, Egfr, her2 and vegf pathways. *Drugs*, 2007. 67(14): p. 2045-2075.

[49] J.B. Johnston, S. Navaratnam, M.W. Pitz, J.M. Maniate, E. Wiechec, et al., Targeting the egfr pathway for cancer therapy. *Current Medicinal Chemistry*, 2006. 13(29): p. 3483-3492.

[50] C.L. Arteaga, Epidermal growth factor receptor dependence in human tumors: More than just expression? *Oncologist*, 2002. 7: p. 31-39.

[51] M.K. Nyati, M.A. Morgan, F.Y. Feng, and T.S. Lawrence, Integration of egfr inhibitors with radiochemotherapy. *Nat Rev Cancer*, 2006. 6(11): p. 876-85.

[52] P.R. Dutta and A. Malty, Cellular responses to egfr inhibitors and their relevance to cancer therapy. *Cancer Letters*, 2007. 254(2): p. 165-177.

[53] P.M. Harari, Epidermal growth factor receptor inhibition strategies in oncology. *Endocrine-Related Cancer*, 2004. 11(4): p. 689-708.

[54] M.A. Olayioye, R.M. Neve, H.A. Lane, and N.E. Hynes, The erbb signaling network: Receptor heterodimerization in development and cancer. *Embo Journal*, 2000. 19(13): p. 3159-3167.

[55] Y. Yarden, The egfr family and its ligands in human cancer: Signalling mechanisms and therapeutic opportunities. *European Journal of Cancer*, 2001. 37: p. S3-S8.

[56] C.L. Arteaga and J. Baselga, Clinical trial design and end points for epidermal growth factor receptor-targeted therapies: Implications for drug development and practice. *Clinical Cancer Research*, 2003. 9(5): p. 1579-1589.

[57] J. Baselga, Why the epidermal growth factor receptor? The rationale for cancer therapy. *Oncologist*, 2002. 7: p. 2-8.

[58] J.R. Grandis and J.C. Sok, Signaling through the epidermal growth factor receptor during the development of malignancy. *Pharmacology & Therapeutics*, 2004. 102(1): p. 37-46.

[59] Y. Yarden and M.X. Sliwkowski, Untangling the erbb signalling network. *Nature Reviews Molecular Cell Biology*, 2001. 2(2): p. 127-137.

[60] J.R. Grandis and K.A. Foon, Emerging role of egfr-targeted therapies and radiation in head and neck cancer - the song/raben article reviewed. *Oncology-New York*, 2004. 18(14): p. 1767-+.

[61] N. Normanno, A. De Luca, C. Bianco, L. Strizzi, M. Mancino, et al., Epidermal growth factor receptor (egfr) signaling in cancer. *Gene*, 2006. 366(1): p. 2-16.

[62] D.S.D.S. Kang and L.M.F. Leeb-Lundberg, Negative and positive regulatory epitopes in the c-terminal domains of the human b1 and b2 bradykinin receptor subtypes determine receptor coupling efficacy to g(9/11)-mediated phospholipase c beta activity (vol 62, pg 281, 2002). *Molecular Pharmacology*, 2002. 62(3): p. 762-762.

[63] J.G. Krupnick, F. Santini, A.W. Gagnon, J.H. Keen, and J.L. Benovic, Modulation of the arrestin-clathrin interaction in cells - characterization of beta-arrestin

dominant-negative mutants. *Journal of Biological Chemistry*, 1997. 272(51): p. 32507-32512.

[64] C.L. Arteaga and D.H. Johnson, Tyrosine kinase inhibitors-zd1839 (iressa). *Current Opinion in Oncology*, 2001. 13(6): p. 491-498.

[65] F. Ciardiello, Epidermal growth factor receptor tyrosine kinase inhibitors as anticancer agents. *Drugs*, 2000. 60: p. 25-32.

[66] R.S. Herbst, Targeted therapy in non-small-cell lung cancer. *Oncology-New York*, 2002. 16(9): p. 19-24.

[67] R.S. Herbst and W.K. Hong, Targeted therapy against the epidermal growth factor receptor - introduction. *Seminars in Oncology*, 2002. 29(5): p. 1-2.

[68] R.S. Herbst and W.K. Hong, Imc-c225, an anti-epidermal growth factor receptor monoclonal antibody for treatment of head and neck cancer. *Seminars in Oncology*, 2002. 29(5): p. 18-30.

[69] D.S. Krause and R.A. Van Etten, Tyrosine kinases as targets for cancer therapy. *New England Journal of Medicine*, 2005. 353(2): p. 172-187.

[70] J.G. Paez, P.A. Janne, J.C. Lee, S. Tracy, H. Greulich, et al., Egfr mutations in lung cancer: Correlation with clinical response to gefitinib therapy. *Science*, 2004. 304(5676): p. 1497-1500.

[71] N. Normanno and W.J. Gullick, Epidermal growth factor receptor tyrosine kinase inhibitors and bone metastases: Different mechanisms of action for a novel therapeutic application? *Endocrine-Related Cancer*, 2006. 13(1): p. 3-6.

[72] G.P. Adams and L.M. Weiner, Monoclonal antibody therapy of cancer. *Nature Biotechnology*, 2005. 23(9): p. 1147-1157.

[73] R.S. Herbst and D.M. Shin, Monoclonal antibodies to target epidermal growth factor receptor-positive tumors - a new paradigm for cancer therapy. *Cancer*, 2002. 94(5): p. 1593-1611.

[74] J.r. Homola, Surface plasmon resonance based sensors. Springer series on chemical sensors and biosensors. 2006, Berlin, Heidelberg: Springer-Verlag Berlin Heidelberg. 1 online resource (Online-Ressource.).

[75] A. Otto, Excitation of nonradiative surface plasma waves in silver by method of frustrated total reflection. *Zeitschrift Fur Physik*, 1968. 216(4): p. 398-&.

[76] E. Kretschmann, Die bestimmung optischer konstanten von metallen durch anregung von oberflächenplasmaschwingungen. *Zeitschrift für Physik*, 1971. 241(4): p. 313-324.

[77] C. Fu and Z.M. Zhang, Thermal radiative properties of metamaterials and other nanostructured materials: A review. *Frontiers of Energy and Power Engineering in China*, 2009. 3(1): p. 11-26.

[78] M.A. Cooper, Optical biosensors in drug discovery. *Nat Rev Drug Discov*, 2002. 1(7): p. 515-28.

[79] H.J. Lee, T.T. Goodrich, and R.M. Corn, Spr imaging measurements of 1-d and 2-d DNA microarrays created from microfluidic channels on gold thin films. *Analytical Chemistry*, 2001. 73(22): p. 5525-5531.

[80] G.J. Wegner, A.W. Wark, H.J. Lee, E. Codner, T. Saeki, et al., Real-time surface plasmon resonance imaging measurements for the multiplexed determination of protein adsorption/desorption kinetics and surface enzymatic reactions on peptide microarrays. *Analytical Chemistry*, 2004. 76(19): p. 5677-5684.

[81] H.H. Nguyen, J. Park, S. Kang, and M. Kim, Surface plasmon resonance: A versatile technique for biosensor applications. *Sensors (Basel)*, 2015. 15(5): p. 10481-510.

[82] Y. Zhou, A.L. Goenaga, B.D. Harms, H. Zou, J.L. Lou, et al., Impact of intrinsic affinity on functional binding and biological activity of egfr antibodies. *Molecular Cancer Therapeutics*, 2012. 11(7): p. 1467-1476.

[83] E.C. Hulme and M.A. Trevethick, Ligand binding assays at equilibrium: Validation and interpretation. *British Journal of Pharmacology*, 2010. 161(6): p. 1219-1237.

[84] J. Kurai, H. Chikumi, K. Hashimoto, K. Yamaguchi, A. Yamasaki, et al., Antibody-dependent cellular cytotoxicity mediated by cetuximab against lung cancer cell lines. *Clinical Cancer Research*, 2007. 13(5): p. 1552-1561.

[85] A. Hellmuth and L.I.A. Calderón Villalobos, Radioligand binding assays for determining dissociation constants of phytohormone receptors, in Plant proteostasis: Methods and protocols, L.M. Lois and R. Matthiesen, Editors. 2016, *Springer New York*: New York, NY. p. 23-34.

[86] C. Dong, Z. Liu, and F. Wang, Radioligand saturation binding for quantitative analysis of ligand-receptor interactions. *Biophysics Reports*, 2015. 1: p. 148-155.

[87] J. Zhen, T. Antonio, S. Ali, K.A. Neve, A.K. Dutta, et al., Use of radiolabeled antagonist assays for assessing agonism at d2 and d3 dopamine receptors:

Comparison with functional gtpγs assays. *Journal of Neuroscience Methods*, 2015. 248: p. 7-15.

[88] J.F. Glickman, A. Schmid, and S. Ferrand, Scintillation proximity assays in high-throughput screening. *Assay and Drug Development Technologies*, 2008. 6(3): p. 433-455.

[89] J.C. Owicki, Fluorescence polarization and anisotropy in high throughput screening: Perspectives and primer. *Journal of Biomolecular Screening*, 2000. 5(5): p. 297-306.

[90] M.J. Lohse, S. Nuber, and C. Hoffmann, Fluorescence/bioluminescence resonance energy transfer techniques to study g-protein-coupled receptor activation and signaling. *Pharmacological Reviews*, 2012. 64(2): p. 299-336.

[91] S. Veiksina, S. Kopanchuk, O. Mazina, R. Link, A. Lille, et al., Homogeneous fluorescence anisotropy-based assay for characterization of ligand binding dynamics to gpcrs in budded baculoviruses: The case of cy3b-ndp-alpha-msh binding to mc4 receptors. *Methods Mol Biol*, 2015. 1272: p. 37-50.

[92] M.A. Ayoub, J. Trebaux, J. Vallaghe, F. Charrier-Savournin, K. Al-Hosaini, et al., Homogeneous time-resolved fluorescence-based assay to monitor extracellular signal-regulated kinase signaling in a high-throughput format. *Front Endocrinol (Lausanne)*, 2014. 5: p. 94.

[93] N. Oueslati, C. Hounsou, A. Belhocine, T. Rodriguez, E. Dupuis, et al., Time-resolved fret strategy to screen gpcr ligand library. *Methods Mol Biol*, 2015. 1272: p. 23-36.

[94] G.I. Mashanov, D. Tacon, M. Peckham, and J.E. Molloy, The spatial and temporal dynamics of pleckstrin homology domain binding at the plasma membrane measured by imaging single molecules in live mouse myoblasts. *Journal of Biological Chemistry*, 2004. 279(15): p. 15274-15280.

[95] L. Parhamifar and S.M. Moghimi, Total internal reflection fluorescence (tirf) microscopy for real-time imaging of nanoparticle-cell plasma membrane interaction. *Methods Mol Biol*, 2012. 906: p. 473-82.

[96] A. Nickerson, T. Huang, L.J. Lin, and X.L. Nan, Photoactivated localization microscopy with bimolecular fluorescence complementation (bifc-palm) for nanoscale imaging of protein-protein interactions in cells. *Plos One*, 2014. 9(6).

[97] C.D. Hu, Y. Chinenov, and T.K. Kerppola, Visualization of interactions among bzip and rel family proteins in living cells using bimolecular fluorescence complementation. *Molecular Cell*, 2002. 9(4): p. 789-798.

[98] Z.C. Pei, J. Saint-Guirons, C. Kack, B. Ingemarsson, and T. Aastrup, Real-time analysis of the carbohydrates on cell surfaces using a qcm biosensor: A lectin-based approach. *Biosensors & Bioelectronics*, 2012. 35(1): p. 200-205.

[99] K. Subramanian, C.J. Fee, R. Fredericks, R.S. Stubbs, and M.T. Hayes, Insulin receptor-insulin interaction kinetics using multiplex surface plasmon resonance. *Journal of Molecular Recognition*, 2013. 26(12): p. 643-652.

[100] I. Navratilova, J. Besnard, and A.L. Hopkins, Screening for gpcr ligands using surface plasmon resonance. *Acs Medicinal Chemistry Letters*, 2011. 2(7): p. 549-554.

[101] C. Bieri, O.P. Ernst, S. Heyse, K.P. Hofmann, and H. Vogel, Micropatterned immobilization of a g protein-coupled receptor and direct detection of g protein activation. *Nature Biotechnology*, 1999. 17(11): p. 1105-1108.

[102] M. Nirschl, F. Reuter, and J. Voros, Review of transducer principles for label-free biomolecular interaction analysis. *Biosensors (Basel)*, 2011. 1(3): p. 70-92.

[103] Y. Guan, X. Shan, F. Zhang, S. Wang, H.Y. Chen, et al., Kinetics of small molecule interactions with membrane proteins in single cells measured with mechanical amplification. *Sci Adv*, 2015. 1(9): p. e1500633.

[104] F.N. Zhang, S.P. Wang, L.L. Yin, Y.Z. Yang, Y. Guan, et al., Quantification of epidermal growth factor receptor expression level and binding kinetics on cell surfaces by surface plasmon resonance imaging. *Analytical Chemistry*, 2015. 87(19): p. 9960-9965.

[105] M.M. Baksh, A.K. Kussrow, M. Mileni, M.G. Finn, and D.J. Bornhop, Label-free quantification of membrane-ligand interactions using backscattering interferometry. *Nat Biotechnol*, 2011. 29(4): p. 357-60.

[106] F. Zhang, W. Jing, A. Hunt, H. Yu, Y. Yang, et al., Label-free quantification of small-molecule binding to membrane proteins on single cells by tracking nanometer-scale cellular membrane deformation. *ACS Nano*, 2018. 12(2): p. 2056-2064.

[107] P. Bergese, G. Oliviero, I. Alessandri, and L.E. Depero, Thermodynamics of mechanical transduction of surface confined receptor/ligand reactions. *Journal of Colloid and Interface Science*, 2007. 316(2): p. 1017-1022.

[108] W. Helfrich, Elastic properties of lipid bilayers: Theory and possible experiments. *Z Naturforsch C*, 1973. 28(11): p. 693-703.

[109] S. Leibler, Curvature instability in membranes. *Journal De Physique*, 1986. 47(3): p. 507-516.

[110] J. Zimmerberg and M.M. Kozlov, How proteins produce cellular membrane curvature. *Nat Rev Mol Cell Biol*, 2006. 7(1): p. 9-19.

[111] H.T. McMahon and E. Boucrot, Membrane curvature at a glance. *J Cell Sci*, 2015. 128(6): p. 1065-70.

[112] A. Callan-Jones and P. Bassereau, Curvature-driven membrane lipid and protein distribution. *Current Opinion in Solid State and Materials Science*, 2013. 17(4): p. 143-150.

[113] C. Ionescu-Zanetti, R.M. Shaw, J.G. Seo, Y.N. Jan, L.Y. Jan, et al., Mammalian electrophysiology on a microfluidic platform. *Proceedings of the National Academy of Sciences of the United States of America*, 2005. 102(26): p. 9112-9117.

[114] D. Purves, Neuroscience. 2nd ed. ed. 2001, Sunderland, Mass. ; [Great Britain]: Sinauer Associates.

[115] G.M. Cooper and R.E. Hausman, The cell : A molecular approach. 6th ed. ed. 2013, Sunderland, MA: Sinauer Associates.

[116] M.A. Lemmon, Membrane recognition by phospholipid-binding domains. *Nat Rev Mol Cell Biol*, 2008. 9(2): p. 99-111.

[117] J.B. Eaton, J.H. Peng, K.M. Schroeder, A.A. George, J.D. Fryer, et al., Characterization of human alpha 4 beta 2-nicotinic acetylcholine receptors stably and heterologously expressed in native nicotinic receptor-null sh-ep1 human epithelial cells. *Molecular Pharmacology*, 2003. 64(6): p. 1283-1294.

[118] A.L. Hopkins and C.R. Groom, The druggable genome. *Nature Reviews Drug Discovery*, 2002. 1(9): p. 727-730.

[119] Y.R. Zou, A.H. Kottmann, M. Kuroda, I. Taniuchi, and D.R. Littman, Function of the chemokine receptor cxcr4 in haematopoiesis and in cerebellar development. *Nature*, 1998. 393(6685): p. 595-9.

[120] S. Hatse, K. Princen, G. Bridger, E. De Clercq, and D. Schols, Chemokine receptor inhibition by amd3100 is strictly confined to cxcr4. *Febs Letters*, 2002. 527(1-3): p. 255-262.

[121] U.M. Domanska, H. Timmer-Bosscha, W.B. Nagengast, T.H.O. Munnink, R.C. Kruizinga, et al., Cxcr4 inhibition with amd3100 sensitizes prostate cancer to docetaxel chemotherapy. *Neoplasia*, 2012. 14(8): p. 709-718.

[122] W.B. Zhang, J.M. Navenot, B. Haribabu, H. Tamamura, K. Hiramatu, et al., A point mutation that confers constitutive activity to cxcr4 reveals that t140 is an inverse

agonist and that amd3100 and alx40-4c axe weak partial agonists. *Journal of Biological Chemistry*, 2002. 277(27): p. 24515-24521.

[123] E. Zwick, J. Bange, and A. Ullrich, Receptor tyrosine kinase signalling as a target for cancer intervention strategies. *Endocrine-Related Cancer*, 2001. 8(3): p. 161-173.

[124] L. Knudsen, P. De Meyts, and V.V. Kiselyov, Insight into the molecular basis for the kinetic differences between the two insulin receptor isoforms. *Biochemical Journal*, 2011. 440: p. 397-403.

[125] O.D. Schneider, A.A. Weiss, and W.E. Miller, Pertussis toxin signals through the tcr to initiate cross-desensitization of the chemokine receptor cxcr4. *Journal of Immunology*, 2009. 182(9): p. 5730-5739.

[126] S. Mangmool and H. Kurose, G(i/o) protein-dependent and -independent actions of pertussis toxin (ptx). *Toxins*, 2011. 3(7): p. 884-899.

[127] P. Sengupta, T. Jovanovic-Talisman, D. Skoko, M. Renz, S.L. Veatch, et al., Probing protein heterogeneity in the plasma membrane using palm and pair correlation analysis. *Nature Methods*, 2011. 8(11): p. 969-975.

[128] C. Klockenbusch and J. Kast, Optimization of formaldehyde cross-linking for protein interaction analysis of non-tagged integrin beta1. *J Biomed Biotechnol*, 2010. 2010: p. 927585.

[129] B. Metz, G.F. Kersten, P. Hoogerhout, H.F. Brugghe, H.A. Timmermans, et al., Identification of formaldehyde-induced modifications in proteins: Reactions with model peptides. *J Biol Chem*, 2004. 279(8): p. 6235-43.

[130] B. Metz, G.F. Kersten, G.J. Baart, A. de Jong, H. Meiring, et al., Identification of formaldehyde-induced modifications in proteins: Reactions with insulin. *Bioconjug Chem*, 2006. 17(3): p. 815-22.

[131] B.W. Sutherland, J. Toews, and J. Kast, Utility of formaldehyde cross-linking and mass spectrometry in the study of protein-protein interactions. *J Mass Spectrom*, 2008. 43(6): p. 699-715.

[132] R. Thavarajah, V.K. Mudimbaimannar, J. Elizabeth, U.K. Rao, and K. Ranganathan, Chemical and physical basics of routine formaldehyde fixation. *J Oral Maxillofac Pathol*, 2012. 16(3): p. 400-5.

[133] T.C. Sudhof, The synaptic vesicle cycle. *Annu Rev Neurosci*, 2004. 27: p. 509-47.

[134] B. Katz, The release of neural transmitter substances. 1969, Springfield, Ill.: Thomas.

[135] T.C. Sudhof and J. Rizo, Synaptic vesicle exocytosis. *Cold Spring Harb Perspect Biol*, 2011. 3(12).

[136] A. Hendrix, W. Westbroek, M. Bracke, and O. De Wever, An ex(o)citing machinery for invasive tumor growth. *Cancer Research*, 2010. 70(23): p. 9533-9537.

[137] J.K. Angleson and W.J. Betz, Monitoring secretion in real time: Capacitance, amperometry and fluorescence compared. *Trends in Neurosciences*, 1997. 20(7): p. 281-287.

[138] W.J. Tyler and V.N. Murthy, Synaptic vesicles. *Curr Biol*, 2004. 14(8): p. R294-7.

[139] F. Lemaitre, M.G. Collignon, and C. Amatore, Recent advances in electrochemical detection of exocytosis. *Electrochimica Acta*, 2014. 140: p. 457-466.

[140] L. Mellander, A.S. Cans, and A.G. Ewing, Electrochemical probes for detection and analysis of exocytosis and vesicles. *Chemphyschem*, 2010. 11(13): p. 2756-2763.

[141] E. Neher and A. Marty, Discrete changes of cell membrane capacitance observed under conditions of enhanced secretion in bovine adrenal chromaffin cells. *Proc Natl Acad Sci U S A*, 1982. 79(21): p. 6712-6.

[142] R.E. Thompson, M. Lindau, and W.W. Webb, Robust, high-resolution, whole cell patch-clamp capacitance measurements using square wave stimulation. *Biophysical Journal*, 2001. 81(2): p. 937-948.

[143] B. Rituper, A. Gucek, J. Jorgacevski, A. Flasker, M. Kreft, et al., High-resolution membrane capacitance measurements for the study of exocytosis and endocytosis. *Nat Protoc*, 2013. 8(6): p. 1169-83.

[144] W.-Z. Wu, W.-H. Huang, W. Wang, Z.-L. Wang, J.-K. Cheng, et al., Monitoring dopamine release from single living vesicles with nanoelectrodes. *Journal of the American Chemical Society*, 2005. 127(25): p. 8914-8915.

[145] C.T. Wang, R. Grishanin, C.A. Earles, P.Y. Chang, T.F. Martin, et al., Synaptotagmin modulation of fusion pore kinetics in regulated exocytosis of dense-core vesicles. *Science*, 2001. 294(5544): p. 1111-5.

[146] B. Zhang, M. Heien, M.F. Santillo, L. Mellander, and A.G. Ewing, Temporal resolution in electrochemical imaging on single pc12 cells using amperometry and voltammetry at microelectrode arrays. *Analytical Chemistry*, 2011. 83(2): p. 571-577.

[147] K.L. Adams, B.K. Jena, S.J. Percival, and B. Zhang, Highly sensitive detection of exocytotic dopamine release using a gold-nanoparticle-network microelectrode. *Anal Chem*, 2011. 83(3): p. 920-7.

[148] C. Amatore, S. Arbault, M. Guille, and F. Lemaitre, Electrochemical monitoring of single cell secretion: Vesicular exocytosis and oxidative stress. *Chemical Reviews*, 2008. 108(7): p. 2585-2621.

[149] L. Mellander, A.S. Cans, and A.G. Ewing, Electrochemical probes for detection and analysis of exocytosis and vesicles. *Chemphyschem*, 2010. 11(13): p. 2756-63.

[150] B. Zhang, K.L. Adams, S.J. Luber, D.J. Eves, M.L. Heien, et al., Spatially and temporally resolved single-cell exocytosis utilizing individually addressable carbon microelectrode arrays. *Anal Chem*, 2008. 80(5): p. 1394-400.

[151] A. Anantharam, B. Onoa, R.H. Edwards, R.W. Holz, and D. Axelrod, Localized topological changes of the plasma membrane upon exocytosis visualized by polarized tirfm. *Journal of Cell Biology*, 2010. 188(3): p. 415-428.

[152] D. Zenisek, J.A. Steyer, and W. Almers, Transport, capture and exocytosis of single synaptic vesicles at active zones. *Nature*, 2000. 406(6798): p. 849-854.

[153] M.A. Gaffield and W.J. Betz, Imaging synaptic vesicle exocytosis and endocytosis with fm dyes. *Nat Protoc*, 2006. 1(6): p. 2916-21.

[154] W.J. Betz, F. Mao, and C.B. Smith, Imaging exocytosis and endocytosis. *Current Opinion in Neurobiology*, 1996. 6(3): p. 365-371.

[155] J.D. Keighron, A.G. Ewing, and A.S. Cans, Analytical tools to monitor exocytosis: A focus on new fluorescent probes and methods. *Analyst*, 2012. 137(8): p. 1755-1763.

[156] S.C. Ge, S. Koseoglu, and C.L. Haynes, Bioanalytical tools for single-cell study of exocytosis. *Analytical and Bioanalytical Chemistry*, 2010. 397(8): p. 3281-3304.

[157] D.F. Steinbrenner and J.C. Behrends, Serotonin-loading increases granule size and prolongs fusion pore formation in two types of rat basophilic leukaemia (rbl) mast cell analogs. *Biophysical Journal*. 104(2): p. 620a-621a.

[158] M.A. Gaffield and W.J. Betz, Imaging synaptic vesicle exocytosis and endocytosis with fm dyes. *Nature Protocols*, 2006. 1(6): p. 2916-2921.

[159] E. Ales, L. Tabares, J.M. Poyato, V. Valero, M. Lindau, et al., High calcium concentrations shift the mode of exocytosis to the kiss-and-run mechanism. *Nat Cell Biol*, 1999. 1(1): p. 40-4.

[160] L. Ren, L.J. Mellander, J. Keighron, A.S. Cans, M.E. Kurczy, et al., The evidence for open and closed exocytosis as the primary release mechanism. *Quarterly Reviews of Biophysics,* 2016. 49.

[161] R.M. Wightman and C.L. Haynes, Synaptic vesicles really do kiss and run. *Nature Neuroscience*, 2004. 7(4): p. 321-322.

[162] G. Alvarez De Toledo, R. Fernandez-Chacon, and J.M. Fernandez, Release of secretory products during transient vesicle fusion. *Nature (London),* 1993. 363(6429): p. 554-558.

[163] C. Amatore, Y. Bouret, E.R. Travis, and R.M. Wightman, Interplay between membrane dynamics, diffusion and swelling pressure governs individual vesicular exocytotic events during release of adrenaline by chromaffin cells. *Biochimie*, 2000. 82(5): p. 481-496.

[164] C. Amatore, A.I. Oleinick, and I. Svir, Reconstruction of aperture functions during full fusion in vesicular exocytosis of neurotransmitters. *Chemphyschem*, 2010. 11(1): p. 159-74.

[165] D.F. Steinbrenner and J.C. Behrends, Serotonin-loading increases granule size and prolongs fusion pore formation in two types of rat basophilic leukaemia (rbl) mast cell analogs. *Biophysical Journal*, 2013. 104(2): p. 620a-621a.

[166] J. Pi, L.F. Huang, F. Yang, J.H. Jiang, H. Jin, et al., Atomic force microscopy study of ionomycin-induced degranulation in rbl-2h3 cells. *Scanning*, 2016. 38(6): p. 525-534.

[167] Z.H. Wu, M.H. Su, C. Tong, M. Wu, and J. Liu, Membrane shape-mediated wave propagation of cortical protein dynamics. *Nature Communications*, 2018. 9.

[168] A. Veksler and N.S. Gov, Calcium-actin waves and oscillations of cellular membranes. *Biophysical Journal*, 2009. 97(6): p. 1558-1568.